Extrusion of plastic crystals

by
Yngve Wik Ydersbond
Physics of Geological Processes
Department of Physics
University of Oslo
Norway

Thesis submitted for the degree
Master of Science

October 2008

Abstract

In this study we have done experiments on extrusion processes. This is important in both industry and geological settings. The transition from ductile to brittle deformation inside the extrusion die is observed as a optical contrast boundary, also called slip-line, between the regions in the die where stick and slip boundary conditions prevail. The dynamic of this boundary is measured *insitu* through optically transparent Plexiglas dies. The organic crystalline materials, Succinonitrile and Camphene, we have used are good analogs for other crystalline material, such as aluminium. We have observed several processes that are important in the production of extruded aluminium products. Several statistical measurements have been carried out on the slip-line, these have shown that the system are persistent or antipersistent depending on the length scale it is observed. Furthermore, we have analysed the bulk and surface velocity of the flowing material. We have systematically varied the radius of the die curvature to see the effect this have on the slip-line behaviour, however, no conclusive results we obtained for the influence of the die curvature.

Acknowledgement

I want to express my sincere gratitude to my main supervisors Dag Kristian Dyste and Espen Jettestuen. The second Dag Kristian heard about my interest in taking on an experimental assignment he would start pitching ideas. When I finally settled with the exiting task of extruding something called organic plastic crystals, it became evident to me that Dag Kristian is a man that never will run out of ideas of fun things to investigate. Many times have I expressed my scepsis and often rejected the most extravagant approaches he suggest, only to find myself preforming and developing them with enthusiasm some week later. I have learnt from him to not get scared by things that seemingly are immensely difficult and time consuming, but rater try to further develop the idea and create the tool's that solves the challenge. I would like to thank Dag Kristian Dysthe for giving me the opportunity to experiment.

With the great help form Olav Gundersen, we would finally get all the "sophisticated" mid-eighties equipment to work in our favour and collect experimental data. However, experimental data are not the same as results. The contribution from Espen Jettestuen in process of turning raw-data into results was invaluable. He is a true craftsman and an artist when it comes to analysing data. Espen had not signed any contract to be my supervisor, none the less he greeted me with open arms and clear answers every time I would knock on his door. As my visits became increasingly more frequent and the questions more intricate it was clear that he was my supervisor as well. Thank you so much for learning me so much Espen!

I also would like to thank the great community here at PGP that always takes time to listen and help me with everything from the smallest compilation error to the very fundamental issues of our science. The list of people who helped me include every PhD. and Master student and most of the senior staff at PGP. Thank you so much for your for having an unselfish mindset! Some persons stands out, and deserve a little additional attention.I am greatly indebted to Ola K. Eriksen, he is always there when I need an extra set of hands and an additional brain. The linguistic help from my fa-

vourite American Kirsten Fristad has been fantastic, without you my thesis would have been a lot more awkward. I am also grateful for all the time Anders Nermoen has devoted to scientific and non-scientific discussions with me.

There are a small group of people that always has, seemingly, unconditionally supported me throughout my education. With all the moral, emotional and economic support I could ever ask for. My sister Hilde was just as proud of me the first year of my study when she told her friends about my chemistry studies, as she was when she discovered that I studied physics. I am very proud of you Hilde, Mamma and Pappa. Thank you for the commitment you have infected me with.

Last, but far from least, I would like to thank Margit-Iren for her unconditional love and support during the often stress full time I was writing my master thesis. I will do my best to reciprocate in the years to come.

Contents

Chapter 1

Introduction

1.1 Motivation

Extrusion processes are abundant in both nature and industry. The extrusion of magmatic bodies takes place several places on earth. Two examples, shown in Figure 1.1, are the extrusive event taking place in the Mount St.Helens crater in the USA [1] and the extruded mud breccia sheet in Azerbaijan [2]. The extruded profile in Azerbaijan bears remarkable resemblance to the profiles extruded in the laboratory experiments discussed in this thesis. The main focus of this report is the transition from ductile to brittle deformation during the extrusion process. Our investigation is based on visual observations made inside a die during extrusion. In this system the ductile-brittle transition is identified by the border between stick and slip conditions inside a flow-through cuvette. In the ductile regime, the flow is laminar with zero velocity boundary conditions. In the brittle regime, there is plug flow with friction between the flowing material and the walls. Our experiments reveal the spatial dynamics of this ductile-brittle transition (DBT). A similar dynamic of the DBT is reported to take place in the Earth's crust [3]. The latter findings show that the level of the transition zone is shallower for low strain-rates, and deepens with increasing strain-rate.

The processing industry relies on extrusion to produce a vast variety of products. Some examples are tubing, window frames, pills and plates made from a wide variety of materials. Aluminium alloys, polymers, plastic crystals, pharmaceuticals and food are some of the materials commonly extruded. In Europe alone, the aluminium industry provides employment for one million people and a revenue of approximately 37 million euros a year [4]. Unfortunately, manufacturers encounter instabilities during the processing of

(a) (b)

Figure 1.1: (a) show the ongoing dome formation a Mount St Helena in USA. A huge slab igneous rock is extruded from the volcano. The event is monitored and studied by a large group of researchers.(b) is a stunning geological example of extrusion from Azerbaijan. Courtesy of H. Svensen

different materials, which limits production rates and design. Examples include imbalances in the flow exiting the die giving rise to shape variations and twisting of the finished section and precipitates from the extrusion flow adhering to the die surface that scratch the extruded profiles. Much engineering research is invested in resolving specific industrial extrusion problems in order to meet the demanded narrow dimensional tolerance and surface requirements. There is no doubt that the quality of extruded products have improved significantly since the first copper pipes were extruded early in the 19th century[1], however there are general aspects of extrusion that are still poorly understood in the scientific community.

1.1.1 Overview of the extrusion process

Extrusion refers to the violent process of plastic deformation of materials by thrusting them through a restricting orifice. The extruded material is forced through a die where severe plastic deformation takes place. The result is an extruded profile with the shape of the die-exit. As an analogy think of toothpaste being squeezed out from the tube and taking on the shape of the

[1]The extrusion process was patented by J.Bramahs in 1897 [5]

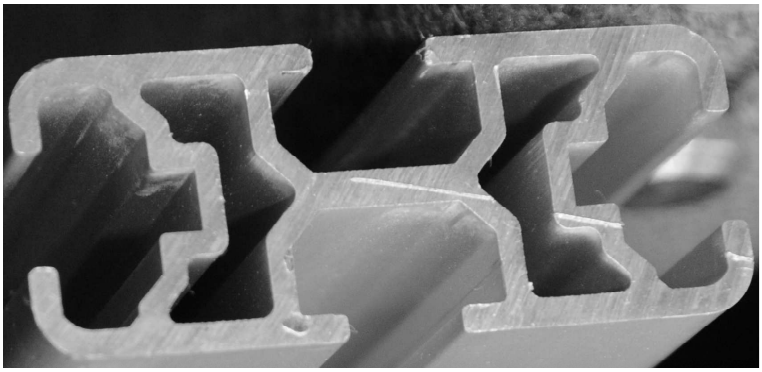

Figure 1.2: Example of an extruded aluminium profile supporting a partition wall in an office at University of Oslo.

spout. This technique allows profiles with complex cross-sectional shapes to be produced cost-efficiently. Figure 1.2 shows one example of an extruded profile taken from our everyday life.

Figure 1.3 gives an overview of the different features of a typical press used for direct hot extrusion of metals, including aluminium. The term "direct" refers to extrusion where the die is held stationary, and the ram presses the billet towards and through the bearing channel[2]. The term "hot" means that the material in the container is heated above its recrystallisation temperature. This elevated temperature makes the material flow easier and prevents strain hardening. Our extrusion experiments belong in the category of direct hot extrusion because of the technique and the conditions at which we extrude the materials Succinonitrile and Camphene. For a comprehensive explanation of the aluminium extrusion process see [6].

Our experiments are performed with plastic crystals that behave plastically at temperatures considerably lower than those of metals used in the extrusion industry. These analog material properties allow us to perform extrusion experiments in a transparent die at moderate temperatures and pressures. The transition from stick to slip conditions illustrated in Figure 1.3 can then be optically traced during the course of extrusion. In the inlet region of the die the extrusion material adheres to the die and appears dark in images. Hence there is no profile surface to be observed here. Towards the die outlet the material detaches from the die and this region appears optically brighter. In this region, the profile surface becomes visible.

[2]This expression refers to the channel inside the die made up by the bearing surfaces

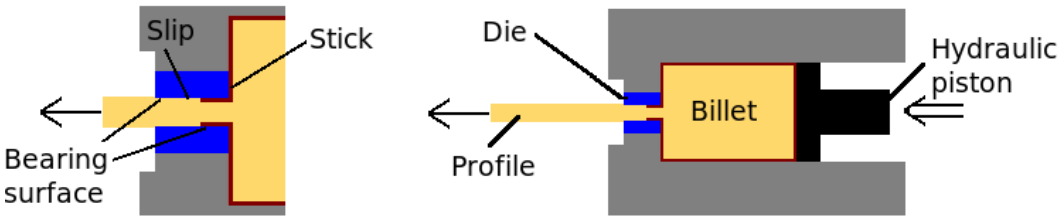

Figure 1.3: An overview of the extrusion process, identifying the main parts. The billet (also called an ingot) is heated to the recrystallisation temperature prior to extrusion, to facilitate easy flow and inhibit strain hardening. Inside the container holding the billet, the material sticks to the wall. At some point between the die inlet and outlet, the boundary conditions change to those of slip, and friction between the bearing surface and the profile prevails.

The sharp intensity border between the dark sticking region and the bright slipping region is seen as a line running over the surface of the extruded material. This line is henceforward referred to as the slip-line. In the work presented in this report, the slip-line plays an integral role in the analysis and characterisation of the extrusion process.

1.1.2 Theoretical challenges linked to extrusion

The extrusion phenomena involves plastic deformation and friction. These are physical processes that are not fully understood when treated separately. This makes extrusion dynamics a complex system well worth studying in detail. Historically, the majority of extrusion research has focused on how to increase production rates and improve the quality of the extruded profile. This has usually been done by examining the extruded material after a press, and then making the appropriate adjustments to the billet and die. This engineering approach is a powerful and fast way to improve the quality of the finished product. Unfortunately, it tells us little about the processes going on inside the die. We have, therefore, developed an experimental setup allowing us to take *in situ* measurements inside the die. We believe that analysing the deformation taking place in the die will give a more fundamental understanding of the extrusion process.

There are numerous studies that attempt to simulate the various processes

inside the extrusion die. However, the instabilities introduced by a dynamic slip-line are often omitted in these models.

It is, for example, assumed that there either is full slip in the entire bearing channel [7] or that there is sticking in a region of fixed length at the inlet side of the die [8].

One study prescribing stick throughout the entire die resulted in strain-rates approaching infinity at the die outlet, making the bulk extrusion material numerically reach the melting temperature [9]. The experiments we have performed and previous experimental studies [10, 11] indicate that these temperatures are not reached inside the die. A more reasonable temperature prediction for the bulk flow was obtained when slip boundary conditions were applied in the outlet side of the die [9]. Implementation of a smooth transition from stick to slip in the die was needed to reduce the predicted strain rates. The sharp stick-slip transition has also been modelled using Coulomb friction model. The critical shear stress,τ_c, is along the bearing surface given by

$$\tau_c = \mu\sigma_n, \tag{1.1}$$

where μ is the friction coefficient and σ_n is the normal compressive stress. When the shear stress in the flowing material next to the bearing surface, τ, is smaller than τ_c this model prescribes stick boundary conditions and where $\tau = \tau_c$, slip boundary conditions prevails. The numerical results when using Coulomb friction is reported to agree well with experimental observations [12].

Material close to the bearing surfaces can experience a very high degree of deformation compared to the material in the centre of the die. Studies of the cross-section of extruded aluminium profiles revealed a up to 250 μm thick heavily sheared zone at the surface of the sections [13, 14]. Analytical solutions for the velocity profile in the bearing channel reveal an exponential distribution of the velocity field next to the bearing surface for very high strain-rates[3] [15].

There are not many *in situ* experimental studies of the aluminium extrusion process because of the difficulties introduced by high temperatures and pressures. Two examples of such successful experiments are the measurement of the aluminium's temperature in the bearing channel using thermocouples attached to the die [16] and measurements of the pressure between the billet and the die [17]. Techniques directed at determining the bulk flow field in the die have also been developed using post experiment analysis [18, 19]. The procedure is to drill systematic holes in the aluminium billet prior to extru-

[3]This solution was obtained for aluminium flowing at 1 m/s in a 3 mm wide channel with stick boundary conditions.

sion and fill them with markers. After a given time, the extrusion is stopped and the extruded profile is cut open to obtain a picture of the aluminium flow field based on the movement of the markers. To study the position of the slip-line, the properties of the adhesive layer on the bearing surface and the development of ridges in this layer, a split die approach has been used. After the aluminium extrusion, the die is opened and its topology studied [8] . These measurements, however, are taken after the extrusion and do not offer continuous observations of the evolving bulk flow field nor of the slip-line.

1.1.3 The slip-line as a fracture front

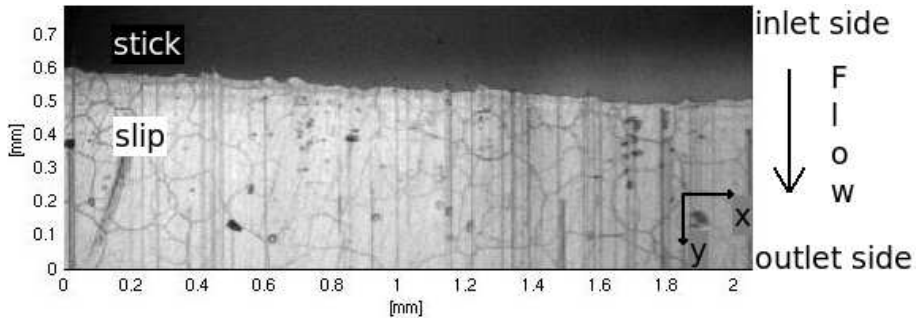

Figure 1.4: An *in situ* image of the bearing surface in the extrusion experiment. At the transition from stick to slip boundary conditions, a mode II (in plane) shear fracture is opening in the flow direction. The fracture tip appears as a line, referred to as the slip-line, across the flowing material.

In our experimental setup, we have literally changed the viewpoint on the extrusion process, we observe the extruded material detach from the bearing surface. This transition, shown in Figure 1.4, resemble a fracture front of varying roughness. As an alternative viewpoint, we suggest considering the slip-line as a fracture front. The idea of the slip-line as the tip of a shear fracture opening towards the outlet of the die is schematically illustrated in Figure 1.5. We have confirmed the presence of an adhesive film on the bearing surface downstream from the slip-line. This suggests that the fracture is opening inside the extruded material, and not on the interface between the material and the bearing surface.

The focus in this thesis on the slip line dynamics is inspired by a recent series of studies into the dynamics of crack propagation [20, 21, 22, 23].

The groups of Måløy and Schmittbuhl have performed experiments on cracks opening in the plane between to transparent plates of the polymer PMMA that had been sintered together. The experiment yielded very good optical contrast that allowed extraction of the crack front and subsequent statistical analysis of the dynamics of this front. The motivation of their study was [20] that crack surfaces were observed to have a universal roughness. The fracture surface may be seen as the trace left behind by the fracture front. One should therefore expect universal scaling of certain dynamical measures of the fracture front and that a dynamical model would be able to link the dynamical behaviour and the geometrical trace (the fracture surface). Both geometrical measures of the self-affine fracture fronts [21] and dynamical measures of front jump sizes, bursts and avalanches [22, 23] have been published and linked to models of the process. Although the dream of universality has faded slightly [23] it seems to have been fruitful to focus on the fracture front in order to understand the dynamics of fracture better.

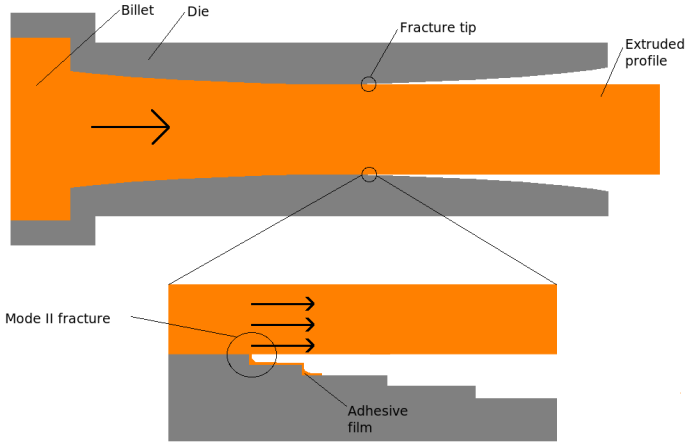

Figure 1.5: Schematic cross-sectional view of the extrusion die. This view is perpendicular to the viewing angle used in the optical image in Figure 1.4. The point where the extruded material slips from the die wall, and forms a profile, can be compared with the opening of a sliding mode II fracture. The magnified drawing illustrates an adhesive film that forms on the bearing surface during extrusion.

Chapter 2

Theory

2.1 Ductile deformation of crystals

As temperatures approach the melt temperature, the atoms and dislocations in rocks and metals become mobile. Deviatoric stress in these crystalline solids will result in creep deformation. At room temperature, rocks behave brittle and most metals require huge stresses to creep at this temperature. This is not the case for organic crystals. Already at room temperature plastic organic crystals deform by the same process that rocks and metals do at much higher temperatures, namely by creep. This process is time dependent, which means strain accumulates in the stressed solids over time. This phenomena is very different from brittle failure, where the deformation happens suddenly when stress is applied.

2.1.1 Creep deformation of crystalline solids at high temperatures

Deformation of crystalline solids is a wide-ranging subject. I will focus on the plastic creep deformation our model materials undergo in the extrusion process. Which mechanism contributes most to the deformation of crystalline solids depends on the temperature and stress the sample is exposed to. Between the transition temperature T_{plast} and the melting temperature T_{melt}, crystalline solids behave plasticly. The extrusion experiments described in this work were performed in the high temperature ($0.9T_{\text{melt}}$) and moderate pressure regime (atmospheric pressure). This section will therefore focus on mass transport in crystals under these conditions. The principal types of mobile species giving rise to mass transport in crystalline solids are lattice

defects; point defects, sub grain boundaries and dislocations [24].

When the temperature is well below the melt temperature, about $< 0.3T_{\text{melt}}$ for metals, the strain of stressed crystals is governed by dislocation glide. The flow rate is controlled by obstacles impeding the gliding mobile dislocations. As the gliding dislocations are pinned, the mass transport at these temperatures is limited [25].

At high temperatures ($> 0.85T_{\text{melt}}$) and extremely low stresses lattice vacancies allow atoms to diffuse through the crystal grains. Atoms migrate by jumping into neighbouring vacant sites in the crystal lattice and by doing this cause the vacancy and atom to swap places. This behaviour can be described either by diffusing vacancies or equivalently by diffusing atoms. Since the behaviour is controlled by the diffusion of atoms or vacancies, it is called diffusion creep.

Under common ductile conditions involving high temperature and pressures, dislocations migrate through the lattice in addition to the vacancies. Vacancies can migrate to a dislocation edge where they accumulate and move the dislocation to an adjacent plane (see Figure 2.1). In this way dislocations can climb past obstacles and glide until they encounter new imperfections. In this case, the gliding mechanism accounts for almost all the strain in the specimen. The rate of climb is diffusion controlled, and therefore very temperature sensitive. This creep regime is called dislocation creep.

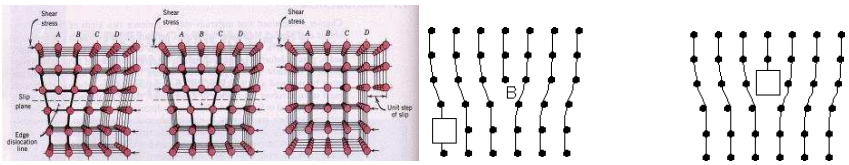

(a) (b)

Figure 2.1: 2.1(a) Side view of an edge dislocation gliding towards the right under shear stress. Dislocation glide can occur at both high and low temperatures. The process is often referred to as dislocation slip. 2.1(b) A vacancy diffuses to location B, causing the slip plane to climb one lattice vector up. Dislocations can overcome obstacles in their slip plane by climbing to an adjacent slip plane. The pictures are found in [26, 27]

In the steady state creep region, the strain rate $\dot{\epsilon}$ for a given temperature

T is related to the stress σ through the empirical expression

$$\dot{\epsilon}(T, \sigma) = Ae^{\frac{-E_c}{RT}}\sigma^n, \tag{2.1}$$

where R is the gas constant and the constant A is material property dependent [24]. The Arrhenius factor expresses how the strain rate depends on temperature and activation energy per mole E_c. The stress exponent, n, usually lies in the range 4-6 for crystalline solids in the plastic state. This strong dependence on stress is often seen in processes deforming by dislocation creep. The considerations and derivations leading up to Equation 2.1 are presented in in the following sections 2.1.2 and 2.1.3, dealing with diffusion creep and dislocation creep respectively.

2.1.2 Diffusion Creep

The diffusion of atoms through the interiors of the crystal grains govern creep deformation in crystalline solids at high temperatures subjected to very low stresses. This causes the grains to deform, leading to rock strain. We will show, following Turcotte [28], how strain rate depends on the stress in diffusion creep and that the relation has a Newtonian fluid behaviour.
Let us consider atoms in a simple cubic crystal lattice, see Figure 2.2(a), confined to their position by inter-atomic forces. Attractive long range forces act to reduce the distance between atoms and repulsive short range forces work to hold them apart. When attractive and repulsive forces balance each other out, the inter-atomic spacing has its equilibrium value b_0 and the lattice energy U exhibits a minimum value U_0(Figure 2.2(b))

Every single atom is trapped in a potential well. Therefore, fluctuations in the position away from b_0 (the equilibrium lattice spacing) require kinetic energy. An atom can move in the lattice if its kinetic energy exceeds the potential energy barrier ϕ_0 confining it to the lattice site. An atom can be considered to have escaped from its lattice position when oscillating with an amplitude greater than the lattice spacing b_0. If we think of the atoms as one dimensional harmonic oscillators, the maximum potential energy of an atom with vibration amplitude b_0 is, according to Hooks law, $\frac{1}{2}kb_0^2$. This gives us an expression for the minimum energy required to change lattice sites, i.e. the potential energy barrier ϕ_0

$$\phi_0 = \frac{1}{2}kb_0^2. \tag{2.2}$$

Here k is the spring constant, a measure for how strong the inter-atomic forces are. We can use k to relate ϕ_0 to the Einstein period τ. This period

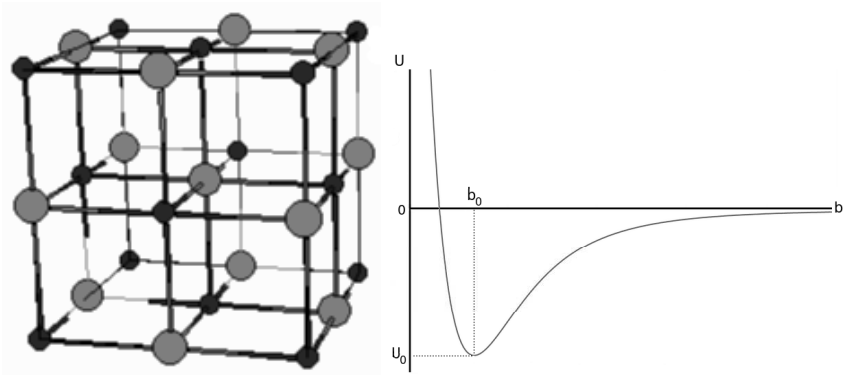

(a) (b)

Figure 2.2: (a) Atoms (NaCl) in a simple cubic lattice. The inter-atomic spacing is b_0 when the repulsive and attractive forces acting between the atom are equal. (b) The Lennard-Jones potential describes the energy of the interaction U between two atoms. This energy has a minimum when the atoms are b_0 apart.

is the reciprocal of the vibration frequency of an atom with mass m in the crystal lattice;

$$\tau = 2\pi\sqrt{\frac{m}{k}}.$$

If we solve Equation 2.2 for k and substitute into the expression for τ above, we obtain

$$\tau = 2\pi b_0\sqrt{\frac{m}{2\phi_0}}. \tag{2.3}$$

We will use this expression for τ later in the calculation to determine the rate at which vacancies and atoms jump to adjacent lattice sites.
Now we need an expression for the number of atoms n_{ϕ_0} having the required kinetic energy to escape from their sites; an energy equal to or larger than ϕ_0. According to Maxwell-Boltzmann distribution of energy, the number of atoms per unit volume dn_{ϕ_0} with energies in the interval $[\phi, \phi + d\phi]$ is

$$dn_{\phi_0} = 2n\sqrt{\frac{\phi}{\pi(k_BT)^3}}e^{-\frac{\phi}{k_BT}}\quad d\phi,$$

where n is the total number of atoms per unit volume, T the temperature and k_B is the Boltzmann constant. We sum up the number of atoms having

energy large enough to jump to neighbouring lattice sites by integrating the energy distribution from $\phi = \phi_0$ to $\phi = \infty$

$$n_{\phi_0} = \int_{\phi_0}^{\infty} dn_{\phi_0} = \frac{2n}{\sqrt{\pi(k_B T)^3}} \int_{\phi_0}^{\infty} \phi^{\frac{1}{2}} e^{-\frac{\phi}{k_B T}} \, d\phi = \frac{4n}{\sqrt{\pi}} \int_{u_0}^{\infty} u^2 e^{-u^2} \, du$$

with the change in variables $u = (\phi/k_B T)^{\frac{1}{2}}$ and $u_0 = \left(\frac{\phi_0}{k_B T}\right)^{\frac{1}{2}}$. This integral is then solved using integration by parts [1] to give

$$\frac{4n}{\sqrt{\pi}} \int_{u_0}^{\infty} u \left(u e^{-u^2}\right) \, du = \frac{4n}{\sqrt{\pi}} \left(\left[-\frac{1}{2} u e^{-u^2} \right]_{u_0}^{\infty} + \frac{1}{2} \int_{\frac{\phi_0}{k_B T}}^{\infty} {}^{\frac{1}{2}} \, e^{-u^2} \, du \right) \quad (2.4)$$

$$= n \left(2 \left(\frac{\phi_0}{\pi k_B T} \right)^{\frac{1}{2}} e^{-\left(\frac{\phi_0}{kT}\right)} + \operatorname{erfc}\left(\left(\frac{\phi_0}{k_B T} \right)^{\frac{1}{2}} \right) \right). \quad (2.5)$$

Most atoms in the lattice, $n - n_{\phi_0}$, are confined to their sites. Therefore, the potential barrier ϕ_0 must be much larger than the average energy for the atoms in the lattice $\frac{3}{2}kT$. This means that $\phi_0/kT >> 1$ and we can simplify Equation 2.4 by using the asymptotic formula for the complementary error function.

$$\operatorname{erfc}\left(\left(\frac{\phi_0}{k_B T} \right)^{\frac{1}{2}} \right) \approx \left(\frac{kT}{\pi \phi_0} {}^{\frac{1}{2}} \right) e^{-\frac{\phi_0}{k_B T}}, \quad (2.6)$$

which is valid when the argument of the error function is much larger than unity. The simplified expression for the number of atoms able to move is then

$$n_{\phi_0} = n \left(2 \left(\frac{\phi_0}{\pi k_B T} \right)^{\frac{1}{2}} + \left(\frac{kT}{\pi \phi_0} {}^{\frac{1}{2}} \right) \right) e^{-\frac{\phi_0}{k_B T}} \, , \quad (2.7)$$

where the last term can be neglected when $\phi_0/kT >> 1$. The simplified and final expression for n_{ϕ_0} is then

$$n_{\phi_0} = 2n \left(\frac{\phi_0}{\pi k_B T} \right)^{\frac{1}{2}} e^{-\frac{\phi_0}{k_B T}} \, . \quad (2.8)$$

Thus the fraction of atoms in the lattice having enough energy to jump the potential barrier ϕ_0 is given by the ratio n_{ϕ_0}/n. From the exponential term

[1] Where we have used that the substitution $s = u^2$ gives

$$\int u e^{-u^2} du = \frac{1}{2} \int e^{-x} dx = \frac{1}{2} e^{-x} = \frac{1}{2} e^{-u^2}.$$

in Equation 2.8, we see that this fraction is highly temperature sensitive.

The principal mobile species in crystal lattices are defects; point defects, sub-grain boundaries and dislocations. Vacancies are one form of point defects, which are open sites in the lattice. They allow atoms to diffuse in the crystal. An atom, whose energy exceeds the potential barrier, can jump to an adjacent vacancy. The site originally occupied by the atom becomes vacant. One can think of this as the vacancy migrating through the crystal lattice. In this way, the flow of vacancies relates to mass transportation in crystals and therefore also creep deformation. The relation between migration of atoms and vacancies makes the diffusion rate of vacancies interesting. The frequency, $\Gamma_{v,+x}$, at which a given vacancy jumps to the site in the positive x direction is the product of the probability for an atom in that site having the required barrier energy, n_{ϕ_0}/n, and the frequency with which the atom is moving towards the vacancy. The atom can move in 6 directions in an Einstein period ,τ, thus the probability for it to move towards the vacancy is $1/6\tau$. This gives

$$\Gamma_{v,+x} = \frac{n_{\phi_0}}{n6\tau}. \tag{2.9}$$

If we insert Equation 2.3 for τ and Equation 2.8 for n_{ϕ_0} into the expression for the rate shown above we get

$$\Gamma_{v,+x} = \frac{\phi_0}{6\pi b}\left(\frac{2}{\pi m k_B T}\right)^{\frac{1}{2}} e^{-\frac{\phi_0}{k_B T}} \ . \tag{2.10}$$

Note that vacancy jump frequency is the same for the positive and negative x direction and the derivation of $\Gamma_{v,-x}$ is the same as for $\Gamma_{v,+x}$. If we assume that there are as many vacancies ,n_v, per unit volume in the crystal lattice as there are atoms with energy sufficient to overcome the potential barrier we have,

$$n_v = n_{\phi_0} = 2n\left(\frac{\phi_0}{\pi k_B T}\right)^{\frac{1}{2}} e^{-\frac{\phi_0}{k_B T}} \ . \tag{2.11}$$

Further, we assume there is a gradient of vacancy density in the crystal in the x direction. The number of vacancies per unit volume at position x in the crystal is $n_v(x)$. The number of vacancies per unit area in the atom plane perpendicular to the x-direction at x is then $n_v(x)b_0$, where b_0 is the atom spacing, ie. thickness of the atom layer. In the adjacent plane at $x + b_0$, the vacancy density per area is $n_v(x + b_0)b_0$. The total rate of vacancy flow per unit area between the planes at x and $x + b_0$ is

$$J_{v,x} = \Gamma_{v,+x} n_v(x) b_0 - \Gamma_{v,-x} n_v(x + b_0) b_0.$$

Since the jump frequency $\Gamma_{v,+x} = \Gamma_{v,-x}$ we can write

$$J_{v,x} = -b_0^2 \Gamma_{v,+x} \left(\frac{n_v(x+b_0) - n_v(x)}{b_0} \right).$$

The following approximation is valid when the change in the vacancy density is small between two adjacent planes separated by b_0.

$$\left(\frac{n_v(x+b_0) - n_v(x)}{b_0} \right) = \frac{dn_v}{dx}.$$

The expression for the vacancy flux then becomes

$$J_{v,x} = -b_0^2 \Gamma_{v,+x} \frac{dn_v}{dx}. \tag{2.12}$$

The vacancy flux is proportional to the vacancy density gradient, and is positive when moving from an area in the crystal with high vacancy density to one with lower vacancy concentration. To obtain a more familiar form of the expression for vacancy flux, we denote the prefactor in Equation 2.12 as the diffusion coefficient for vacancies

$$D_v = -b_0^2 \Gamma_{v,+x}, \tag{2.13}$$

and we get Fick's first law of diffusion;

$$J_{v,x} = -D_v \frac{dn_v}{dx}. \tag{2.14}$$

By substituting Equation 2.10 for $\Gamma_{v,+x}$ into Equation 2.13 we find that the diffusion coefficient is given by

$$D_v = \frac{\phi_0 b_0}{6\pi} \left(\frac{2}{\pi m k_B T} \right)^{\frac{1}{2}} e^{-\frac{\phi_0}{k_B T}}.$$

In the framework of vacancy diffusion, we can find an expression for the atom flux $J_{a,x}$. Imagine a crystal containing two species of atoms A and B (see Figure 2.3). Let the concentration of A in the lattice be nonuniform, ie. there exists a gradient in the x direction in the A-atom density per unit volume. The existence of vacancies allows the atoms to diffuse through the crystal interior where atoms migrate by jumping into adjacent vacant sites. The initial nonuniform distribution of A-atoms will become uniform throughout the crystal with time as a result of the random transport of atoms in the crystal.

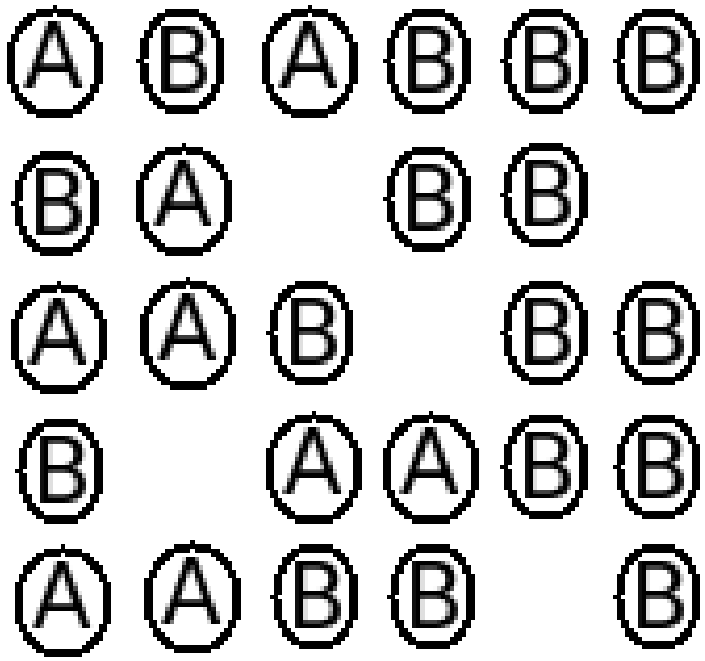

Figure 2.3: Illustration of a crystal with vacancies (denoted by empty sites) containing two species of atoms, A and B. There is a gradient in concentration of A atoms. With time, atoms will randomly jump into neighbouring vacant sites. This will gradually erase the nonuniform distribution of A atoms in the crystal. Eventually the concentration of A and B atoms will be uniform throughout the crystal.

The frequency $\Gamma_{A,+x}$ describes how often a given A-atom jumps in the positive x direction in the lattice. The jump rate is determined by three factors:

First, the jumping A-atom must have enough energy to overcome the potential barrier ϕ_0. The probability for this is given by the fraction $n_{A,\phi_0}/n_A$ (n_{A,ϕ_0} is the number of A-atoms having enough energy to jump and n_A is the total number of A-atoms). The fraction of atoms meeting this requirement is independent of atom species, in fact it is only dependent on temperature (see Equation 2.8). Therefore, the probability for an A-atoms energy to exceed ϕ_0 is given by

$$\frac{n_{A,\phi_0}}{n_A} = \frac{n_{\phi_0}}{n}.$$

The next requirement is that the adjacent site in x direction of the A-atom is vacant n_v/n. The last factor is how often the A-atom moves towards

the vacant site $1/6\tau$. This gives

$$\begin{aligned}\Gamma_{A,+x} &= \frac{n_{\phi_0}}{n}\frac{n_v}{n}\frac{1}{6\tau} \\ &= \frac{n_v}{n}\frac{n_{\phi_0}}{6\tau n}\end{aligned}$$

as the jump frequency for A-atoms in the x direction. Comparing with Equation 2.9, we see the relation between the jump frequencies for vacancies and A-atoms

$$\Gamma_{v,+x} = \frac{n_v}{n}\Gamma_{A,+x}.$$

The derivation of an expression for the A-atom flux is analogous to the one for vacancy flux (Equation 2.9 to Equation 2.14). The results only differ in the factor n_v/n;

$$J_{A,x} = -D\frac{dn_v}{dx}, \qquad where \;\; D = \frac{n_v}{n}D_v. \tag{2.15}$$

From Equation 2.11 we get

$$\frac{n_v}{n} = 2\left(\frac{\phi_0}{\pi kT}\right)^{\frac{1}{2}} e^{-\frac{\phi_0}{k_B T}}.$$

By using this expression, the diffusion coefficient for atoms diffusing through the crystal lattice becomes

$$\begin{aligned}D = \frac{n_v}{n}D_v &= \left[2\left(\tfrac{\phi_0}{\pi kT}\right)^{\frac{1}{2}} e^{-\frac{\phi_0}{k_B T}}\right]\left[\frac{\phi_0 b}{6\pi}\left(\frac{2}{\pi m k_B T}\right)^{\frac{1}{2}} e^{-\left(\frac{\phi_0}{kT}\right)}\right] \\ &= \sqrt{\frac{2}{m}}\frac{b_0\phi_0^{3/2}}{3\pi^2 kT}e^{-2\frac{\phi_0}{k_B T}}.\end{aligned}$$

The equation above can be rewritten to use the unit mole instead of the number of molecules (or atoms). We use the universal gas constant $R = N_A k_B$ (N_a is Avogadro's number), the potential energy barrier per mole $E_c = N_A\phi_0$ and the atomic mass per mole $M = N_A m$, to obtain

$$D = \frac{bE_c^{\frac{3}{2}}}{3\pi^2 RT}\sqrt{\frac{2}{M}}e^{-2\left(\frac{E_c}{RT}\right)}. \tag{2.16}$$

Since the barrier energy E_c (ϕ_0) is dependent on pressure and temperature, the expression

$$D = D_0 e^{-\left(\frac{E_a + pV_a}{RT}\right)} \tag{2.17}$$

is often used for the diffusion constant. The frequency factor D_0 neglects the dependence of temperature in the prefactor of Equation 2.16. The activation

energy per mole E_a and the activation energy per volume V_a account for the temperature and pressure dependence of diffusion respectively. Thus, when the pressure increases, there become fewer vacancies in the lattice and the potential barrier between sites increases. D_0, E_a and V_a are usually determined experimentally.

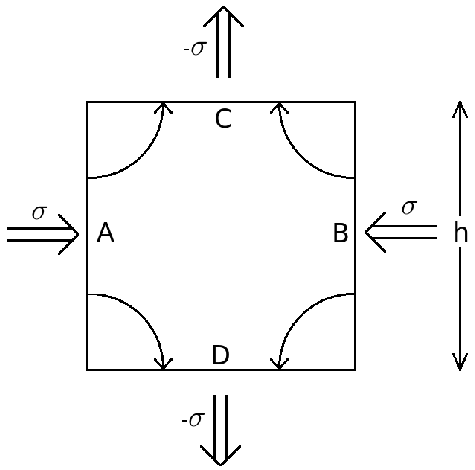

Figure 2.4: Figure shows a crystal where compressive stresses σ are applied to sides A and B, and a tensional stress applied to sides C and D. The last two sides of the cube, E and F, are in the plane of the paper. The arrows indicates the flux of atoms in the stressed crystal. The atom flux is induced by the reduction in the number of vacancies at sides A and B and with the increase in vacancy density at sides C and D. The diffusion creep in the crystal will lead to a lengthening of the crystal in the y-direction and a shortening in the x-direction. Note that for diffusion creep to be the prevailing deformation mechanism, the temperature must be high ($> 0.85T_{\text{melt}}$) and the stresses small. When the stresses are larger, dislocation creep is responsible for most of the mass-transport within the crystal.

We will now investigate how applying a differential stress to a crystal changes the diffusion creep behaviour, in other words; how the strain rate $\dot{\epsilon}$ depends on the stress σ. Consider a crystal cube with sides of length h under compressive stress σ in the x-direction and tensional stress $-\sigma$ in the y-direction (illustrated in Figure 2.4). Note that in a poly-crystal, the crystal dimension h is a measure of the distance between the grain boundaries.

There is no stress applied in the z-direction. The stresses will make atoms diffuse from the sides under compression (A and B) to the ones under tension (C and D). This can be understood by recognising that the diffusion of vacancies occurs in the opposite direction of the atom diffusion. At the compressed sides A and B, the number of vacancies per unit volume will decrease from n_v to $n_{v,A}$ and $n_{v,B}$. The tensional stress will increase the number density of vacancies at the sides C and D from n_v to $n_{v,C}$ and $n_{v,D}$. As a result, a flux of vacancies will go from side C (and D) to sides A and B, this is equivalent to a flux of atoms in the opposite direction. The vacancy densities $n_{v,E}$ and $n_{v,F}$ of the two unstressed sides of the crystal, E and F, will remain n_v. The flux of vacancies from A and B into E and F will equal the flux from E and F into C and D, therefore, the total flux in z-direction will be zero. Note that vacancies will diffuse from C and D via E and F to A and B. Mass conservation requires the strain in the crystal in the x- and y-direction to be of equal size, but with opposite sign ($\epsilon_{xx} - \epsilon_{yy} = 0$). The strain in the z-direction will be 0 ($\epsilon_{zz} = 0$).

We can describe the the vacancy flux within the crystal with Fick's law of diffusion Equation 2.14. In the stressed crystal the mean separation between two adjacent sides is the distance between the centre points of two sides, $h/\sqrt{2}$. The flux of vacancies from sides A to C is proportional to the gradient in vacancy density. We denote the flux between sides A and B by $J_{v,AB}$ and so on for the other sides. The expression for the vacancy flux between all the adjacent walls can be expressed as

$$J_{v,AC} = J_{v,AD} = J_{v,BC} = J_{v,BD} = D_v \left(\frac{n_{v,C} - n_{v,A}}{h/\sqrt{2}} \right) \tag{2.18}$$

$$J_{v,AE} = J_{v,AF} = J_{v,BE} = J_{v,BF} = D_v \left(\frac{n_v - n_{v,A}}{h/\sqrt{2}} \right) \tag{2.19}$$

$$J_{v,CE} = J_{v,CF} = J_{v,DE} = J_{v,DF} = D_v \left(\frac{n_{v,C} - n_v}{h/\sqrt{2}} \right).$$

The flux above is expressed per unit time and area. We can obtain the number of vacancies that flow between the adjacent sides by dividing the flux over the area it passes through. This area ($\sqrt{2}h^2/2$) is half of the diagonal ($h/\sqrt{2}$) times the height of the crystal h. The change in strain associated with each vacancy is $-b_0^3/h^3$. The expressions for the strain-rate in the x-

and y-direction becomes

$$\dot{\epsilon}_{xx} = \frac{b_0^3}{h^3}\frac{h}{\sqrt{2}}(J_{v,AC} + J_{v,AD} + J_{v,BC} + J_{v,BD} + J_{v,AE} + J_{v,AF} + J_{v,BE} + J_{v,BF})$$
$$\dot{\epsilon}_{yy} = -\frac{b_0^3}{h^3}\frac{h}{\sqrt{2}}(J_{v,AC} + J_{v,AD} + J_{v,BC} + J_{v,BD} + J_{v,CE} + J_{v,CF} + J_{v,DE} + J_{v,DF})$$

We can eliminate the flux in the above expressions for strain-rate by using Equation 2.18. A further simplification can can be done using $1/b_0^3 = n$, where n is the total number of lattice sites in a unit volume. We can now write

$$\dot{\epsilon}_{xx} = \frac{4D_v}{nh^2}(n_{v,C} - 2n_{v,A} + n_v)$$
$$\dot{\epsilon}_{yy} = -\frac{4D_v}{nh^2}(2n_{v,C} - n_{v,A} - n_v).$$

The dependence of stress in the equations for strain-rate comes from the stress dependence of vacancy density n_v. At the sides where the stress is applied the vacancy density per unit volume becomes

$$n_{v,A} = n_{v,B} = 2n\left(\frac{E_c}{\pi RT}\right)^{\frac{1}{2}} e^{-\left(\frac{E_c+\sigma V_a}{RT}\right)}$$
$$n_{v,C} = n_{v,D} = 2n\left(\frac{E_c}{\pi RT}\right)^{\frac{1}{2}} e^{-\left(\frac{E_c-\sigma V_a}{RT}\right)}.$$

These expressions only differ from the expression for n_v (the vacancy density in the absence of a stress Equation 2.11) by the σ in the exponent. This is the same trick as we used in the definition for the diffusion constant when including the pressure (Equation 2.17). When diffusion creep is the prevailing deformation mechanism, the stresses are extremely small. Therefore, $\sigma V_a/RT << 1$ and we can write

$$\frac{n_{v,A}}{n_v} = e^{-\left(\frac{\sigma V_a}{RT}\right)} \approx 1 - \frac{\sigma V_a}{RT}$$
$$\frac{n_{v,C}}{n_v} = e^{\left(\frac{\sigma V_a}{RT}\right)} \approx 1 + \frac{\sigma V_a}{RT},$$

where we have divided by Equation 2.11 and used the first order series expansion of e^x. The strain-rates now becomes

$$\dot{\epsilon}_{xx} = \tfrac{4n_vD_v}{nh^2}\left(1 + \tfrac{\sigma V_a}{RT} - 2\left(1 - \tfrac{\sigma V_a}{RT}\right) + 1\right) = \tfrac{12n_vD_vV_a}{nh^2RT}\sigma$$
$$\dot{\epsilon}_{yy} = -\tfrac{4n_vD_v}{nh^2}\left(2\left(1 + \tfrac{\sigma V_a}{RT}\right) - 1 + \tfrac{\sigma V_a}{RT} - 1\right) = -\tfrac{12n_vD_vV_a}{nh^2RT}\sigma.$$

The diffusion constant for atoms D is related to the diffusion constant for vacancies D_v through Equation 2.15. When exchanging D_v with D we obtain

$$\dot{\epsilon}_{xx} = -\dot{\epsilon}_{yy} = \frac{12 V_a D}{h^2 RT}\sigma. \tag{2.20}$$

This relation shows that the strain-rate increases linearly with stress (the stress-exponent equals unity). This is in agreement with the prediction that diffusion creep exhibits Newtonian fluid behavior.

2.1.3 Dislocation Creep

It is not only diffusion of vacancies that leads to creep in crystalline solids. Another mechanism for deformation is dislocation creep. This type of creep needs high stress relative to the shear modulus of the material to take place, whereas diffusion creep occurs even at very low stress. As the name suggests, there are the dislocations that accommodate the strain in dislocation creep. We only need the superposition of two basic dislocation types to describe all forms of dislocations in crystals. The two basic types are edge (shown in Figure 2.1) and screw dislocations. A good qualitatively description of them can be found in [28].

Solids are deformed when the dislocations move by either dislocation climb or dislocation slip. The former dislocation creep mode, dislocation climb, allows a dislocation to move by adding or subtracting atoms from the plane that define the dislocation. Figure 2.1(b) illustrates this process. Since this is not a mass-conserving process, atoms are required to diffuse in the lattice to change the position of the dislocation. The diffusion makes this a slow process compared to dislocation slip. In this mode, the atom plane containing the dislocation actually gets longer or shorter. While in the case of dislocation slip, shear stress transfers the dislocation to an adjacent atomic plane. Figure 2.1(a) illustrates this. The latter process is mass-conserving. Therefore, no atom diffusion is required and the slip deformation can happen much faster than the climb deformation.

The relationship between the strain rate $\dot{\epsilon}$ and stress σ for diffusion creep is dependent of the inter grain boundary distance h. In dislocation creep the deformation is facilitated by dislocations, rather than by grain boundaries as in the case of diffusion creep. We can exploit this to obtain a power-law relation between $\dot{\epsilon}$ and σ for dislocation creep. The approach is to replace h

in Equation 2.20 with the mean spacing between dislocations h_d

$$\dot{\epsilon}_{xx} = -\dot{\epsilon}_{yy} = \frac{12V_aD}{h^2RT}\sigma. \tag{2.21}$$

The mean distance between dislocations is determined from the dislocation density n_d in the crystal. The dislocation density is defined as the total length of dislocations per unit volume of the material. This gives n_d units of $m/m^3 = m^{-2}$. As the units indicate, an equivalent definition of n_d is the number of dislocation lines intersecting a unit area. In metals, the dislocation density is usually of the order $10^{10}m^{-2}$ and increases with strain hardening. The spacing and volume density of dislocations are related by

$$h_d = \sqrt{\frac{1}{n_d}}.$$

Under a wide range of conditions [28], the mean dislocation spacing can be approximated by

$$h_d = \frac{|b|G}{\sigma},$$

where $|b|$ is the magnitude of the Burgers vector (hence the size of the dislocation) and G is the shear modulus. When we substitute the above for h_d in Equation 2.21, the relation between $\dot{\epsilon}$ and σ becomes

$$\dot{\epsilon} = \frac{12V_aD}{|b|^2G^2RT}\sigma^3. \tag{2.22}$$

This shows that dislocation creep gives a non-Newtonian relationship between $\dot{\epsilon}$ and σ. The power-law exponent, n, is 3 in this example, while other approaches can yield different values, typically in the satisfying $3 \leq n \leq 10$. Common for all the derivations is the non-Newtonian behaviour they prescribe. Equation 2.22 becomes identical with Equation 2.1 when inserting the general power-law exponent n for 3 and summarising the material properties in a constant A.

2.1.4 Shear flow

This section discusses the flow of power-law fluids (or non-Newtonian materials) in a channel. The model materials used in the experiments and presented in this thesis, Succinonitrile and Camphene, are examples of such non-Newtonian materials [29]. See Table 3.2 for a list of the characteristics for these materials. The non-linear stress and strain-rate (or velocity gradient) relation in these materials is described by the power-law in Equation 2.1.

Let us consider the stationary and laminar flow of a non-Newtonian material in a channel. The thickness of the channel is h with stationary walls at $y = \pm h/2$, and the width of the channel is so large that boundary effects from the walls in this dimension can be ignored. The shear stress τ in the material is related to the velocity gradient across the height of the channel through

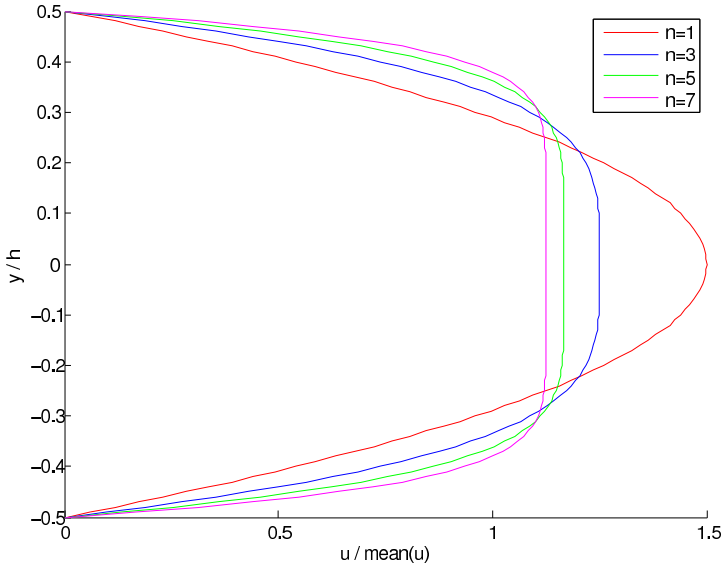

Figure 2.5: The velocity profiles for non-Newtonian material flowing in a channel of height h with zero velocity at the walls at $y/h \pm 0.5$. The profiles are for power-law exponent $n = 1$ (Newtonian), 3, 5 and 7. For higher n, the flow profile becomes more plug-like.

$$\frac{du}{dy} = B\tau^n, \tag{2.23}$$

where u is the flow velocity,B is a positive material dependent constant and n is the materials power law exponent. The ratio of the flow velocity u to the mean velocity $\bar{u}$ across the thickness h of the channel is given by

$$\frac{u}{\bar{u}} = \left(\frac{n+2}{n+1}\right)\left[1 - \left|\frac{2y}{h}\right|^{n+1}\right], \tag{2.24}$$

where $y \in [-h/2, h/2]$ is the position in the channel [28]. In Figure 2.5 this velocity ratio profile is plotted for various values of n, note that $n = 1$ corresponds to Newtonian flow. From the figure we see that increasing n gives larger velocity gradients close to the walls. According to Equation 2.23, this

means that the shear stress close to the walls also increases with larger n. The effective viscosity of a non-Newtonian material is proportional to τ^{1-n} [28]. The latter means that where τ is large, the materials viscosity is low (ie. close to the walls), whilst the viscosity is high where τ is small (ie. the middle of the channel). This effect becomes more pronounced as n grows. The stress dependence of the effective viscosity makes materials with higher power-law exponents n exhibit a more plug-like velocity profile.

2.1.5 Coulomb friction criteria

Several friction models have been suggested for describing the friction inside the bearing channel [30, 31] and because the mechanisms of friction are not well understood, it is not established which model adresses the problem best. This section discusses the application of a Coulomb friction model to describe the friction at the bearing surface inside the extrusion die. Numerical implementation of this model is reported to generate results similar to what is reported from experimental studies [12].

In extrusion, the normal pressure at the bearing surface, p, decreases from the inlet towards the outlet of the bearing channel. Let us, for simplicity, consider a bearing channel with parallel walls. Close to the inlet of the channel, where q is largest, there is stick between the bearing and the extruded profile, while at the outlet there is sliding friction at the material-bearing interface. The transition from stick to slip takes place where the internal shear stress in the boundary material layer[2], τ, reaches the value of the frictional shear stress, τ_f, at the interface. In case of Coulomb friction,

$$\tau_f = \mu\sigma_n \tag{2.25}$$

where σ_n is the compressional stress on the material at the bearing surface. The velocity profile in the channel can be assumed to be constant upstream from the slip-line, as illustrated in Figure 2.6, when the shear-deformation heating of the material is neglected. This assumption is justified by the stress-independence in Equation 2.24, the expression for the velocity profile for a non-Newtonian fluid in a channel. The strain-rate, $\dot{\epsilon}$, is proportional to the derivative across the velocity profile, therefore, the $\dot{\epsilon}$ in the channel is also constant at a given distance from the wall. Figure 2.6 illustrates the

[2]The boundary layer refers to the thin layer of material flowing in the vicinity of the bearing surface. In the stick region of the bearing channel, this layer is heavily sheared because there is zero a velocity boundary condition at the bearing surface.

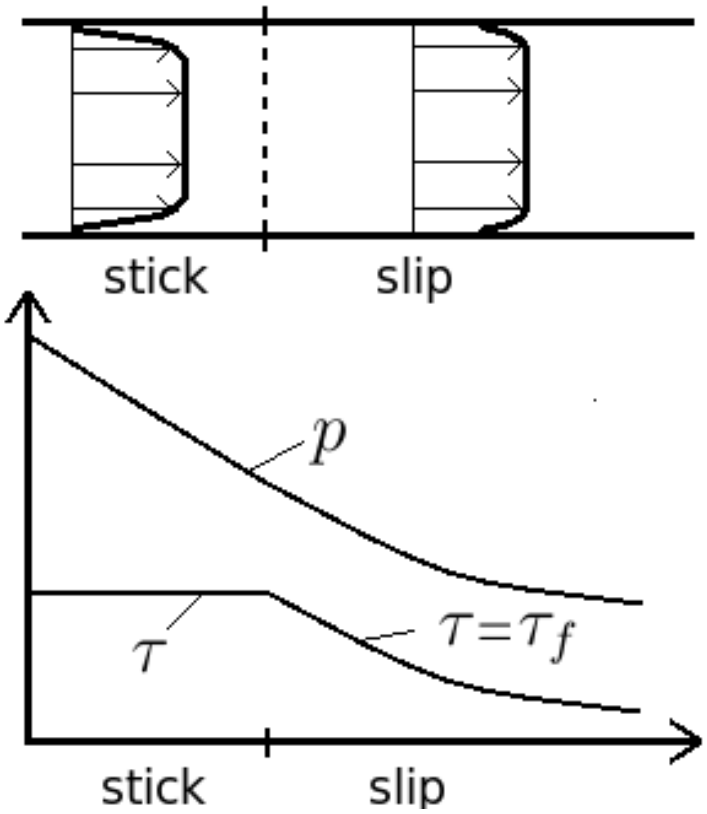

Figure 2.6: **Top**: Schematic view of the velocity along the bearing channel. Flow is from left to right. **Bottom**: Relation between the normal pressure p, equal to σ_n in Equation 2.25, and the shear stress, τ, in the material immediately next to the bearing surface. The Coulomb friction force at the bearing surface, τ_f, is acting the opposite direction of τ. When $\tau = \tau_f$, the boundary conditions in the channel change from sticking to the wall to sliding friction.

relation between τ, τ_f, and the slip-line in a channel with parallel bearing surfaces. In such a channel, the transition from stick to slip is often modeled as a stationaty line at the point where $\tau = \tau_f$.

2.2 Calculus of Variations

We will here present a brief introduction to calculus of variations to help the readers who are not familiar with this branch of calculus follow the Euler-Lagrange transformation concerning the image analysis tool in section 3.4. First, we will present a famous example explaining the method, and then

we will generalize the result to arrive at the Euler-Lagrange equation. The presentation is based on [32]

What is the shortest distance between two neighbouring points? The answer is a straight line as we will prove shortly. Calculus of variation is used to minimize various quantities, for example, a distance on a plane. Another example is the minimization of the energy functional in Section 3.4. Let us look closer at the problem of finding the geodesic of a surface (the geodesic is the term for the shortest distance between two points on a surface).

What we do, in practise, is to make the quantity in question stationary. In terms of ordinary calculus we set $f'(x) = 0$ to find the stationary points of $f(x)$. Then, we rely on physics or geometry to decide if we have found a maximum point, minimum point or a point of inflection with a horizontal tangent. Calculus of variations is based on the same principle, but the quantity to make stationary is a functional not a function. It is the integral

$$I(x, y, y') = \int_a^b F(x, y, y')dx \quad where \quad y' = \frac{dy}{dx}, \tag{2.26}$$

for which we want to find a maximum or minimum. In the case of finding the shortest curve $y(x)$ between the two points (x_1, y_1) and (x_2, y_2), it is the arc length $\int dS$ that must be minimized. The arc along the curve can be expressed by length as $\int ds = \int \sqrt{dx^2 + dy^2}$. When using the definition of y' from Equation 2.26, we can write $\sqrt{dx^2 + dy^2} = \sqrt{1 + y'^2}$. The quantity to minimize by varying the path $y(x)$ between the points is

$$I = \int_{x_1}^{x_2} \sqrt{1 + y'^2}dx, \tag{2.27}$$

which is Equation 2.26 with $F(x, y, y') = \sqrt{1 + y'^2}$. The $y(x)$ that minimizes this quantity is called an extremal. To find this extremal we want to consider the infinitely many curves (having a continuous second derivative, so we can differentiate them later) passing through the given endpoints. We can represent these varied curves algebraically by introducing a function $\eta(x)$, see Figure 2.7.

The function $\eta(x)$ goes to zero at the two endpoints, and has continuous second derivatives, but apart form this is completely arbitrary. All the curves passing through the two endpoints (x_1, y_1) and (x_2, y_2) can be expressed by

$$Y(x) = y(x) + \epsilon\eta(x), \tag{2.28}$$

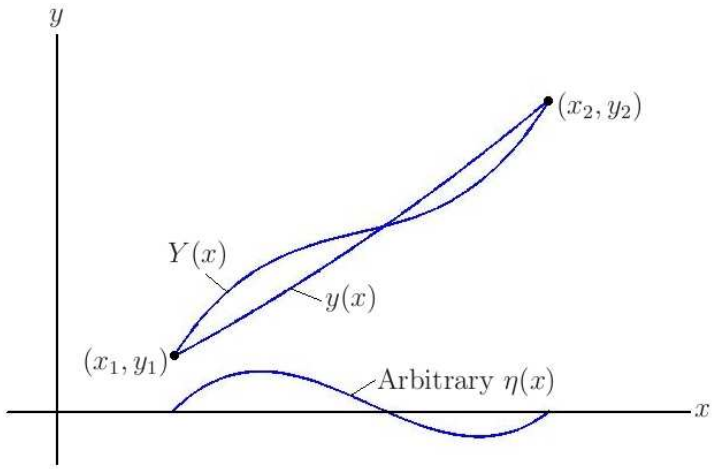

Figure 2.7: $Y(x)$ is the sum of the extremal curve $y(x)$ and the arbitrary function $\eta(x)$. Notice how $\eta(x)$ is zero at x_1 and x_2.

where $y(x)$ is the desired extremal and ϵ is a parameter. Out of all the curves $Y(x)$, we want to pick out the one making

$$I = \int_{x_1}^{x_2} \sqrt{1 + Y'^2} dx, \tag{2.29}$$

as small a possible. When $\epsilon = 0$, we have that $Y(x) = y(x)$. If the integral I has its minimum value when $\epsilon = 0$, $y(x)$ must be the extremal we are looking for. These two requirements can be written as

$$\frac{dI}{d\epsilon} = 0 \quad and \quad \epsilon = 0. \tag{2.30}$$

By differentiating Equation 2.29 with respect to ϵ and then evaluating the resulting expression at $\epsilon = 0$ we find the expression for the extremal $y(x)$. Here we differentiate Equation 2.29 using the chain rule ($\frac{\partial F(Y(\epsilon))}{\partial \epsilon} = \frac{\partial F}{\partial Y'}\frac{\partial Y'}{\partial \epsilon}$) and get

$$\frac{dI}{d\epsilon} = \int_{x_1}^{x_2} \frac{1}{2} \frac{1}{\sqrt{1 + Y'^2}} 2Y' \frac{\partial Y'}{\partial \epsilon} dx. \tag{2.31}$$

By first differentiating Equation 2.28 with respect to x and then with respect to ϵ we get

$$\begin{aligned} Y'(x) &= y'(x) + \epsilon \eta'(x) \\ \frac{\partial Y'}{\partial \epsilon} &= \eta'(x). \end{aligned}$$

Inserting this expression into Equation 2.31 gives

$$\frac{dI}{d\epsilon} = \int_{x_1}^{x_2} \frac{Y'\eta'}{\sqrt{1+Y'^2}} dx. \tag{2.32}$$

Evaluating the expression shown above at $\epsilon = 0$ from Equation 2.28 we see this is the same as setting $Y'(x) = y(x)$. If we then demand that $\frac{dI}{d\epsilon} = 0$ we have

$$\left(\frac{dI}{d\epsilon}\right)_{\epsilon=0} = \int_{x_1}^{x_2} \frac{y'\eta'}{\sqrt{1+y'^2}} dx = 0. \tag{2.33}$$

This can be integrated by parts to give

$$\left(\frac{dI}{d\epsilon}\right)_{\epsilon=0} = \left[\frac{y'}{\sqrt{1+y'^2}}\eta(x)\right]_{x_1}^{x_2} - \int_{x_1}^{x_2} \eta(x)\frac{d}{dx}\left(\frac{y'}{\sqrt{1+y'^2}}\right) dx = 0.$$

The first is zero because we defined $\eta(x)$ to be zero at the endpoints. Because $\eta(x)$ is an arbitrary function it must be that

$$\frac{d}{dx}\left(\frac{y'}{\sqrt{1+y'^2}}\right) = 0$$

for the expression to always be equal to zero. Integrating this expression with respect to x gives

$$\frac{y'}{\sqrt{1+y'^2}} = const.$$

This means that the slope of the curve $y'(x)$ between the two points is constant, ie. the extremal curve $y(x)$ is a straight line.

Instead of going through this process step by step for every problem, we can generalize the method by finding the differential equation that solves all later calculus of variation problems. The method is analogous to the one for the straight line, but this time we generalize. Again we consider all varied curves

$$Y(x) = y(x) + \epsilon\eta(x),$$

and define the quantity we want to make stationary

$$I(\epsilon) = \int_a^b F(x, y, y')dx.$$

We differentiate with respect to ϵ and using the chain rule on both the variables Y and Y' that are functions of ϵ, we obtain

$$\frac{dI}{d\epsilon} = \int_a^b \left(\frac{\partial F}{\partial Y}\frac{\partial Y}{\partial \epsilon} + \frac{\partial F}{\partial Y'}\frac{\partial Y'}{\partial \epsilon}\right) dx,$$

substituting Equation 2.28 and its derivative with respect to x into the integral, and requiring $(dI/d\epsilon)$ to be zero when $\epsilon = 0$ yields

$$\left(\frac{dI}{d\epsilon}\right)_{\epsilon=0} = \int_a^b \left[\frac{\partial F}{\partial y}\eta(x) + \frac{\partial F}{\partial y'}\eta'(x)\right] dx = 0 \tag{2.34}$$

Assuming that y'' is continuous, we can integrate the second term by parts to get

$$\int_a^b \frac{\partial F}{\partial y'}\eta'(x)dx = \left[\frac{\partial F}{\partial y'}\eta(x)\right]_a^b - \int_a^b \eta(x)\frac{d}{dx}\left(\frac{F}{y'}\right) dx,$$

where the first term is zero because $\eta(x)$ is defined to be zero in a and b. Substituting this expression into Equation 2.34 results in

$$\left(\frac{dI}{d\epsilon}\right)_{\epsilon=0} = \int_a^b \left[\frac{\partial F}{\partial y} - \frac{d}{dx}\frac{F}{y'}\right] \eta(x)dx = 0. \tag{2.35}$$

Since $\eta(x)$ is an arbitrary function, the expression in the square brackets must always be equal to zero such that

$$\frac{d}{dx}\frac{F}{y'} - \frac{\partial F}{\partial y} = 0.$$

This is the Euler-Lagrange equation. All calculus of variation problems can be solved by using this differential equation. First, define the integral that is to be stationary, then substitute the expression for the function F into the Euler-Lagrange equation, and solve the resulting differential equation.

2.3 Estimation of errors

We have estimated the standard deviation, σ, and mean standard deviation, σ_m, in our measurements using the measurement residuals, d. The theory behind this standard approach is splendidly explained in [33]. The error in the ith measurement, x_i, is estimated by its residual according to

$$d_i = x_i - \bar{x},$$

where $\bar{x}$ is the mean of a set of n measurements. The rms value of the residuals s, defined as

$$s^2 = \frac{1}{n}\sum_{i=1}^{n} d_i^2,$$

is used to estimate σ_m through

$$\sigma_m \approx \left(\frac{1}{n-1}\right)^{1/2} s.$$

In this thesis estimated values are quoted as $\bar{x} - \sigma_m$ unless otherwise stated.

Chapter 3

Experimental methods

In nature and in industry, the extrusion process is difficult to observe closely because of the extreme conditions normally involved. In geology, the process often takes place in subterranean systems or the scale is too large and too many parameters are involved to gain a qualitative insight into the process. In manufacturing applications, the scale and accessibility is more suited to studying extrusion, but the high temperatures and pressures involved often make the study both dangerous and complicated. The low yield stress of the model materials we work with enable us to use a miniature press operated at moderate pressures at room temperature. A natural place to start this chapter is with an overview of the process we are studying and the parameters that are adjusted in the experiment. The overview focuses on the processes taking place inside the die during extrusion. Later in this chapter, we present our experimental setup and methods. It may be helpful to briefly study Figure 3.1 before reading the following overview.

The objective of our experiments is to track the movement of the transition from stick to slip boundary conditions, also referred to as the slip-line, inside the die. We want to gain insight into the processes that form the extrudate[1] and the topology of the slip-line. For this purpose, we have designed transparent extrusion dies. They enable us to acquire *in situ* images of the plastic crystal material as it is thrusted through the die. Figure 3.2 shows the properties of the process inside the die that we determine from the images taken of the flowing material. These properties can be characterised as either quantitative and qualitative measures. The first category is comprised of the strain rate throughout the die and the slip-line position. Note that the strain-rate measure gives us information about the exit velocity of the

[1]The term extrudate refers to the finished profile, ie. the extruded material.

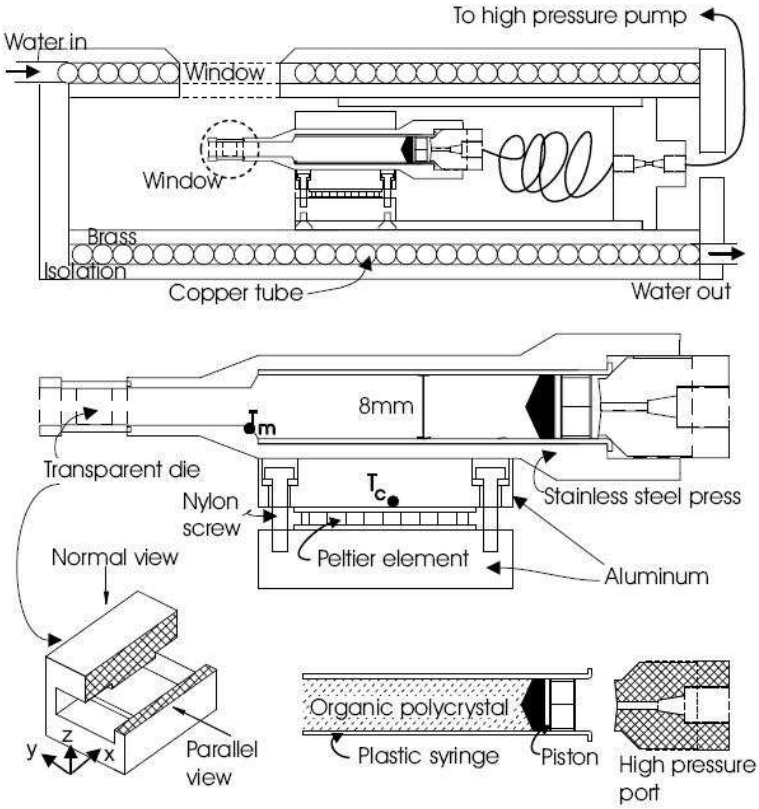

Figure 3.1: Cylindrical symmetric extrusion press. **Top**: The Extrusion press mounted on a brass sledge inside a temperature controlled and insulated cylinder. Temperature controlled water flows in the copper tubing surrounding the brass cylinder. The windows allow the die to be observed, both with a microscope objective and transmitted light (dashed circle). Micrometre screw to position the sledge is not drawn in. **Middle**: The miniature extrusion press mounted on a temperature controlled aluminium slab. The thermistor T_c works in a PID loop with the Peltier element to control the sample chamber temperature. **Bottom**: The syringe containing the annealed organic crystal is placed in the extrusion press. A nut with a high pressure port seals the press from behind, and connects it to a hydraulic pump. The sample is extruded through the transparent slit die.

material and the bulk flow velocity field. Examples of the qualitative information available in the extrusion movies are; large scale slip-line instabilities, formation and behaviour of an adhesive layer on the bearing surface, and how deposits in the adhesive layer scratches the extruded profile. During the extrusion, we continously measure the hydraulic pressure that pushes the material through the die.

The parameters we control in the experiment are as follows; ingot temperature, extrusion material composition, flow-rate, dimensions and curvature of the die. We have chosen to limit the parameter space by only varying die curvature and material composition in the different experiments. However, the average flow velocity can vary with different dies. This is because we assemble the dies by hand, which causes variation in the cross-sectional area of the dies. The nominal die opening[2] is $4 \times 1\ mm^2$. In dies with a smaller die opening the average flow velocity will increase and *vice versa*. The measured dimensions of the die opening for the dies we have used in the analysed experiments are presented in Table 4.2. The change in flow velocity caused by the variation in die opening for the different dies is very small. Therefore, we keep the flow rate, ie. the material flux, constant in the experiments rather than trying to achieve a constant flow velocity by adjusting the flow rate when changing dies.

[2]The term die opening refers to the cross-sectional area in the bearing channel at its narrowest point.

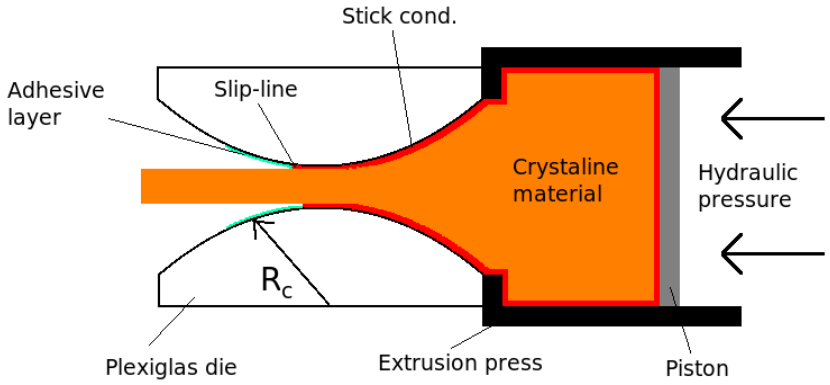

(a) Parallel view

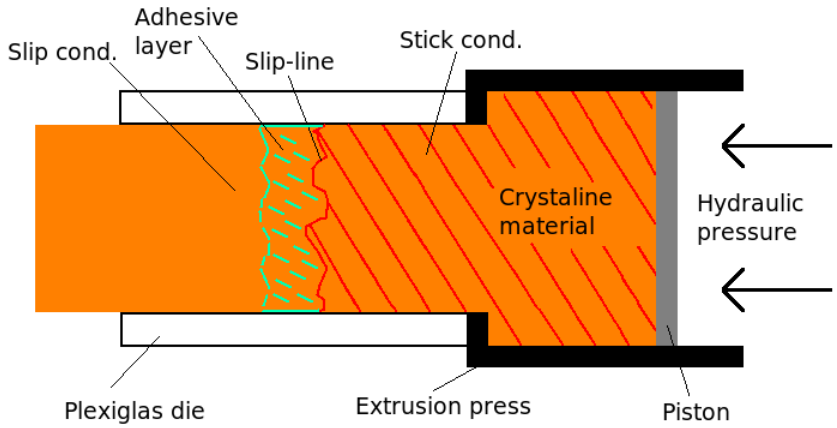

(b) Normal view

Figure 3.2: (a) A cross-sectional parallel view of the extrusion die displaying the curvature in the die. The radius of curvature, R_c, of the bearing surfaces is one parameter that we vary in the experiments (the curvature centre of curvature is chosen wrong in the figure to save space). The other parameter is the extrusion material, we have extruded two different organic crystals. The parallel viewing angle is used when we measure the bulk velocity. (b) Normal view of the extrusion die. The focus is on the surface on the extrusion profile. The slip-line is seen as a clear border between the stick region (shaded) and the slip region. As the names implies, in the stick region the material adheres to the die surface, and in the slip region it is detached from the die surface, also called bearing surface. For the sake of clarity, the adhesive layer that sometimes arises on the bearing surface is in (a) and (b) only drawn in the dimension perpendicular to the cross-section. In reality, this thin layer, when present, covers all the surfaces inside the die downstream from the slip-line.

3.1 Using an analog material for metal and rock

This section will first explain my choice of analog materials and then explain how they are treated in order to exhibit properties similar to metals and rock. To characterise the deformation of crystalline materials, such as metal and rock, without reaching the extreme temperature and pressure conditions where this normally occurs, one can study an analog material. This allows one to study the behaviour of the process in great detail at room temperature and moderate pressures.

In the experiments I have performed, the transition from ductile to brittle behaviour of plastic crystals has been used to gain insight into what is happening when metal and rocks undergo this transition. The first challenge is to find analog materials. The model materials should preferably have the features of being transparent and non-toxic.

3.1.1 Plastic organic crystals as analog material for metals and rocks

There is a group of organic crystals known to be very plastic compared to other crystals. This type of crystals is often referred to as plastic organic crystals. They recrystallise at room temperature and have the ease of plastic flow. Some even flow under gravity.
The first extensive study of the plasticity of organic crystals was performed by Michils [34]. He extruded a number of polycrystalline samples through a circular orifice of 1 mm and recorded the back pressure. The results were compared with the entropy of fusion[3] and orientational disorder of the crystals. From this, he found that plasticity increased with increasing orientational disorder. Michils also noted that the extruded samples showed the outward characteristics of crystalline solids, not of viscous fluid samples, making them ideal for metallurgists studying deformation at attainable conditions. Many studies have been performed using plastic crystals as an analog for minerals in rocks [35, 36, 37]. These studies have concentrated on the microstructural changes caused by various types of deformation.

Camphene and Succinonitrile (SCN) are transparent organic crystals that have been studied extensively by Jones et al. in a series of articles [29, 38, 39, 40, 41]. The microscopic mechanisms of plasticity for these materials have

[3]Entropy of fusion is the increas in entropy when a substance melt. Therefore, materials with low entropy of fusion needs less energy to to go from the organised crystalline solid state to the more disorganised liquid state.

Material	Hot extrusion temperature ($°C$)
Aluminium	400-500
Steel	1100-1300
Copper	650-1100
Succinonitrile	40
Camphene	22

Table 3.1: Hot extrusion temperatures for three commonly extruded materials including the temperatures at which we performed the analog material experiments. The term 'hot extrusion' refers to extrusion at temperatures above the recrystallisation temperature of the working material. The hydraulic pressure when extruding the metals is usually in the range 340-6700 bar, while our experiments are preformed with a back pressure in the 20-50 bar range.

been studied extensively with X-ray scattering, acoustic methods, Raman scattering and infrared studies, light scattering, and NMR [24].Since these materials have a high rotational degree of freedom, they flow plastically under moderate pressures even in the solid state. The compounds have low entropy of fusion and under stress they deform plastically without fracturing. Table 3.1 presents the extrusion temperatures for several common metals and the temperatures at which we extruded the analog materials.

Compound	Structure	T_{plast} ($°C$)	T_{melt} ($°C$)	E_c (kJ/mol)	n
Succinonitrile	bcc	-40	58	57	4.6
Camphene	bcc	-123	47	102	5.0
Aluminium	fcc	$\sim$400	660	142	4.4
Limestone			2570	210	2.1

Table 3.2: Power law-creep properties of aluminium [42, 43], Limestone [28], and the organic crystals Succinonitrile and Camphene [29, 24, 44]. T_{plast} is the plastic transition temperature, T_{melt} is the melting temperature, n is the stress exponent, and E_c the activation energy for lattice self-diffusion. For a discussion regarding the two latter properties, see section 2.1. Typical stress exponents for iron is 6.9, and 4.8 for copper [29].

Except at small loads, Camphene and SNC show power law creep with stress exponents, shown in Table 3.2, in the same range as aluminium and copper [29]. At the pressure and temperature we have conducted our experi-

ments, plastic crystals are believed to deform by dislocation creep according to Equation 2.1;

$$\dot{\epsilon}(T, \sigma) = Ae^{\frac{-E_c}{RT}}\sigma^n.$$

The arguments discussed above show that Camphene and SNC seem to fulfill all criteria for being metal analog materials. Both materials are transparent, allowing for more measuring techniques. Unfortunately SNC is toxic, so it needs to be handled with some more precautions than Camphene. Camphene evaporates at normal room conditions, while SNC does not, making study of the recrystallisation in extruded Camphene samples difficult. To cite the conclusion of Prakash and Jones [29]: "The close correspondence between the creep behaviour of organic plastic crystals and orthodox metallic systems, coupled with the experimental convenience and optical transparency of these compounds is very promising from a modelling point of view".

3.1.2 Preparation of analog materials

The extrusion press, shown in Figure 3.1, is built for extruding plastic crystals contained in disposable syringes. The 2 ml syringes are filled with melt drawn from a Succinonitrile or Camphene sample heated in a water bath. The sample contained in the syringe is then left for 24 hours at room temperature to slowly regain a solid state. As the sample solidifies during the first few hours, its volume is reduced and this enables air to enter and form a void in the tip of the syringe. During the next 20 hour period, fluids in the Camphene samples migrate to the tip of the syringe where the pressure is lowest. After the 24 hour period, the initial air-filled void in the Camphene sample is completely purged and replaced with the expelled fluid. There is no fluid present in the Succinonitrile samples; therefore, the void remains air-filled by the end of this period. The difference in fluid content in Camphene and Succinonitrile is probably caused by their purity, 95% and 99% respectively. All the samples are prepared from the same flasks of Camphene and Succinonitrille to promote repeatability in the experiments. The high fluid content in Camphene, however, has made it difficult for us to predict the outcome in the experiments with this material.

The next step in the process is to pressurise the syringe with a controlled force. This makes the sample recrystallise in a repeatable manner and pushes the fluid out of the syringes containing Camphene and the air out of the Succinonitrile samples. To do this, we place the syringe under pressure in a

cylinder with a piston pushed by a metal spring. It is left to anneal in this press for another 24 hours. When the syringe is removed from the press, the crystalline material appears transparent and fills the syringe completely. The analogue material is now ready to be extruded.

The next step is to cut the syringe to fit inside the extrusion press. We use a custom made cutting bench with a razor blade for this purpose. This is done to minimise the distortion of the crystal grains in the sample when cutting off the syringe tip and the plunger shaft. The syringe body containing the sample and piston is then ready to be inserted into the extrusion press.

Some ingots are specially treated to enable the measurement of the the bulk flow velocity within the bearing channel. The bulk flow field is determined with image correlation. This requires a layer of tracer-particles in a plane oriented perpendicular to the viewing direction, in the middle of the sample. To do this, the cylindrical plastic crystal sample is divided in the middle by pressing it out of the syringe and past a 0.1 mm thick piano string. Silicon carbamide particles less than 10 μm are then sparingly sprinkled onto the newly formed surfaces. Then the two halves are put together and inserted into the syringe. The sample is once again set under pressure to recrystallise before being inserted into the extrusion press.

The extrusion press with the ingot is held at constant temperature for at least 90 minutes prior to extrusion. We do this to assure that the plastic crystal is in thermal equilibrium with the temperature control system. For each material, all experiments were conducted at the same temperature. After many trial experiments we chose to extrude Camphene at $22°C$ and SNC at $40°C$. The temperatures are high enough that the normal stress, σ_n, acting on the bearing walls are comfortably below the yield stress of the glued die and sufficiently far from the melting point of the materials to prevent melt in the bearing channel.

3.2 Experimental means

The extrusion experiments are performed in a miniature extrusion press surrounded by further control and measurement systems. The entire setup is shown in figure 3.3. The deformation of the crystalline solids in the transparent die is recorded with a camera mounted on a microscope. A pressure transducer records the pressure of the hydraulic fluid during the extrusion.

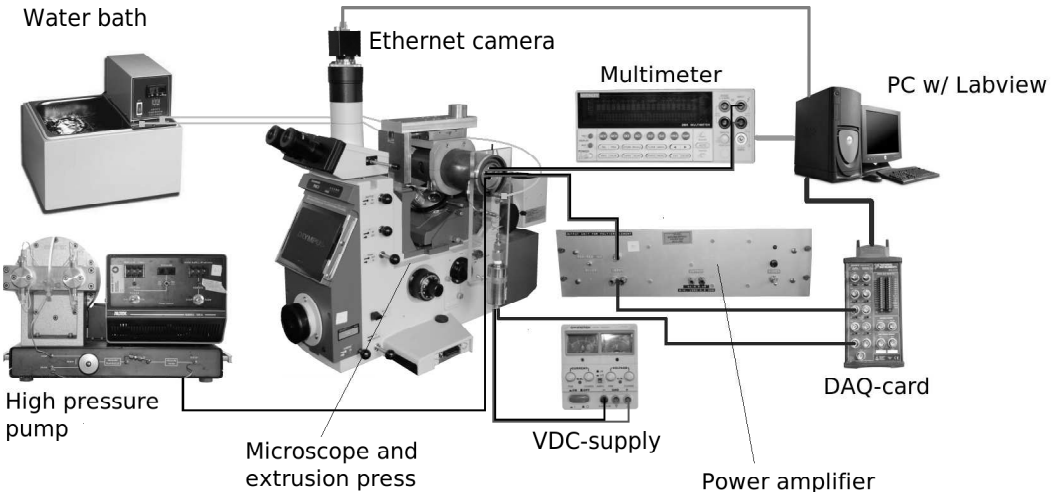

Figure 3.3: A schematic overview of the experimental setup we use to study the extrusion process. The extrusion press with the transparent die is mounted on the microscope. The material flowing inside the die is filmed with a Ethernet camera that is read with a desktop computer. The extrusion press is driven by a high pressure pump. The back pressure in the system is measured with a pressure transducer. A two stage temperature control system holds the extrusion ingot at a constant temperature during the extrusion.

The temperature of the ingot[4] containing the sample is controlled by a two stage thermal system. We use the commercial software Labview^{TM} to simultaneously record data from the camera and the pressure transducer and to control the temperature. The apparatuses briefly mentioned in this paragraph are thoroughly presented in the following sections.

3.2.1 Miniature Extrusion Press

The experiments are carried out with a custom built extrusion press inspired by the hot extrusion presses used in the aluminium extrusion industry. Our miniature press is shown in Figure 3.1. The press consists of a stainless steel body, an exchangeable die, a commercial plastic syringe with a piston, and a steel nut with a high pressure port. The polycrystalline sample is contained

[4]An ingot is a material cast into a shape suitable for further processing. It is also referred to as a billet, but preferably for larger sizes. Here it refers to the analog material contained in a syringe inside the press prior to extrusion.

in the plastic syringe; this allows us to handle even poisonous model materials since the material is enclosed prior to the experiment. The piston in the syringe separates the isopropanol, acting as hydraulic fluid, from the sample during extrusion. The die is held in place by four screws and a metal end piece. Between the metal and the die there are Teflon seals. The inner diameter of the syringe is 8.5 mm and the travel length of the piston is 40 mm. The smallest opening in the die is 4x1 mm, yielding a reduction factor of 14.2.

A pump is coupled to the high pressure port on the press and pumps hydraulic fluid at a constant rate. The hydraulic pressure exerting constant force on the syringe piston is measured with an Omega pressure transducer. The calibration procedure and installation of the pressure sensor and a discussion concerning the stability of the pump rate and pressure is presented in section 3.2.3.

A Prosilica GC 650 Ethernet camera is mounted to the microscope to monitor the extruded material in the die. The details regarding the image acquisition is discussed in section 3.3.2.

3.2.2 Extrusion Die

As stated above, the aim of our experiments is to visually observe the behaviour of the extruded material in the die. Therefore, the die had to be made out of an optically transparent material. In the preliminary studies we chose to mill dies from Plexiglas blocks. This technique allowed us to make many dies since the machining is time efficient and rather straightforward. A major drawback is the poor quality of the milled die surfaces, both on the inside and the outside. The rough Plexiglas surface reduced the contrast in our movies and pinned the slip line to large asperities on the bearing surfaces. To solve these problems, we have built a press for casting Plexiglas dies from smooth Plexiglas pieces. We use parts from a Plexiglas tube and a plate, and sinter them together at approximately $130°C$ (see Figure 3.4 for illustration). This enables us to control the radius of curvature R_{C} of the bearing surfaces. The sintered dies vastly improved the contrast in the movies and allowed the slip-line to move more freely compared to the milled dies.

Unfortunately, only the Plexiglas tubing we used for our $R_{\mathrm{C}} = 44.5mm$ dies was suited for the sintering process. As we varied the curvature of the dies by using different Plexiglas tubing, it became evident that most Plexiglas alloys in our inventory were unsuited for sintering. They either deformed drastically in the press as they approached the required sintering

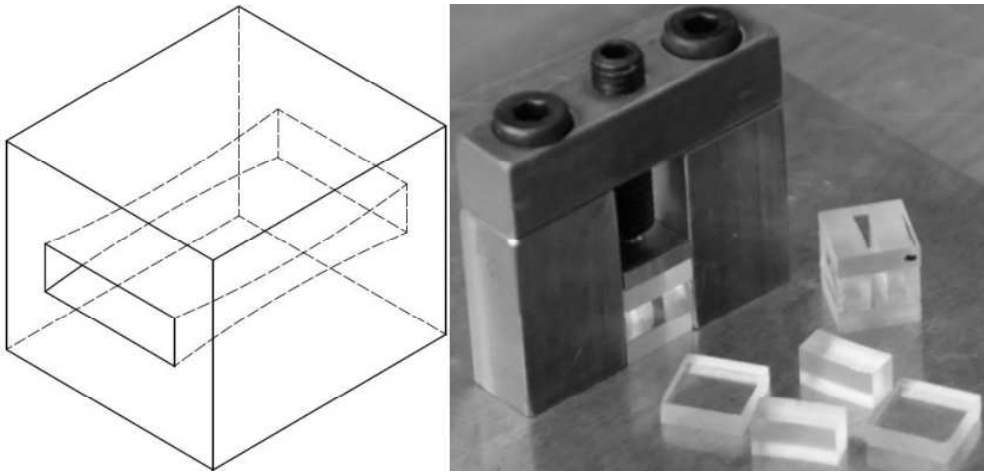

Figure 3.4: **Left:** A schematic view of our curved Plexiglas dies. In this report, the two curved surfaces are referred to as 'the die land surfaces' or 'the bearing surface'. **Right:** Our custom made die-press loaded with Plexiglas pieces ready to be glued together. In the foreground is the pieces we use; two end-plates and the side walls cut from Plexiglas tubing. Finally, to the right is a finished sintered die. Note how the die walls are bulging out as a result of plastic deformation during sintering. This was one of the reasons to begin gluing the dies together instead

temperature, or they became opaque after the heat treatment. We resolved this by changing our casting technique rather than searching for suppliers of the initial tubing. The dies used to obtain the measurements discussed in this report were all made by gluing the Plexiglas pieces together. We used the high strength Plexiglas glue ACRIFIX® 106 for this job. The glued dies withstood extrusion runs where the back-pressure in the press exceeded 100 bar. With tis metod, we also have greater control over the die geometry as no creep deformation occurred during the assembly. However, the drawback with this technique was the time consuming assembly process and the occurrence of glue being squeezed into the die channel. It is very difficult to assemble a die without any glue leaking out into the die channel. Because of this, we had to tolerate several dies with a small amount of solidified glue inside. To ensure the repeatability of the experiments in these cases, we did measurements on the opposite walls that had no visible glue-defects. Table 4.2 presents the measured dimensions of the dies, while the nominal dimensions of the dies are shown in Figure 3.5.

The geometry of the die prescribes where the extruded materials detaches (or slips) from the die. With parallel bearing surfaces the material, will slip

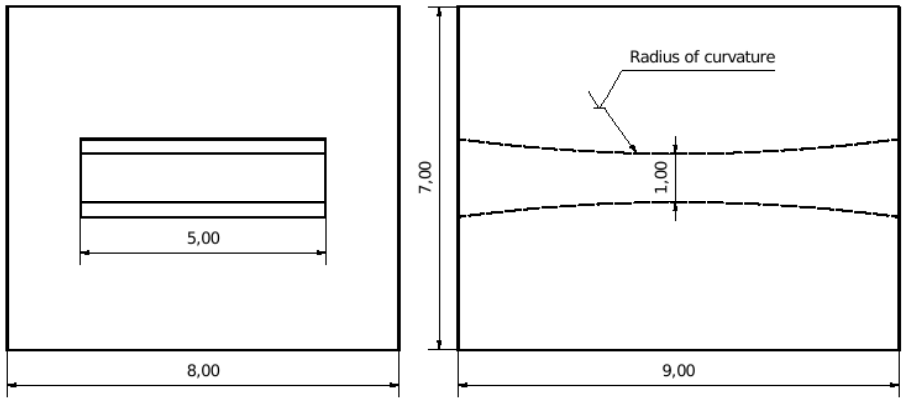

Figure 3.5: Schematic drawings displaying the nominal dimensions, in mm, of the glued dies. The nominal die dimensions used in the extrusion experiments are all the same, except for the radius of curvature R_c. However, their real dimensions vary slightly. These discrepancies are presented in Table 4.2.

at the die exit. A curvature in the die will make the slip occur in the vicinity of where the constriction is tightest, and it can be observed as a line, ie. the slip-line.

This section explains our choice of the radius of curvature of the bearing surfaces. When the plastic crystalline material has passed the middle of the die, where the constriction is tightest, it will expand elastically before taking on its final shape. To guarantee that the slip-line is in the die, rather than at the die exit, the expansion in the die must be greater than the elastic expansion of the extruded crystal. The slip line has a more static behaviour when the radius of curvature decreases. We therefore want a die curvature that just allows slip to occur, but restricts the movement of the slip line as little as possible. We have found the elastic expansion of the plastic crystals to be in the order of 0-2%. This was determined by comparing the dimensions of the narrowest point in the die to the thickness of the extruded profile.

The relation between the radius of curvature R_c and the expansion δ of the die is given by

$$\delta = 2(R_c - \sqrt{R_c^2 - d^2}), \qquad for\ R_c > d \tag{3.1}$$
$$R_c = \frac{\delta^2 + 4d^2}{4\delta},$$

where d is the half the length of the die, ie. 4 mm. The die curvature that gives an expansion of 3% between the middle of the die and the outlet is,

according to Equation 3.2, $R_c = 533mm$. The percentage is calculated for a nominal height of 1 mm in the middle and narrowest part of the bearing channel. Figure 3.6 shows the expansion for the die curvatures we have used. These curvatures clearly facilitate observation of the slip-line immediately down-stream from the middle of the bearing channel.

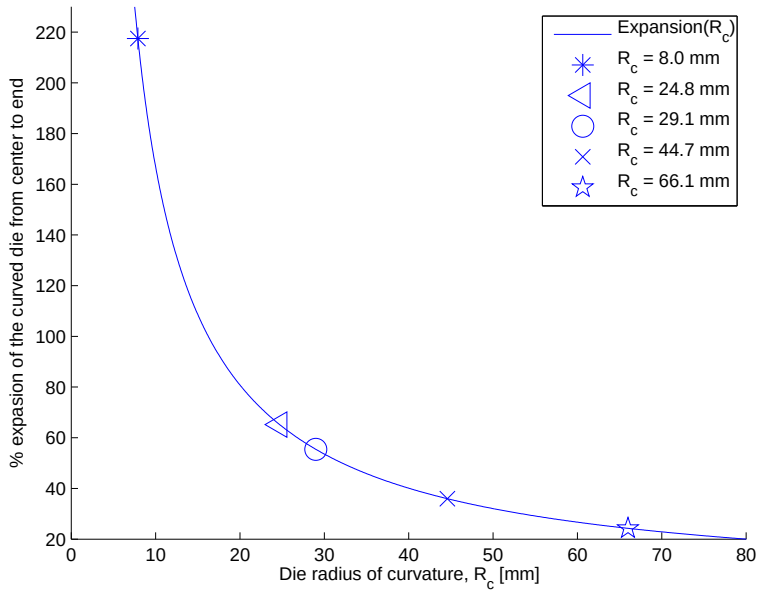

Figure 3.6: The expansion of the die between its narrowest point and the outlet (or inlet) as a function of the surface curvature. The narrowest point is the middle of the bearing channel, where the bearing surfaces are separated by 1 mm (the side walls are parallel and always separated by 4 mm). The five different curvatures we have used correspond to an expansion of 217%, 36%, 55%, 65%, and 24%.

3.2.3 Pressure Transducer and Pump Stability

Installation and calibration of pressure transducer
We use an Omega PX01C1-1.5KGI (0-103 bar full scale) gauge pressure transducer to record the back pressure exerted by the hydraulic fluid on the piston during extrusion. The friction between the syringe wall and piston are negligible compared to the back pressure provided by the pump, which for the various experiments lay in the 45-60 bar range. Therefore, the pressure acting on the ingot can be approximated to equal the back pressure. The current passing through the transducer has a linear relationship with the pressure it is sensing. At 1 atmosphere pressure (0 bar overpressure) the current passing through the transducer is 4.03 mA and at 103 bar the current is 20.02 mA. The current-pressure calibration points supplied by the manufacturer and the their linear fit is presented in Figure 3.7(b).

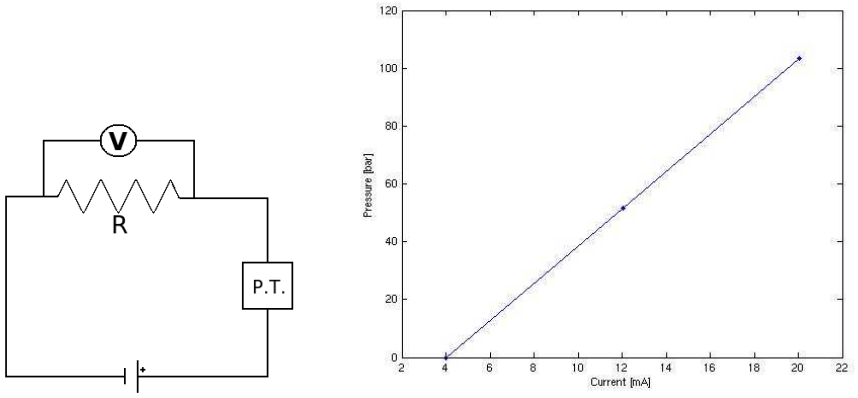

(a) (b)

Figure 3.7: (a) Scematic of the circuit used to measure the current through the pressure transducer (P.T.). We use a DAQ-card as a voltmeter. This card has a 16-bit DA-converter allowing the voltage readings to be read by the Labview software. The voltage is converted to pressure by Equation 3.2 determined from the calibration chart for the Omega PX01C1 pressure transducer shown in (b). There are five overlapping points that we use to determine the linear relationship between the current passing through the transducer and the pressure it is sensing.

The pressure transducer is exited with a 28 Vdc electrical potential from a Gwinstek DC power supply. To determine the current I (thereby the hy-

draulic fluid pressure) passing through the transducer, we have coupled it in series with a $R = 200\Omega$ resistor. The circuit is shown in Figure 3.7(a). We measure the electrical potential U over the resistance with a National Instrument 16-bit 6646 DAQ-card (digital acquisition) connected to a computer. The electric potential is then converted to current through Ohms law, $I = R/U$. Finally, we use Labview to convert the measured current into pressure in bar through the calibration formula

$$P_{bar} = \frac{1.0[bar]}{14.50326[PSI]} \left(93.51 \frac{U[mV]}{200[\Omega]} - 374.23 \right) [PSI] \tag{3.2}$$

which is determined from the calibration chart provided by Omega Engineering. The uncertainty of the pressure transducer is $\pm 0.05\%$ of full scale, which is 103 bar. This yields an absolute uncertainty of the transducer of ± 0.05 bar.

High pressure pump characteristics

To understand how the nominally constant flow-rate pump can affect our results we have tested it in an isolated system. The fluctuations in the back pressure recorded during the experiments are likely to originate from several sources. Examples of these effects are the decreasing resistance in the system as the syringe empties and heats, the very dynamic extrusion processes that we want to study, and fluctuations in the pressure delivered by the pump. To determine the importance of latter effect, without interference from anything else, we have tested how the pump performs when pressing against a constant resistance. The pump behaviour is characterised by studying how the flow-rate and pressure varies in this constant load system.

An end plug attached to the exit tube of the pump serves as a constant resistance. The resistance can be adjusted by tightening or loosening the nut to obtain the appropriate pressure for different flow-rates. The flow-rate is measured by weighing the hydraulic fluid (distilled water) that exits the tube. For this purpose, we use a Mettler PM4800 Delta Range® 0.01 gram accuracy scale with a RS323 interface. The pressure transducer and the scale is read simultaneously every 140 ms, 7 times per second. The measurements are logged in Labview together with the time for the measurements. Figure 3.8(a) illustrates how the flow-rate varies as the pressure builds up and is relieved. In the magnified region in Figure 3.8(a) the pump delivers a steady flow-rate of 0.52 ml/minute (the adjustment on the pump says 0.62 ml/minute). The pressure here varies with ± 0.5 bar around the mean pressure of 57.7 bar.

Figure 3.8(b) shows the pressure fluctuations for a different test with flow rate 0.03 ml/minute. The maximum pressure here is 81.7 bar, the minimum is 81.3 bar, and the mean pressure is 81.6 bar. This suggests that the pressure fluctuations decrease with a lower flow-rate. The pressure graphs also show a periodic drop in pressure in the steady flow regimes. This is probably caused by the pumps' software in order to maintain a constant flow-rate. With our current setup, we cannot measure what the actual flow-rate is during the extrusion experiment. The pump is set to give 0.2 ml/minute during the extrusion. However, the experiment described above shows that these settings are not accurate. The pump can be trusted to give a steady and repeatable flow-rate, but the flux value indicated on the pump is not accurate.

3.2.4 Two stage thermal control system

It is important to control the temperature of the ingot prior to and during the pressing. The recrystallisation rate and the viscosity of organic crystals are highly temperature dependent as shown in Equation 2.1. The initial temperature has to be thoroughly controlled to ensure reproducibility of the experiments.

We have set up a two-stage temperature control system that controls the temperature of the press to any set temperature in the range 15 to 80°C. The system is shown in Figure 3.1. The outer and first stage controller consists of a brass cylinder wrapped in a copper tubing coil surrounded by insulating Bakelite. This external system, or oven, alone controls the RMS temperature fluctuations in the extrusion press to ± 0.05°C. Inside the brass cylinder, and in good thermal contact, is a movable brass sledge with a block of aluminium holding the press around the shank. Inside the block is a Peltier element that is modulated by a thermistor sitting on top of it. The aluminium provides rapid thermal equalisation between the Peltier element and the ingot. When both the external water control and the Peltier element control are used, the temperature fluctuations around the die are ± 0.003°C. The oven has an opening, the large window on top shown in Figure 3.1, enabling the use of microscope objectives to study the die during experiments with reflected light microscopy. There are also two smaller holes in the oven (dashed circle around the die in figure Figure 3.1) for transmitted light birefringence experiments or for simultaneous use of an infrared and optical camera. The sledge is moved with a micrometre screw for positioning the viewing area during the experiment.

3.2.5 Thermistor Calibration

In order to monitor and control the temperature accurately in our experiments, we calibrated several negative temperature coefficient (NTC) $10k\Omega$ thermistors. The resistance measured over NTC thermistors decreases as the temperature increases. This temperature dependence is different for all thermistors, so each must be calibrated individually.

To determine how the resistance of each thermistor depends on temperature we submerged them together with a quartz thermometer in a water bath. The absolute accuracy of the quartz thermometer is $\pm 0.040°C$. A slow increase in temperature is required to achieve thermal equilibrium between the thermistors and the thermometer. The temperature of the thermistors and the thermometer was increased slowly by raising the water temperature in the bath from 10°C to 80°C over 12 hours. Equilibrium was further ensured by placing all the probes close together inside a block of copper.

Throughout the temperature ramp, we simultaneously measured the resistance over each thermistor and the temperature of the reference thermometer. We fit the recorded data set with the resistance of each thermistor as a function of temperature to the Steinhart-Hart equation

$$T = \frac{1}{c_1 + c_2 \log(\Omega) + c_3 \log^3(\Omega)}, \tag{3.3}$$

where T is the temperature of the thermistor (measured with the quartz thermometer) and Ω is the resistance over the thermistor at temperature T. The three Steinhart-Hart coefficients c_1, c_2 and c_3 can be determined using a linear regression since T and Ω are both known. The scripts we have written for the linear regression can be found in appendix B.2. Figure 3.9 shows the agreement between the measurements and the temperature curve fit by our calculated coefficients. We define the error in the Steinhart-Hart fitting d_{fit} as the residual of the temperature measured with the quartz thermometer, T_{quartz}, and the calculated thermistor temperature, T_{therm},

$$d_{fit} = T_{\text{therm}} - T_{\text{quartz}}.$$

When we insert the residuals for the fitting in the range $18 - 50°C$ into Equation 2.3

The mean standard deviation σ_m of the residuals in the range $18 - 50°C$, calculated according to Equation 2.3, is $\sigma_m = \pm 0.0034°C$. This is within the absolute uncertainty of the quartz thermometer.

3.3 Instrumentation

The high level programming language Labview® [45] was used to simultaneously control the temperature and to record pressure, images and temperature. The temperature is read through a Keithly 2000 multimeter with GPIB interface to an computer running Labview. This computer is used solely for controlling the PID loop modulating the Peltier element temperature. A second computer reads the camera through an Ethernet interface while simultaneously logging the back pressure driving the extrusion process. We divide the tasks between two computers because the image acquisition routine and the PID-loop both demand much of the computers RAM. This approach ensures that enough of the computers' memory is available for the camera to maintain a constant image acquisition rate. The graphical program code for the main data acquisition routine together with subroutines can be found in B.1. The calibration procedure of the thermistors and the pressure transducer are described in section 3.2.5 and section 3.2.3 respectively.

3.3.1 Experiment execution

This section gives an overview of how an experiment is executed. First the die, the cut syringe containing the sample, the extrusion press body, and the rear locking nut are assembled. The press is then fixed to the temperature controlled brass sledge, and inserted into the thermal oven situated above the microscope. The high pressure pump, that has run for a while to push any air out of the tubing, is attached to the rear of the press via the port in the lock nut. Before this connection is tightened, the pump is allowed to run for some time to expel the air in the press body. When the nut is tightened the same procedure is used for connecting the pressure transducer. Then the pump is turned off, and the temperature controlling system turned on. The system is then left for at least 90 minutes at the desired set temperature to ensure homogeneous temperature in the whole press.

The next step is to turn on the pump, while monitoring the back pressure. Since the hydraulic fluid flow rates we use are small, it takes about 2 minutes to compress the air trapped in the tubing between the press and pump and achieve working pressure. During the pressure buildup, the centre of the die is positioned over the microscope by adjusting the micrometre screws. When the pressure stabilises, and the material starts to flow through the die, we start capturing images and record the back pressure. The thermal control

loop is running simultaneously, and the temperature of the Peltier element is logged. All the measurements are recorded together with a time-stamp. The experiment is terminated when the syringe is empty. This can take up to 15 minutes depending on the flow rate. We investigate the extruded profile in a microscope to establish possible lineation or any other defects and we measure the profile dimensions with a calliper. When all the measurements have been logged, the press is taken apart and the various parts cleaned. The reusable die is carefully rinsed with hot water to prevent any damage.

3.3.2 Imaging

A Prosilica GC 650 Gigabit Ethernet CCD camera is mounted to the microscope to monitor the extruded material in the die. The camera has a CCD chip resolution of 492x648 pixels, and is capable of capturing up to 90 gray-scale frames per second. We use the scale bar insert on the microscope to determine the pixel to millimetre conversion for the captured images. We have performed experiments with two different magnifications, 5x and 2.5x. At these magnifications the dimensions of one pixel are $(1.56)^2$ μm^2 and $(3.13)^2$ μm^2 respectively. The camera is read to the Labview acquisition software through the computer's Ethernet interface. We use an Intel® PRO/1000 GT Desktop Adapter Ethernet network card, which supports Jumbo frames[5] as the camera manufacturer recommends [46].

It is critical to know the precise timing of the measurements made during the experiment. Knowing this, we can later correlate the pressure and extract the surface and the bulk velocity from the extrusion images. We have used a function in Labview that gives every measurement a universal time-stamp. Each image and pressure reading is written to the hard disk together with this millisecond time. In our preliminary experiments, output from Labview indicated that the Prosilica camera failed at acquiring images at a constant frame rate. The typical time between two image acquisitions was in the range 25-45 ms (20-40 frames per second). Therefore, we attempted to use the temporal heterogeneous timestamps to determine flow velocity and area fluctuations. We controlled the correctness of this approach by manually analysing movies of a spin-disk that rotates with constant angular velocity. This technique provides the best measure of the cameras acquisition rate possible. As suspected, we revealed a discrepancy between the time written to disk with each image, t_{PC}, and the time measured from the spin-plate,

[5] A jumbo frame is loosely defined as a frame size greater than 1500 bytes. However, the typical Jumbo frames are around 9000 bytes [46].

t_{SP}. We estimated this error, e, according to

$$e = \Delta t_{PC} - \Delta t_{SP},$$

where Δt_{PC} and Δt_{SP} are the time separating two images obtained from the time stamp function and the spin-plate measure respectively. We have estimated the root-mean-square error, e_{rms}, to be

$$e_{rms} = \sqrt{\frac{1}{n}\sum e^2} = 12.73ms,$$

where the number of measurements,n , are $n = 26$. We have used the results from these experiments only to measure quantities on longer timescales, and therefore are independent of errors in the order of $\pm 100ms$.

The error occurred because the image acquisition routine in Labview had insufficient memory to work properly and the camera was set to acquire as many images as possible rather than at a fixed frame rate. We solved the timing problem by using a second desktop computer for the memory demanding temperature control routine and by fixing the frame rate to 35 fps. The current setup has been tested with the spin-disk to assure that the correct time is written with the measurements. The time between each image acquisition in the analysed extrusion experiments with correct timing are $\Delta t = 28.64 \pm 0.02ms$, which corresponds to 34.9 fps. This estimate is calculated according to Equation 2.3 based on a series of 1000 images.

The uncertainty in Δt for the various experiments we have analysed is listed in the overview of the analysed experiments in Table 4.1.

3.4 Image analysis

The main objectives of the image analysis tools we have implemented are to determine the flow profile and detect the position of the slip-line in the die. These methods have to be automated in order to process the several thousand images we acquire for each experiment.

An example of three successive reflected light microscope images that are used to determine the slip-line position and surface velocity of the extruded are shown in Figure 3.10. The focus in the images is on the surface of the curved bearing wall in the die. The inlet side, the upper part, in these images is dark because not much light is reflected from the interface in focus. On

the outlet side, the lower part, however, there is more light reflected from the interface. We interpret the dark region as the interface between the extruded material and the bearing surface. The material-Plexiglas interface does not reflect much light. This is because of the similar refractive index of the analog material and the Plexiglas[6]. In the bright region, the focus is on the interface between the extruded profile and air[7]. The border between the two regions of different contrasts are identified as the slip-line.

We attempted to extract the temporal evolution of the slip-line, using two different active contour methods. The first one is often referred to as a "snake", which is based on using image gradients to detect edges[8]. The second is based on an image segmentation method without the use of edge detection. We ended up using the latter, because it provided, by far, the best results using our images. Both detection methods are presented in the following sections with emphasis on our preferred method.

The flow profile, or velocity, of the extrusion flow in the die is determined by correlating material points with different contrast from one image to the next. For the surface velocity measurement of the material, it is the crystal grain boundaries that make up structured contrasts we can correlate. In the images used to determine the bulk flow measurement, however, there are no visible grain boundaries or other structures to correlate. To make this measurement possible, we must disperse tracer particles in a plane inside the ingot. The thorough explanation of the work done to determine the flow properties is presented in section 3.4.3.

[6]The refractive indexes of Succinonitrile liquid and Plexiglas are n=1.49 and n=1.41 respectively. The refractive index of Camphene is unknown to us, but is believed to be lower than in Succinonitrile since the Camphene-Plexiglas interface appears brighter than the Succinonitrile-Plexiglas interface.

[7]In air, the refractive index $n \approx 1$

[8]Edges refers to large contrasts in image intensities, which defines different objects in the image. In our case , the dark stick and bright slip regions.

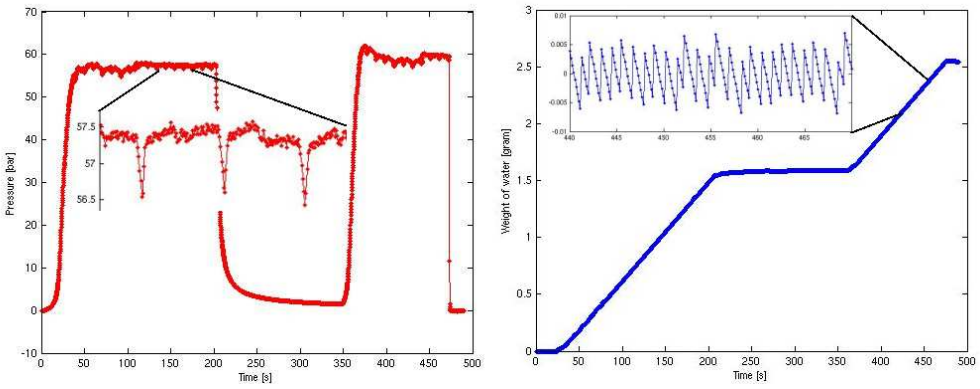

(a)

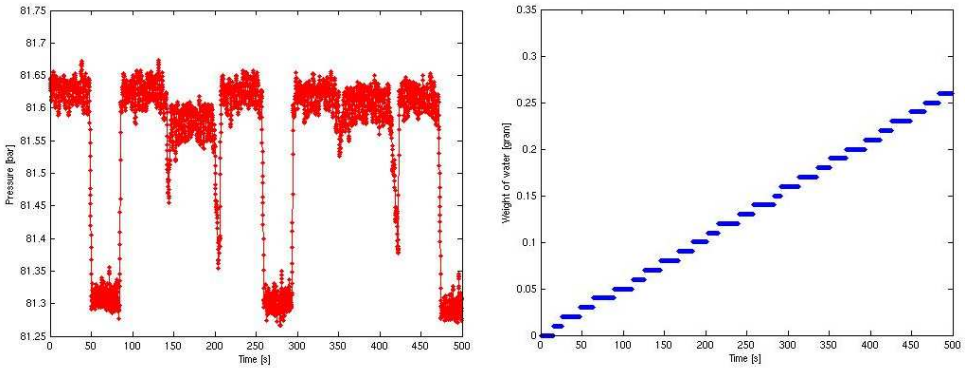

(b)

Figure 3.8: (a) Pressure (red line) and flow-rate (blue line) recorded to test the pump stability. The red line shows how the pressure builds up as the pump works against a constant resistance and fluctuates around a constant level. The first drop in pressure (and halt in flow) is caused by turning off the pump. The last and more sudden drop occurs when the drain valve on the pump is opened. The fluctuations in pressure in the steady flow region are magnified. Here, the periodic drop in pressure (every 10 seconds) indicates when the pump is slowing to maintain a constant flow-rate. The slope of the blue line is the flow-rate, which is constant when the work pressure is reached. The slopes correspond to a flow-rate of 0.52 ml/minute. The magnification shows the fluctuations in the flow-rate that are caused by the resolution of the weight, 0.01 gram. (b) Pressure fluctuations measured in the steady flow regime over a period of 8 minutes. The flow rate is considerably lower than in (a), only 0.03 ml/minute. We can see that the pressure fluctuations introduced by the pump are smaller when the flow-rate is decreased. At this flow-rate, the periodic pressure drops caused by the internal pump software are more pronounced; each drop is held for approximately 30 seconds.

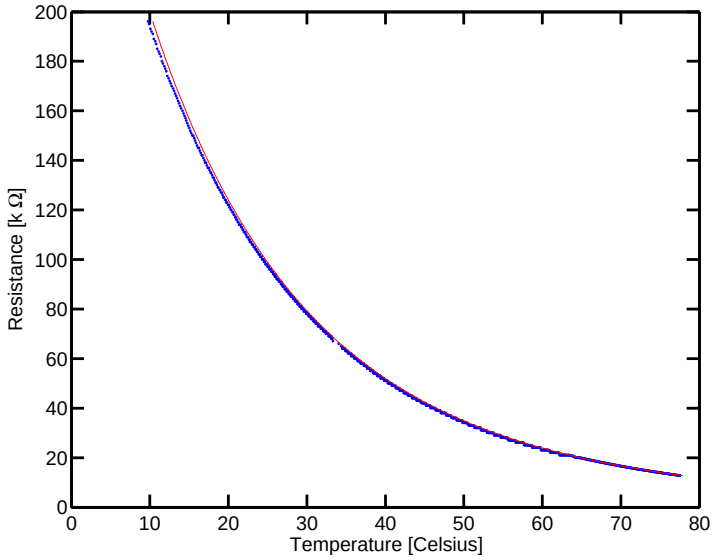

Figure 3.9: The blue data points represent the resistance over a 10kΩ thermistor in the range 10 to 80°C. The red line is the temperature from the Steinhart-Hart equation,3.3, when inserting the measured resistance and the coefficients obtained by linear regression. The coefficients for this particular thermistor are $c_1 = 1.0e-3$, $c_2 = 2.4993e-04$ and $c_3 = 1.3125e-07$.

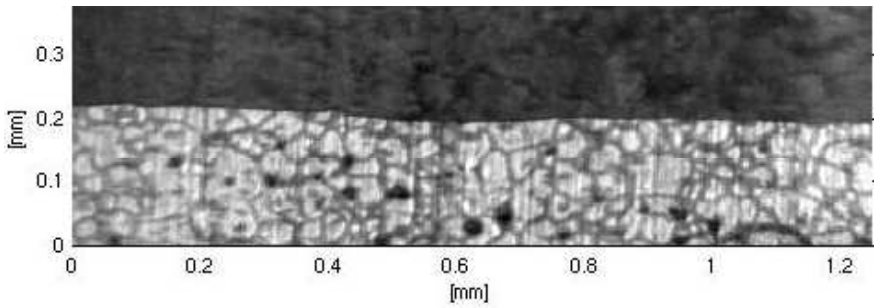

(a) t_1

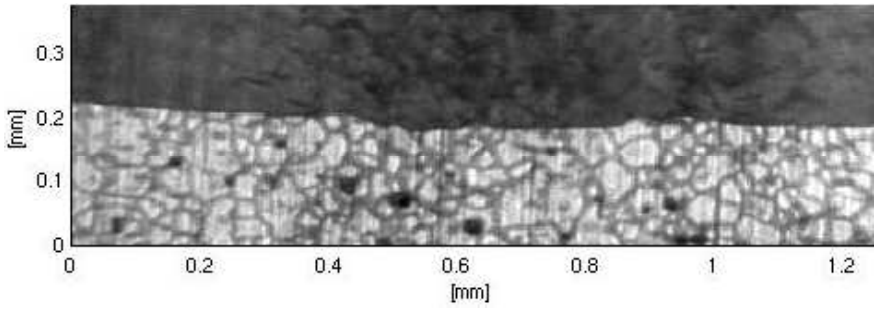

(b) t_2

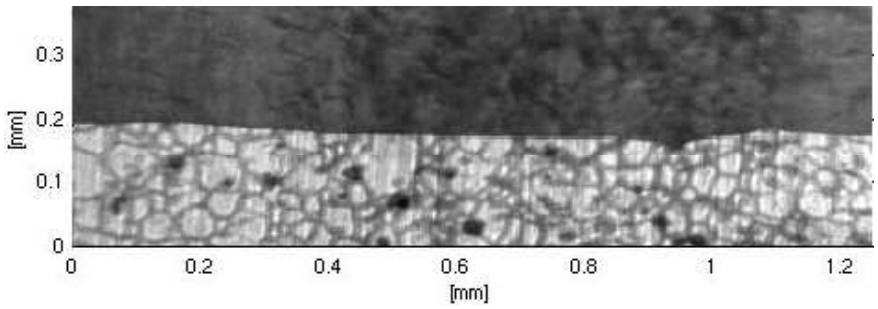

(c) t_3

Figure 3.10: Three succeeding reflected light microscope images of of Camphene in a Plexiglas die during extrusion. The flow is from top to bottom. During one experiment we acquire up to several thousand frames. The analysis of all these frames requires automatic contour detection and velocity algorithms. In the dark area in the images, the crystalline material sticks to the die surface. This region is referred to as the "stick domain". In the bright region, the material is unattached to the die and is the "slip region". The boundary separating the two regions is the slip-line whose coordinates we extract. The polygonal pattern visible as dark lines in the slip region is grain boundaries used to determine the exit velocity of the extruded material. Note the dark spots in the slip region. These are material deposits adhering to the bearing surface that some times are moved slowly down stream by the extrusion flow. Having objects moving with different speeds complicates the velocity measurement, but increasing the correlating regions allows this problem to be overcome.

3.4.1 Edge detection using intensity gradients

We tried to use an energy minimising contour, henceforth called snake, to segment the pictures acquired in the experiments into regions controlled by either by stick or slip. The energy of the snake depends on its shape and position within the image. From an initially prescribed position, the snake is allowed to dynamically move within the image towards an equilibrium between the forces acting upon it. These forces can be divided into internal forces and image forces. In our method, the internal forces are comprised of tension forces and rigidity forces. The tension force will make the snake act like a membrane by controlling the length of the snake, while the rigidity force makes it resist bending. The image forces are represented by a potential function P(x,y) whose minima coincide with the intensity extrema in the image I(x,y) (in our case the ductile-brittle transition). The snake is represented by the parametrisation

$$\vec{v}(s) = (x(s), y(s)).$$

The vector $\vec{v}(s)$ describes the position of the entire snake as s varies from its minimum value (start of snake) to its maximum value (end of snake). The energy functional to minimise the shape of the snake is

$$E_{snake}(\vec{v}) = E_{internal}(\vec{v}) + E_{image}(\vec{v}),$$

where $E_{internal}$ and E_{image} represent the energy exerted on the snake by internal and image forces respectively. The internal energy is calculated from the tension and rigidity forces,

$$E_{internal}(\vec{v}) = \frac{1}{2}\int_s w_1 \left|\frac{\partial \vec{v}}{\partial s}\right|^2 + w_2 \left|\frac{\partial^2 \vec{v}}{\partial^2 s}\right|^2 \, ds,$$

the first term controls tension (length) of the line and the latter controls the rigidity (smoothness) of the snake. When the distance between two positions on the curve grows, the tension term increases. The rigidity term increases when changes in the snake make sharp turns. The parameters w_1 and w_2 determines which behaviour is the most important. The image energy is the sum of the potential function P ($P(x, y) = -I(x, y)$) along the snake. The exact expression is

$$E_{image}(\vec{v}) = \int_s P(\vec{v}) \, ds.$$

When the energy $E_{snake}(\vec{v})$ has its minimum, the snake is in the optimal

position. To summarise, we have

$$E_{image}(\vec{v}) = \int_s \frac{1}{2} w_1 \left| \frac{\partial \vec{v}}{\partial s} \right|^2 + \frac{1}{2} w_2 \left| \frac{\partial^2 \vec{v}}{\partial^2 s} \right|^2 + P(\vec{v})\ ds.$$

We now name the integrand in the above equation for F:

$$F(\vec{v}, \dot{\vec{v}}, \ddot{\vec{v}}) = \frac{1}{2} w_1 \left| \frac{\partial \vec{v}}{\partial s} \right|^2 + \frac{1}{2} w_2 \left| \frac{\partial^2 \vec{v}}{\partial^2 s} \right|^2 + P(\vec{v}).$$

It can be shown by using calculus of variations that the $\vec{v}$ that minimises the $E_{image}(\vec{v})$ satisfies the differential Euler-Lagrange equation

$$\frac{\partial F}{\partial \vec{v}} - \frac{d}{ds}\left(\frac{\partial F}{\partial \dot{\vec{v}}}\right) + \frac{d^2}{ds^2}\left(\frac{\partial F}{\partial \ddot{\vec{v}}}\right) = 0. \quad where\ \dot{\vec{v}} \tag{3.4}$$

The details of the Euler-Lagrange transformation is omitted in this section. The transformation is described in depth in the following section along with our preferred image analysis technique. When we carry out the differentiation in Equation 3.4, we obtain the equation describing the snake position when the internal forces are counterbalanced by the image forces

$$-w_1 \frac{\partial^2 \vec{v}}{\partial ds^2} + w_2 \frac{\partial^4 \vec{v}}{\partial ds^4} = -\nabla P(s).$$

This can be written in component form as

$$-w_1 \frac{\partial^2 x}{\partial ds^2} + w_2 \frac{\partial^4 x}{\partial ds^4} = -\frac{\partial P}{\partial x} \quad -w_1 \frac{\partial^2 y}{\partial ds^2} + w_2 \frac{\partial^4 y}{\partial ds^4} = -\frac{\partial P}{\partial y}.$$

We must solve the differential equations above iteratively to obtain the location of the snake that balances the internal and external forces (minimise E_{image}). The numerical recipe we have written for Matlab to do this is presented in Appendix C.1.

However, this method was unable to extract the slip-line because of the many local intensity gradients in the extrusion experiment images. Figure 3.11 illustrates how local gradient maximas arrest the snake before it is able to extract the globally largest gradient, the slip-line.

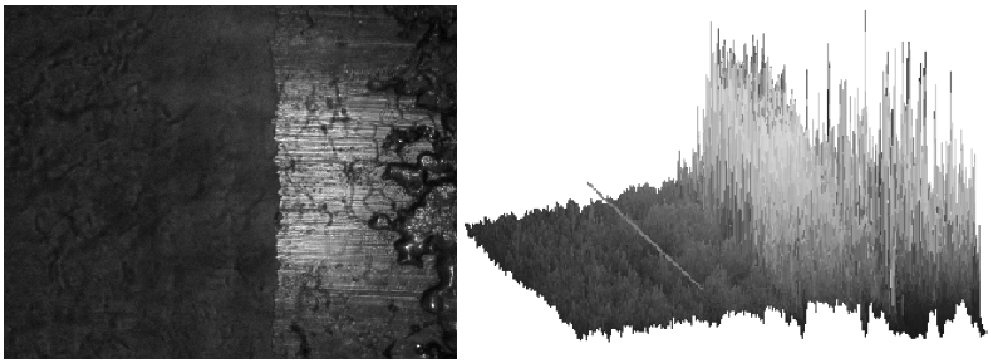

Figure 3.11: The left image is the original image $I(x, y)$ of the slip-line. The right image displays the derivative of the potential function $P(x, y) = -I(x, y)$. The line in the picture is an active contour (or snake) that has found a local potential minimum. The slip-line is easily identified by inspection in the original image. An automatic detection of the transition relying on intensity gradients is not possible because of the noise. Smoothing the image will help the snake localise the global minimum in $\nabla P(x, y)$, however, this will also lead to a blurring of the topology of the slip-line.

3.4.2 Edge detection not dependent on intensity gradients

The method described here, presented in [47], does not rely on intensity gradients to identify objects in an image. Therefore, objects without a sharp edge can also be detected. The method makes use of an evolving level set function whose zero-contour gives the borders of objects in the picture directly. This approach allows several objects to be detected simultaneously, including interior contours. Let us go through all of the derivation, starting with the basic idea and ending up with a numerical expression ready to be implemented in a script.

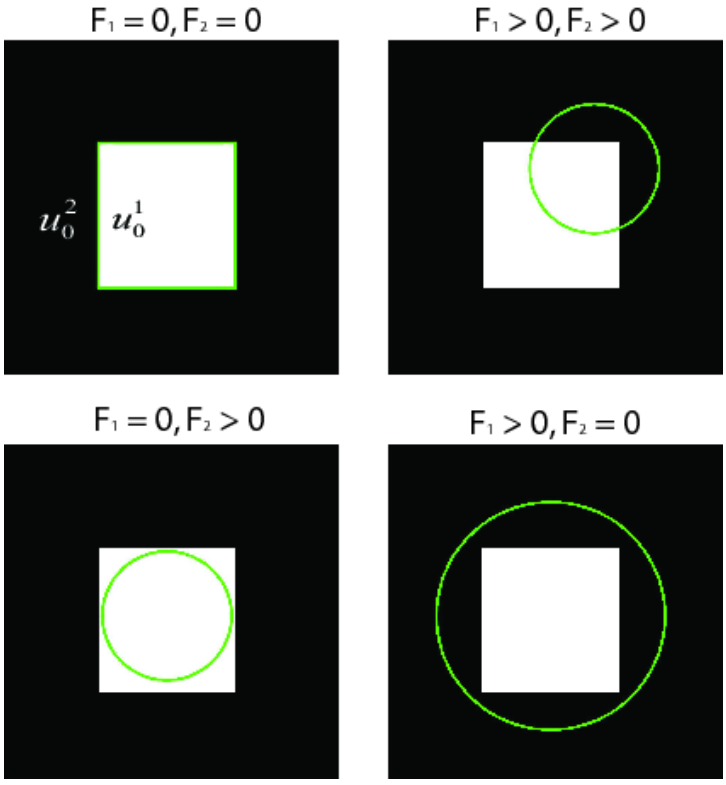

Figure 3.12: The fitting terms F_1 and F_2 are only minimised when the curve lies on the border between the two regions with intensities u_0^2 and u_0^2.

Consider a curve C defined on an image u_0. The region of the image inside C is denoted "inside(C)" and the remaining region outside C is "outside(C)".

The basic idea of this method is to minimise the fit terms

$$\begin{aligned} F_1(C) + F_2(C) = \quad & \int_{inside(C)} (u_0(x,y) - c_1)^2 \; dxdy \\ & + \int_{outside(C)} (u_0(x,y) - c_2)^2 \; dxdy, \end{aligned}$$

where c_1 and c_2 are the average of the image intensities inside and outside the contour respectively. An example with an ideal image will illustrate the basic concept. Let u_0 be an image comprised of two regions with piecewise constant intensities u_0^1 and u_0^2, and let the curve C_0 be the border between the two regions. This is illustrated in Figure 3.12. Then $C_1 = u_0^1$ and $C_2 = u_0^2$ when $C = C_0$;

$$F_1(C = C_0) + F_2(C = c_0) = 0.$$

A deviation of C away from C_0 increases the sum $F_1(C) + F_2(C)$.

In addition, to minimise the two image dependent terms F_1 and F_2, we also consider the length of the curve C and the area inside C. All this can be written as an energy functional $F(c_1, c_2, C)$ given by

$$\begin{aligned} F(c_1, c_2, C) = \quad & \nu \; Area(inside(C)) + \mu \; Length(C) \\ & + \lambda_1 \int_{inside(C)} (u_0(x,y) - c_1)^2 \; dxdy \\ & + \lambda_2 \int_{outside(C)} (u_0(x,y) - c_2)^2 \; dxdy, \end{aligned}$$

where ν,μ,λ_1 and λ_2 are fixed parameters determining the weighting of the different terms.

We can represent the evolving curve C with the zero contour of the level set function ϕ (thereby $F(c_1, c_2, C) \rightarrow F(c_1, c_2, \phi)$) defined such that

$$\phi = \begin{cases} \phi(x,y) = 0 & \text{on C} \\ \phi(x,y) > 0 & \text{inside C} \\ \phi(x,y) < 0 & \text{outside C} \end{cases}$$

We can now express the energy functional F using the Heaviside function and its derivative (the Dirac delta function)

$$H(z) = \begin{cases} 1, & \text{if } Z \geq 0 \\ 0, & \text{if } Z < 0 \end{cases}, \quad \delta_0(z) = \frac{d}{dz}(H(z)).$$

The terms in $F(c_1, c_2, \phi)$ become

$$Area(\phi \geq 0) = \int_{u_0} H(\phi(x,y)) \; dxdy,$$

$$Length(\phi = 0) = \int_{u_0} \nabla H(\phi(x,y)) \; dxdy = \int_{u_0} \delta_0(x,y) \nabla \phi(x,y) \; dxdy.$$

The two fitting terms can be written as

$$\int_{\phi>0}(u_0(x,y)-c_1)^2\ dxdy = \int_{u_0}(u_0(x,y)-c_1)^2 H(\phi(x,y))\ dxdy,$$
$$\int_{\phi<0}(u_0(x,y)-c_1)^2\ dxdy = \int_{u_0}(u_0(x,y)-c_1)^2 (1-H(\phi(x,y)))\ dxdy$$

Collecting the terms gives

$$\begin{aligned} F(c_1,c_2,C) = \quad & \nu\int_{u_0} H(\phi(x,y))\ dxdy \\ & +\mu\int_{u_0}\delta_0(x,y)\nabla\phi(x,y)\ dxdy \\ & +\lambda_1\int_{u_0}(u_0(x,y)-c_1)^2 H(\phi(x,y))\ dxdy \\ & +\lambda_2\int_{u_0}(u_0(x,y)-c_2)^2(1-H(\phi(x,y)))\ dxdy. \end{aligned}$$

By minimising $F(c_1,c_2,C)$ with respect to c_1 and c_2 for a fixed ϕ value, the average image intensities, c_1 and c_2, can be determined:

$$\frac{dF}{dc_1}=0 \quad = \int_{u_0}(-2u_0(x,y)+2c_1)H(\phi(x,y))\ dxdy \tag{3.5}$$

$$c_1 \quad = \frac{\int_{u_0} u_0(x,y)H(\phi(x,y))\ dxdy}{\int_{u_0} H(\phi(x,y))\ dxdy}, \tag{3.6}$$

and

$$\frac{dF}{dc_2}=0 \quad = \int_{u_0}(-2u_0(x,y)+2c_2)(1-H(\phi(x,y)))\ dxdy \tag{3.7}$$

$$c_2 \quad = \frac{\int_{u_0} u_0(x,y)(1-H(\phi(x,y)))\ dxdy}{\int_{u_0}(1-H(\phi(x,y)))\ dxdy}. \tag{3.8}$$

To find the minimizers of $F(c_1,c_2,\phi)$ we calculate the Euler-Lagrange equation for the level set function ϕ. Section 2.2 offers an introduction to Calculus of Variations and the nomenclature used in the following calculations. A regularisation of the Heaviside function $H(z)$ and the delta function δ_0 is required to find the stationary curve. Let $H\to H_h$ and $\delta_0\to\delta_h$.

$$H_h(z)=\frac{1}{2}\left(1+\frac{2}{\pi}\arctan(\frac{z}{h})\right), \quad \delta_h=\frac{1}{\pi h}\left(\frac{1}{1+\left(\frac{z}{h}\right)^2}\right) \tag{3.9}$$

The Heaviside function and the Dirac delta function are plotted along with our approximations in Figure 3.13. One can see from Equation 3.9 that as $h \to 0$ the regularised functions converge to H and δ.

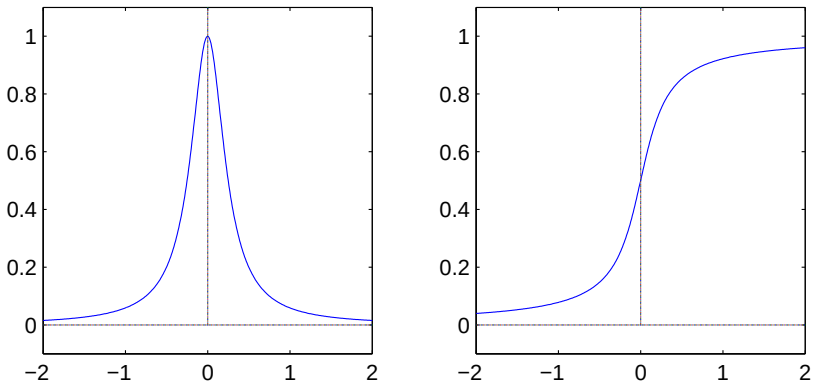

Figure 3.13: **Left**: Regularisation of the Heaviside function H_h.**Right**: Regularisation of the Dirac Delta function δ_h. Observe that because of the regularisation, δ_h is different from zero everywhere. This makes the method more likely to find global minimisers of F_h

Now we are ready to determine the associated Euler-Lagrange equation for $F(c_1, c_2, \phi)$. For simplicity we regard c_1 and c_2 as constants as we minimise F_h

$$\begin{aligned} F_h(c_1, c_2, \phi) = \quad & \nu \int_{u_0} H_h(\phi(x,y))\ dxdy \\ & +\mu \int_{u_0} \delta_h(x,y)\nabla\phi(x,y)\ dxdy \\ & +\lambda_1 \int_{u_0} (u_0(x,y) - c_1)^2 H_h(\phi(x,y))\ dxdy \\ & +\lambda_2 \int_{u_0} (u_0(x,y) - c_2)^2 (1 - H_h(\phi(x,y)))\ dxdy. \end{aligned}$$

The full Euler-Lagrange transformation is presented in A.1. Here we only quote the result of this transformation, the expression that minimises F_h

$$\begin{aligned} \frac{dF_h}{d\epsilon} = \quad & \delta_h(\phi)\Big(\nu - \mu\ div\frac{\nabla\phi}{|\nabla\phi|} \\ & +\lambda_1(u_0 - c_1)^2 - \lambda_2(u_0 - c_2)^2\Big) = 0. \end{aligned}$$

Now our job is to determine the level-set function ϕ_0 that satisfies this nonlinear equation. We can do this by introducing an artificial time t, and demanding that $F_h(\phi(t,x,y))$ decreases with time. Let the level set function ϕ^t be our initial guess for ϕ_0. The following procedure will, for each iteration, bring ϕ closer to ϕ_0 (that is $F_h(\phi^{t+1}) < F_h(\phi^t)$):

$$F_h(\phi^{t+1}) = F_h(\phi^t + (\phi^{t+1} - \phi^t)),$$

let $\Delta\phi_t = \phi^{t+1} - \phi^t$ be the change in ϕ between each step. We can now Taylor expand the expression

$$F_h(\phi^{t+1}) = F_h(\phi^t + \delta\phi_t) = F_h(\phi^t) + \frac{dF_h}{d\Delta\phi_t}\Delta\phi. \tag{3.10}$$

By demanding that $\Delta\phi_t = -c\frac{dF_h}{d\Delta\phi_t}$, we get

$$F(\phi^{t+1}) = F_h(\phi^t) - c\left(\frac{dF_h}{d\Delta\phi_t}\right)^2.$$

This expression converges to the minimum of F_h. The method we use here is analogous to the Euler-Lagrange transformations we applied to all the terms of F_h, and we can write $\Delta\phi_t$ as

$$\frac{dF_h}{d\Delta\phi_t} = \delta_h(\phi)\left(\nu - \mu\ div\frac{\nabla\phi}{|\nabla\phi|} + \lambda_1(u_0 - c_1)^2 - \lambda_2(u_0 - c_2)^2\right)$$

This is the change we apply to ϕ as we iterate towards the stationary solution

$$\frac{dF_h}{d\Delta\phi_t} = 0 \tag{3.11}$$

Numerical Approximation

Following the work in [47], we use a finite difference implicit scheme to discretise Equation 3.11. Let the space step be $\Delta\phi_t$, the time-step Δt, the spatial coordinates aka grid points $(x_i, y_i) = (ih, jh)$, and $\phi^n_{i,j} = \phi(n\Delta t, x_i, y_i)$. The finite differences are

$$\Delta^x_-\phi_{i,j} = \phi_{i,j} - \phi_{i-1,j}, \qquad \Delta^x_+\phi_{i,j} = \phi_{i+1,j} - \phi_{i-1,j}$$
$$\Delta^y_-\phi_{i,j} = \phi_{i,j} - \phi_{i,j-1}, \qquad \Delta^y_+\phi_{i,j} = \phi_{i,j+1} - \phi_{i,j}$$

Using the iterative algorithm from [48], ϕ^{n+1} is computed from the linearising

of Equation 3.11

$$\begin{aligned}\phi_{i,j}^{n+1} = \quad & \phi_{i,j}^{n} \\ & +\Delta t\delta_h(\phi_{i,j}^{n})\left[\frac{\mu}{\Delta\phi_t^2}\Delta_-^x\left(\frac{\Delta_+^x\phi_{i,j}^{n+1}}{\sqrt{(\Delta_+^x\phi_{i,j}^{n})^2/(\Delta\phi_t^2)+(\phi_{i,j+1}^{n}-\phi_{i,j-1}^{n})^2/(2\Delta\phi_t)^2}}\right)\right. \\ & +\frac{\mu}{\Delta\phi_t^2}\Delta_-^y\left(\frac{\Delta_+^y\phi_{i,j}^{n+1}}{\sqrt{(\Delta_+^y\phi_{i,j}^{n})^2/(\Delta\phi_t^2)+(\phi_{i+1,j}^{n}-\phi_{i-1,j}^{n})^2/(2\Delta\phi_t)^2}}\right) \\ & \left.-\nu-\lambda_1(u_{0_{i,j}}-c_1\phi^n)^2+\lambda_2(u_{0_{i,j}}-c_2\phi^n)^2\right].\end{aligned}$$

We have implemented the edge detection method described here in Matlab (the script can be found in Appendix C.2).

3.4.3 Velocity measurement

It is interesting to determine the correlation between the extrusion velocity and the slip-line movement. This section explains how we determined the extrusion velocity using image correlation. We tried two different methods, which both are described in this section. For the final velocity analysis, we ended up using the approach correlating pixels (presented second) and not the one correlating average intensities. The numerical implementation was done in MatLab

We measure the surface velocity of the material immediately next to the bearing surface by correlating images of the surface of the exiting profile captured with known time intervals. These measurements have to be taken down-stream from the slip-line, ie. where the material has detached from the die walls (slip regime). Up-stream from the slip-line the material adheres to the die surface, and the velocity of the material immediately next to the bearing surface is zero in this region. Note that the term "extrusion velocity" in the following refers to the surface velocity of the extruded material down-stream of the slip line. We have also determined the bulk velocity of the material as it flows through the die. This measurement is made based on the flow of particles dispersed inside the flowing material.

Extrusion velocity measurement obtained by cross correlating average image intensities

We average the intensities in two squares (10×10 pixels) separated by a constant distance Δs in the flow direction to determine the average flow velocity. Figure 3.14 illustrates this method, and is referred to throughout the following discussion. The script executing the method described here can be found in Appendix C.3.

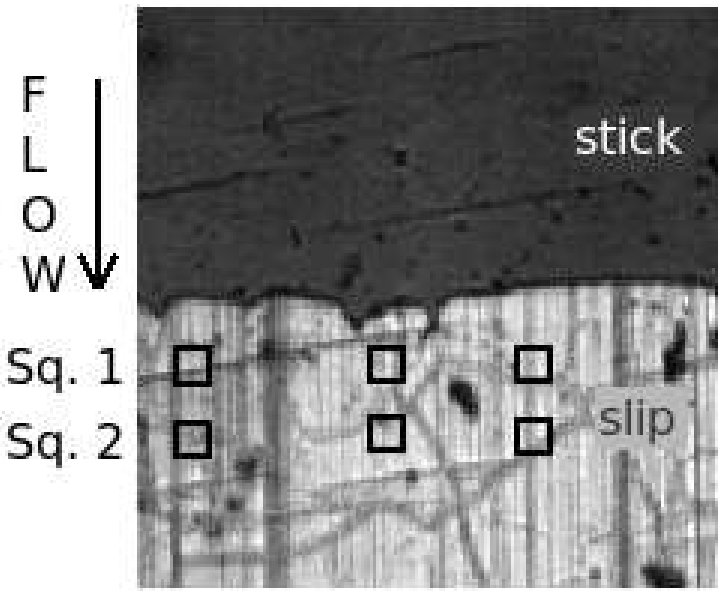

Figure 3.14: The mean intensities in the two squares separated by a distance Δs is recorded. By correlating the two recorded intensities, we determine the time Δt required for a point on the profile surface to travel Δs. Knowing Δs and Δt we can calculate the flow velocity of the extruded material.

Starting with the first movie frame to analyse, we record the intensities in the two squares (1 and 2) for as many movie frames as required to ensure that the same intensity spectrum has been visible in both squares. This gives us two intensity vectors I1 and I2. The next step is to normalise and remove the any trends from the intensity functions. The cross correlation function $R(n)$ can now be calculated by the formula

$$R(n) = \frac{1}{N} \sum_{i=1}^{N} I1_{i+n} I2_i, \tag{3.12}$$

where n is the number of frames offsetting the two correlation functions. The maximum of $R(n)$ gives the time expressed in number of frames, n, that a

point on the surface of the extruded profile spends on travelling from square 1 to square 2 (Δs).

Equation 3.12 gives the number of offsetting frames between I1 and I2 in whole numbers. To determine the extrusion velocity more precisely we need to determine the actual decimal number of offsetting frames. We do this by fitting a second-order polynomial around the maximum of $R(n)$. The maximum of the fitted function multiplied with the average time between two movie frames gives Δt. We follow the method for linear least square fitting described in [49]. The Matlab code for implementing the fitting procedure presented in Appendix B.2. The average flow velocity is found by

$$v_{\text{flow}} = \frac{\Delta s}{\Delta t}.$$

The method above is very sensitive to large perturbations of the flow, such as an impurity covering both of the squares. To limit this problem, we measure the flow velocity at three different places along the slip line. The velocity v_{flow} is set to be the average of the two velocities that differ the least. The above procedure is then repeated, starting at the second movie frame and continuing. The result is a vector $\bar{v}_{\text{flow}}(t)$ containing the average velocity of the extruded material.

Extrusion velocity measurement obtained by correlating pixels between two successive images

Correlating structures on the pixel level provides a better spatial and temporal resolution of the velocity field compared to the method described above.

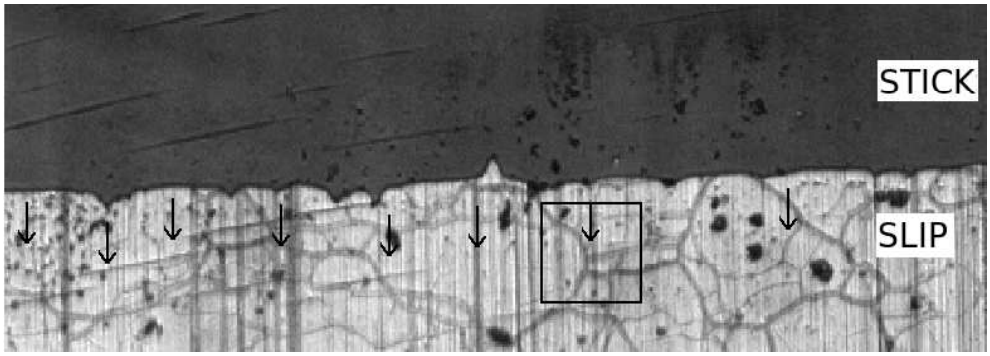

Figure 3.15: The arrows indicates how the flow velocity is measured 5 pixels down stream of the slip-line. For the sake of clarity, only a few arrows are drawn in the horizontal direction. For every pixel in the horizontal direction, a flow velocity is calculated by correlating the pixels in the surrounding area with an image from a later stage of the extrusion. The area that is correlated is contained inside a box of 80x80 pixels. The inserted square illustrates the size of this cut-out to be compared to a later image. As mentioned, note how the top of the box always is 5 pixels away from the slip-line in the flow direction.

We measure the fluctuations in the flow velocity of the material along the slip-line, ie. perpendicular to the flow. Figure 3.15 illustrates the spatial position of the measurements. If we measure imbalances in the flow out of the die, this means that different regions of the extruded profile exit the die with different velocities. This will make the extruded profile exit the die at an angle. From the velocity analysis described here, we obtain a flow chart allowing us to determine any imbalances in the profiles exit velocity. The result of one flow velocity analysis, containing the temporal evolving exit velocity along the slip-line, is shown in Figure 3.16.

The displacement of structures between two images of the slip region, separated by a time dt, tells us how fast the material is flowing. An example of two images that are correlated is shown in Figure 3.17. These two images are separated by four movie frames, or about 100 ms. The main difference in the images is the position of the bright lines, which are the grain boundaries

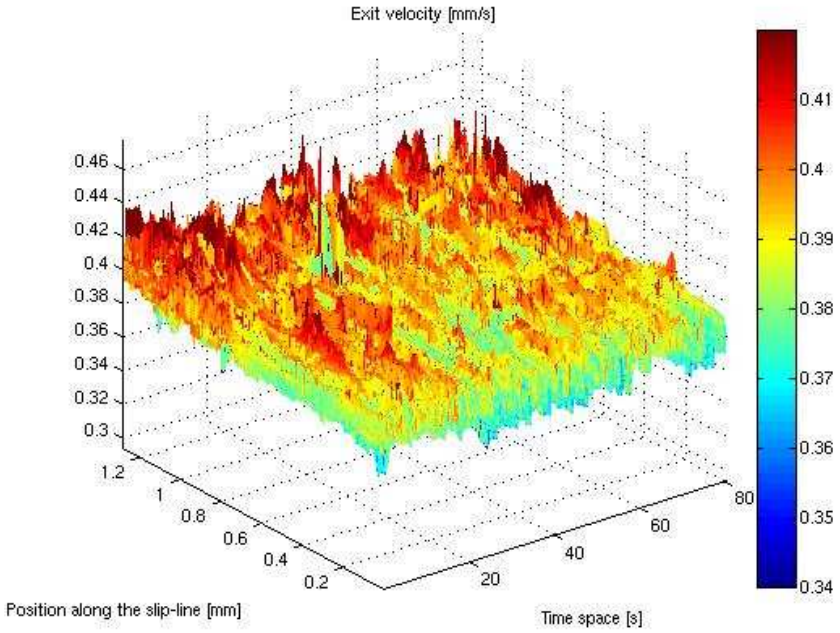

Figure 3.16: The temporal evolution of the extruded profiles surface-velocity measured along the slip-line. The velocity along the slip-line calculated by correlating structures in two pictures separated by the time dt.

in the extruded crystal. For a good correlation these lines should not overlap in the correlated images. It is the position of these lines and the dark region in between that we correlate to determine the extrusion velocity. Therefore, we remove the static background so only the moving objects in the images are left (see bottom of Figure 3.17). This is done by constructing an image comprised of the brightest pixels from the two images and then subtracting the two images from this background picture. The dark lines will not be contained in the background picture. After the subtraction, the lines are bright while the static parts are cancelled out and appear black. The two images are now ready do be correlated.

To obtain the flow velocity we follow the strain measurement technique published by Hung and Voloshin in [50]. The correlation method is as follows, we cut out boxes with identical pixel coordinates from the images. A box is made for every pixel in the direction parallel to the slip line, typically 500 pixels. The box size is usually 80x80 pixels. The boxes are chosen so that the top of them are 5 pixels away from the nearest point on the slip-line in

the cut out considered. The image cut-out from the first time-step is moved around on top of the later image cut-out to find the displacement that gives the best correlation. The correlation function is calculated according to

$$R = \frac{\sum_{i,j} \mathrm{IM1}_{i,j}\mathrm{IM2}_{i,j}}{\sqrt{\sum_i \mathrm{IM1}^2}\sqrt{\sum_i \mathrm{IM2}^2}} \tag{3.13}$$

where IM1 and IM2 are images (comprised of i×j pixels) of the same region in the die separated by a time dt. In Equation 3.13 the images are normalised by dividing by the length of the image vector for the two images respectively. This is to make up for uneven lighting in the regions of IM2 where we try to correlate IM1. Since all the pixels have intensities in the range 0 to 255, subtracting the mean is unnecessary. We move the box about 5 pixels in both directions parallel to the slip-line and 15 pixels in the flow direction. The result is the 11x16 2-dimensional correlation function R displayed in Figure 3.18(a). The best correlation is the maximum value in R. The indices of this maximum yields the displacement of the recognised structures in pixels. The occurrence of impurities flowing slowly on top of the material is a possible source of error for the correlation method. These impurities are not removed together with the background because they are moving from one picture to the next. Fortunately the impurities are so rare that we can overcome this problem by using large cut-outs when correlating.

A sub-pixel resolution of the displacement between the two pictures is obtained by fitting a function to the maximum value of the correlation matrix R and its eight neighbours, see Figure 3.18 for an illustration. Initially, we tried to fit a plane ($z = ax^2 + by^2 + cxy + dx + ey + f$) to the maximum point in R and its eight neighbours. This was not successful because around its maximum the correlation matrix often is very flat in the direction parallel to the slip-line. The explanation for this is the orientation of the identified grain boundaries, which often are aligned parallel to the slip-line (shown in Figure 3.17). Because of this, the maximum of the fitted plane did not always agree with the displacement found from the maximum value in the correlation matrix.

This problem is solved using shape functions to define the fitting function. The advantage of this method is that the requirements for the shape functions ensure that the fitted function has the same value as the correlation matrix in the nine points we are fitting it to. The details regarding the construction of the fitting function, $F(x, y)$, from shape functions are presented in A.1. The resolution of $F(x, y)$ is 1/100 of a pixel. The maximum of the fitting

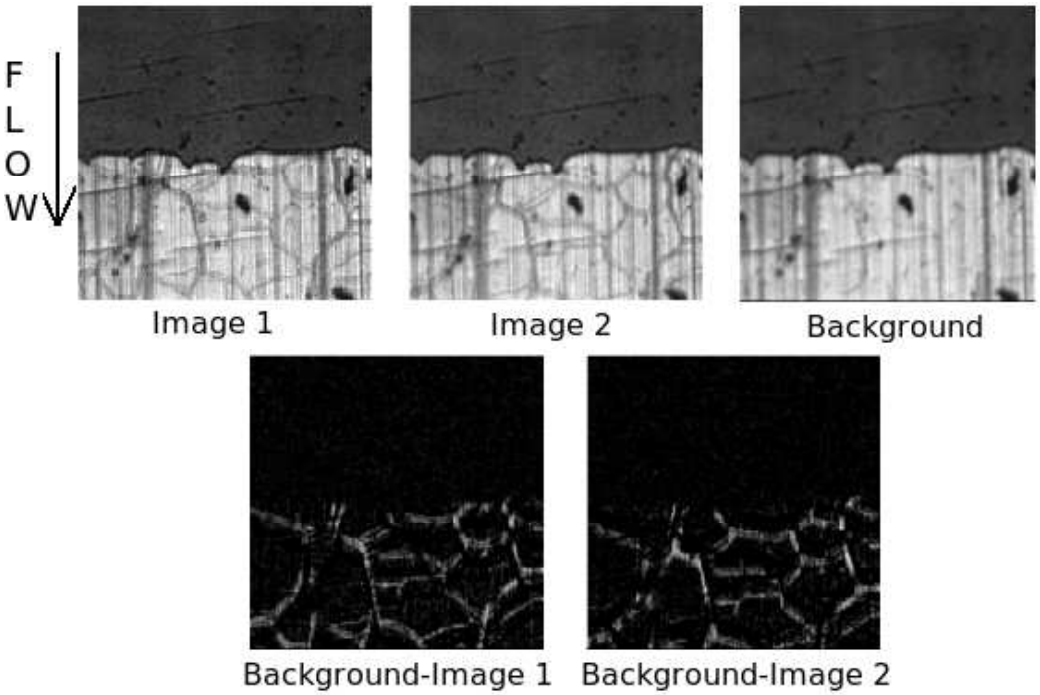

Figure 3.17: Image 1 and Image 2 are separated by a time dt. When we subtract them from their background (top right) image we obtain the two images to compare (bottom).

function $F_{\max}$ gives us the displacement between two pictures with sub-pixel resolution. We then convert pixel length to millimetres and calculate the extrusion velocity v_e using

$$v_e = \frac{F_{max}}{dt}\frac{[mm]}{[s]}.$$

This velocity measurement is an average along the slip-line because the width of the boxes we correlate is about a quarter of the total length of the slip-line. The implementation of this method, written for Matlab, can be found in C.4.

Bulk velocity profile

We also determined the bulk velocity of the material inside the flow by the correlation method described above. The flow velocity profile in the middle of the die is measured based on the relative movement of carbamid particles dispersed in a plane in the middle of the crystallines sample. The measurement was made by focusing in the middle of the die from a parallel view, see Figure 3.1 for the definition of parallel view. Figure 3.19 illustrates where in

the die the measurement is made. We must acquire 3 series of images from the inlet to the middle to cover the bearing channel in this region. These series are then put together to form a panorama image of the flow field throughout the die. We were not able to map the bulk flow from the middle of the die and out because of poor contrast in the slip-region. The poor contrast is due to the reflection from the profile surface in the slip region that we must film through to observe the carbamide particles.

We apply only as many tracer particles to the ingot as needed to obtain a good correlation and not effect the material flow adversely. The lack of tracer particles makes it difficult to obtain a complete velocity profile only by correlating two successive images. The incomplete velocity profile shown in Figure 3.20 illustrates the result obtained when only two images are used to determine the bulk velocity. The positions without values in Figure 3.20 correspond to locations in the die where there have been too few tracer particles in the images to obtain a good correlation. The complete bulk velocity profiles presented in Chapter 4.5.5 are comprised of the average of 100 successive velocity measurements.

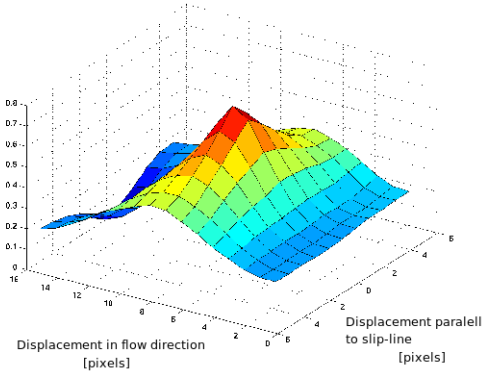

(a)

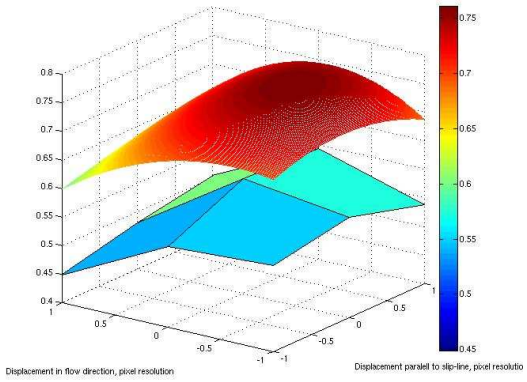

(b)

Figure 3.18: (a) Surface plot of the correlation matrix R obtained by correlating two successive images of the exiting extrusion profile. The maximum point of this surface corresponds to the distance the extruded material has moved between the two images. In this case, we see that the displacement is 8 pixels in the flow direction and 0 pixels parallel to the slip-line. We fit a function with sub-pixel resolution to the maximum point (3x3 point making up the maximum) to accurately determine the maximum. (b) Illustrates the fit obtained using shape-functions to construct the high resolution fitting function. The difference between using a plane equation and shape functions when fitting, is that the latter method requires the function to be equal to the correlation matrix where this is defined. The fitted function (top) is lifted from the correlation matrix R(bottom) for clarity. In reality, it passes through all nodes of R.

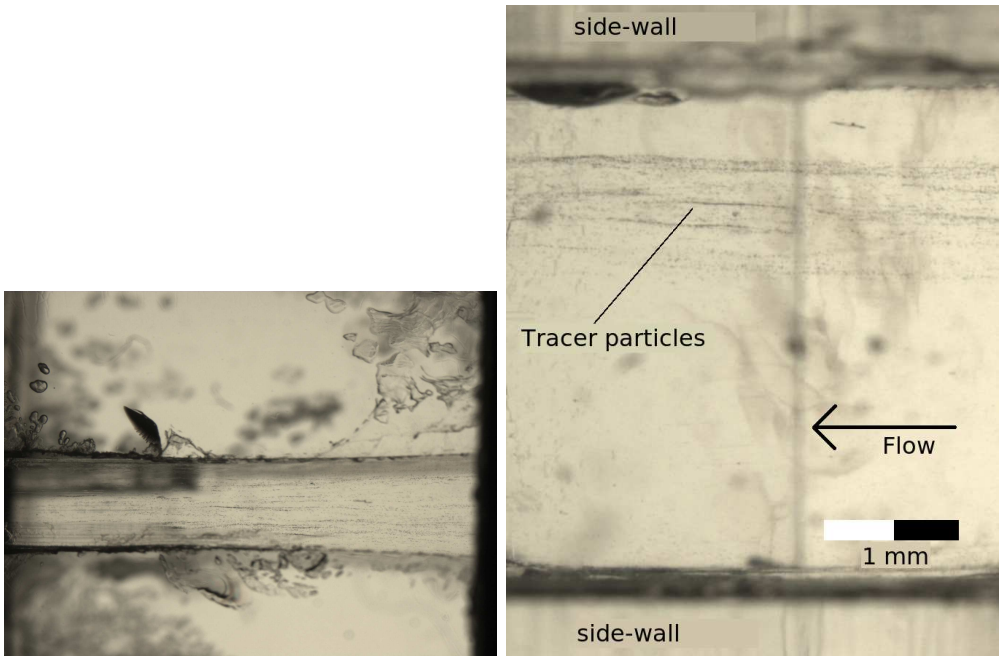

(a) (b)

Figure 3.19: The bulk flow velocity profile is measured by correlating the position of tracer particles dispersed on a plane in the crossing the middle of the die. This plane is orientated perpendicular to the curved bearing surfaces. (a) An overview of the die with the tracer particles. The images used for determining the velocity is taken from this viewing angle, but five times higher magnification. To map the flow from the inlet the middle of the die 3 image series along the bearing channel is required. The inserted black square indicate wher the measurement is made. (b) Microscope image taken in normal view of the die with the tracer particles. Note that the particles should ideally be in the middle of the die. However, because this sample was cut open slightly off-centre the particles ended up not flow entirely in the centre of the die channel. Both the images are taken from experiment S17, see Table 4.1 for more information regarding this experiment.

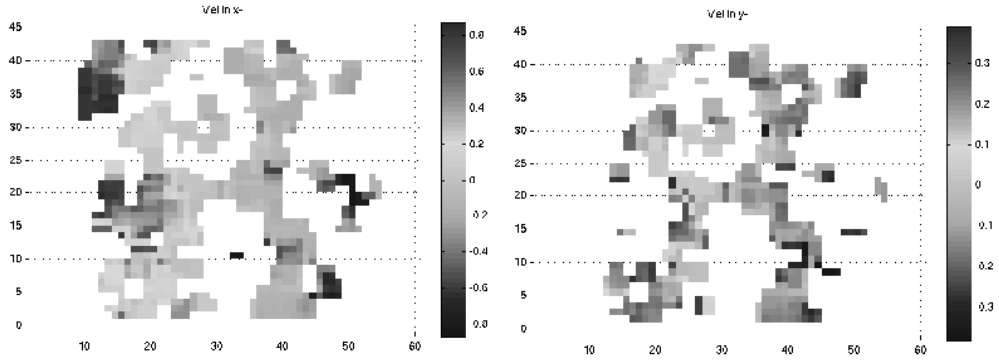

(a) (b)

Figure 3.20: The incomplete bulk velocity profile obtained from only one image correlation. There are not enough tracer particles to determine the velocity in the whole die just from two successive images. (a) is velocity perpendicular to the flow and (b) is the flow velocity. We have averaged over 100 correlations, that is 101 images, to obtain the more complete velocity profile shown in Section 4.5.5

3.5 Statistical treatment of experimental data

Up to now this chapter has explained how we extract information about the events inside the die. The fruits of this work are data-sets describing how the extrusion processes evolve with time. The temporal measurements we have obtained are; the slip-line position, the extrusion back pressure, the surface velocity of the extruded profile, and the bulk flow field. A visual representation of the three different types of raw-data we extract from the extrusion experiments filmed in normal view are displayed in Figure 3.21. The experiments where we determine the bulk flow velocity profile are filmed in parallel view, the raw-data we extract from these experiments are shown in Figure 3.20. We define the quantity width, w, as the width of the image cutout the slip-line is measured over, this is illustrated in defined in figSLposition. The width, w, which is constant throughout one experiment, is used to normalise several of the measurements calculated from the slip-line data. Table 4.1 list the value of w in the various experiments where the slip-line position is determined.

In the following sections we explain and discuss the statistical methods we have used in our analysis of the experimental data. Examples of what we used the different measures for are provided along with the recipes. We have used the high-level program Matlab® [51] to analyse the experimental data.

3.5.1 Mean and Standard Deviation of an discrete data-set

We have calculated the standard deviation of the evolving slip-line from each picture taken to get a measurement of the line's roughness. The discrete coordinates of the slip-line obtained from the image analysis are not equally spatial distributed. This complicates the calculation of the mean and standard deviation in the slip-lines position. The following section explains step by step how we calculated the mean and standard deviation of the slip-line from the discrete coordinates

For an continuous distribution, the standard deviation is given by

$$s = \sqrt{\frac{1}{L}\int_0^L (y(x) - \bar{y})^2 \, dx}.$$

The discretised expression is

$$s \approx \sqrt{\frac{1}{x_N - x_1} \sum_{i=1}^{N-1} \int_{x_i}^{x_{i+1}} (y_{i+1} - \bar{y})^2 \, dx}. \tag{3.14}$$

We approximated $y(x)$ to be linear between two data-points (see Figure 3.22)

$$y \approx= \frac{y_{i+1} - y_i}{x_{i+1} - x_i}(x - x_i) + y_i = \frac{y_{i+1}(x - x_i) + y_i(x_{i+1} - x)}{x_{i+1} - x_i}. \tag{3.15}$$

Now that we have an expression for $y(x)$, we can start working our way towards a discrete expression for Equation 3.14. This expression should only consist of known quantities, that is, the coordinates of the slip-line (x_i and y_i). We start by determining the expression for the mean of the line $\bar{y}$,

$$\bar{y} = \frac{1}{L} \int_0^L y(x) \, dx \approx \frac{1}{x_N - x_1} \sum_{i=1}^{N-1} \int_{x_i}^{x_{i+1}} \frac{y_{i+1}(x - x_i) + y_i(x_{i+1} - x)}{x_{i+1} - x_i}.$$

When evaluating the definite integral above at x_i and x_{i+1} we obtain the desired expression for the mean:

$$\bar{y} \approx \frac{1}{x_N - x_1} \sum_{i=1}^{N-1} \frac{y_{i+1} + y_i}{2}(x_{i+1} - x_i).$$

Let us continue with determining the expression for the standard deviation, Equation 3.14. We need to solve the integral

$$I = \int_{x_1}^{x_2} (y_2 - \bar{y})^2 \, dx,$$

where I have for clarity exchanged the subscripts $i + 1$ and i with 1 and 2. By substituting $a = \frac{y_2 - y_1}{x_2 - x_1}$ into Equation 3.15 we can write

$$y(x) \approx a(x - x_1) + y_1.$$

The integral can now be written

$$\int_{x_1}^{x_2} (a(x - x_1) + y_1 - \bar{y})^2 \, dx. \tag{3.16}$$

We simplify this integral by substituting $u = a(x-x_1)+y_1-\bar{y}$ and $du = adx$. Solving it gives

$$\begin{aligned}\int_{a(x_1-x_1)+y_1-\bar{y}}^{a(x_2-x_1)+y_1-\bar{y}} (u)^2\, dx &= \frac{1}{3a}\left[u^3\right]_{y_1-\bar{y}}^{a(x_2-x_1)+y_1-\bar{y}=y_2-\bar{y}} \\ &= \frac{x_2-x_1}{3(y_2-y_1)}\left((y_2-\bar{y})^3-(y_1-\bar{y})^3\right).\end{aligned}$$

When inserting this result into Equation 3.14 we obtain the following expression for the standard deviation of the slip-line,

$$s = \sqrt{\frac{1}{x_N-x_1}\sum_{i=1}^{N-1}\frac{x_2-x_1}{3(y_2-y_1)}\left[(y_2-\bar{y})^3-(y_1-\bar{y})^3\right]}.$$

This expression only depends on known coordinates obtained by image analysis of the slip-line experiment movies. We need to rewrite[9] the above expression to avoid the possibility of dividing by zero. The final expression we implement numerically is

$$s = \sqrt{\frac{1}{x_N-x_1}\sum_{i=1}^{N-1} x_2-x_1\left[(y_2-\bar{y})^2+(y_1-\bar{y})\left[(y_2-\bar{y})+(y_1-\bar{y})\right]\right]}.$$

3.5.2 Fast Fourier transform

It is interesting to see how the characteristic wavelength in one measured quantity effects other properties in the extrusion process. Examples of such important relations are how the periodic back-pressure effects the slip-line dynamics and the extrusion velocity. We use the built-in Fast Fourier Transform (FFT) routine in Matlab, fft, to determine the periodicity in various measures made from the extrusion experiment. An example of a pressure signal and its corresponding periodogram is shown in Figure 3.23. The peak in the periodogram reveals the characteristic frequency in the recorded back-pressure.

The period of the pressure signal is only determined for a part of the pressure reading during an experiment. This is because there are normally occur

[9] Where we have used that

$$\frac{a^3-b^3}{a-b} = a^2+b(a+b).$$

1-2 large pressure drop during the course of an experiment. The complete pressure profiles for three analysed experiments are shown in Figure 4.19(b) in section 4.5.5.

3.5.3 Position of the slip-line

We use the known position of the slip-line to calculate the area between a reference line (fixed in space) and the slip-line to determine how the transition zone moves in time. A positive differential area between two pictures corresponds to an average advancement of the slip-line in the flow direction (see Figure 3.24).

We use Greens theorem to calculate the area for each slip-line image. The theorem states that

$$\int_C (p(x,y)\ dx + q(x,y)\ dy) = \iint_A \left(\frac{\partial q}{\partial x} - \frac{\partial p}{\partial y}\right), \tag{3.17}$$

were C is a closed, positively oriented, and piecewise smooth curve. A is the area, and the partial derivatives are continuous, bounded by C . The fact that C is positively oriented means that the line integral has to be computed counterclockwise. When the integrand $\left(\frac{\partial q}{\partial x} - \frac{\partial p}{\partial y}\right) = 1$ then

$$\iint_A dxdy = \ Area\ of\ region\ A.$$

$p = 0$ and $q = x$ is one of infinitely many combinations but maybe the simplest of the functions p and q making the integrand one. Inserting $p = 0$ and $q = x$ into Equation 3.17 gives

$$\iint_A dxdy = \int_C x\ dy.$$

This result show that we can determine the area of a region by integrating over its boundaries. The blue lines in Figure 3.24 illustrate the boundaries we have to integrate over to determine the area associated with each slip-line. The numerical expression for calculating the area between the slip-line and the reference line is

$$Area = \sum_{i=1}^{N} (y_{i+1} - y_i) \left(\frac{(x_{i+1} - x_i}{2}\right),$$

where x and y are the coordinates of the slip-line and reference line.

Choosing a common reference line in the integration path allows us to calculate an area for each slip-line image. By subtracting the area of the preceding image we obtain the change in area between two images. However, we can obtain the change in area directly and omit using a reference line. If the boundary of the region is made up by two succeeding slip-lines, the line-integral yields the areal difference between the two lines (see Figure 3.25). This approach is more elegant, but gives us only the area change dA, whereas the method relying on the reference-line gives us an absolute area A for each picture. The change in area, dA, is simply the derivative of the area A.

3.5.4 Length of slip-line

The length of the slip-line in each movie frame is calculated by applying the Pythagorean theorem to the auto detected slip-line x- and y-coordinates. We simply integrate the lengths of the straight lines connecting neighbouring data-points in the slip-line data-set, according to

$$L = \sum \sqrt{(y_{i+1} - y_i)^2 + (xi + 1 - x_i)^2}.;$$

The data-set provided by the level-set image analysis tool has sub-pixel resolution. Therefore, this length measurement gives an accurate estimate for the temporal evolution of the slip-line length. We normalise the slip-line length by dividing by the width,w , it is measured over. The ratio of the slip-line length to the width for a Succinonitrile extrusion experiment is plotted in Figure 3.26. The plot has been filtered with a median filter for the sake of clarity. The same filter has been used on the length plots presented in the results chapter, section 4.5.3.

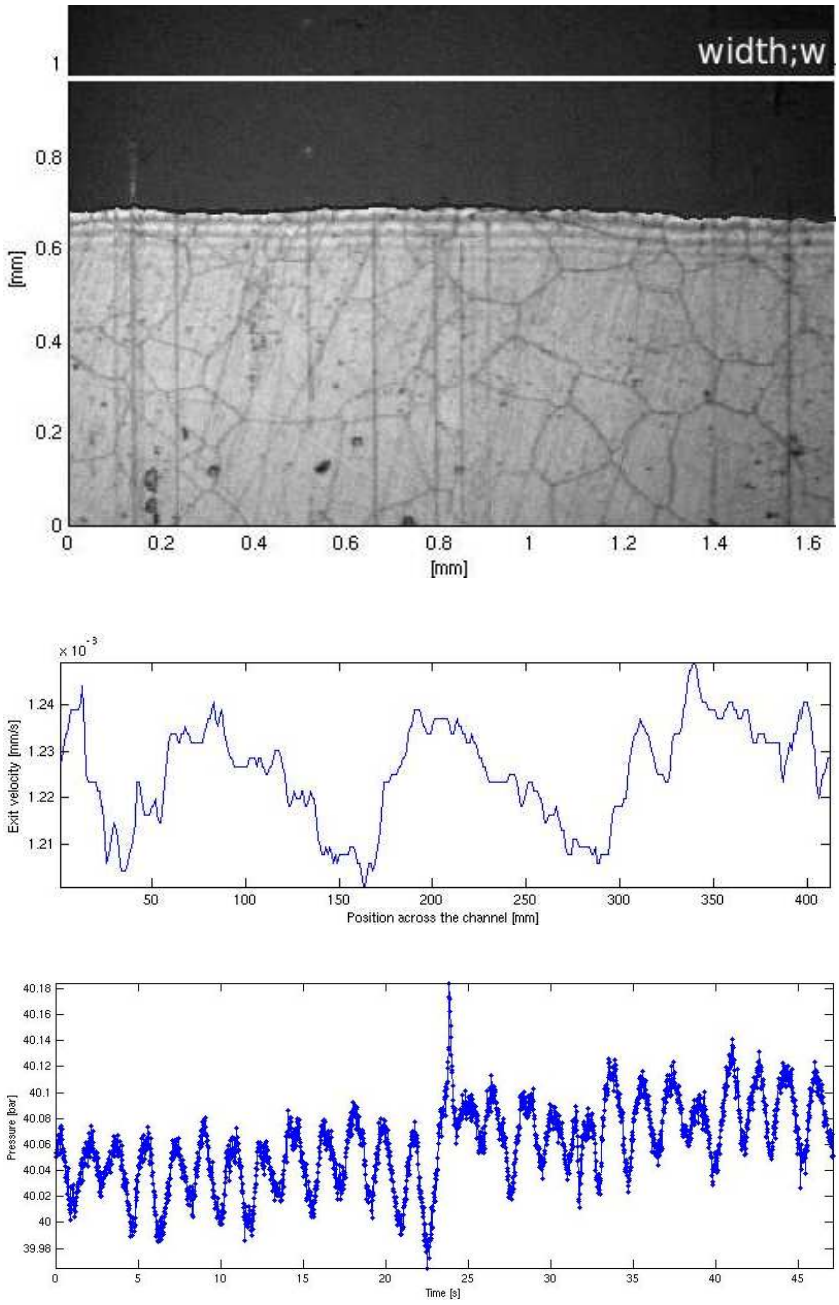

Figure 3.21: Plot of the three different measures we extract from the experiments where the slip-line is filmed. (a) The automatically detected slip-line position drawn in on the original image from the experiment. The slip-line position is extracted from every image and used to describe the dynamics of the transition. The length of the inserted white line defines the width, w, the slip-line measurement is made over, for this experiment $w \approx 1.65mm$. (b) One surface-velocity measurement of the extruded profile along the slip-line. Fluctuations in the velocity across the bearing channel will make the profile exit the die with an angle. An example of the temporal evolution of this measure is plotted in Figure 3.16.(c) Example of a back-pressure record acquired during the extrusion. We record the pressure 50 times per second.

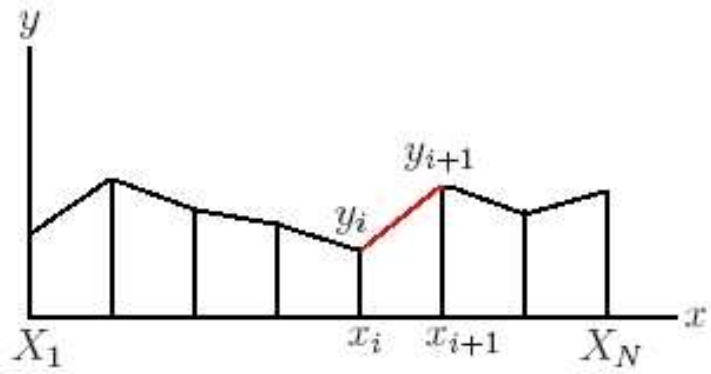

Figure 3.22: We approximate the position of the slip-line $y(x)$ with a linear function between the coordinates obtained from image analysis of the experimental data.

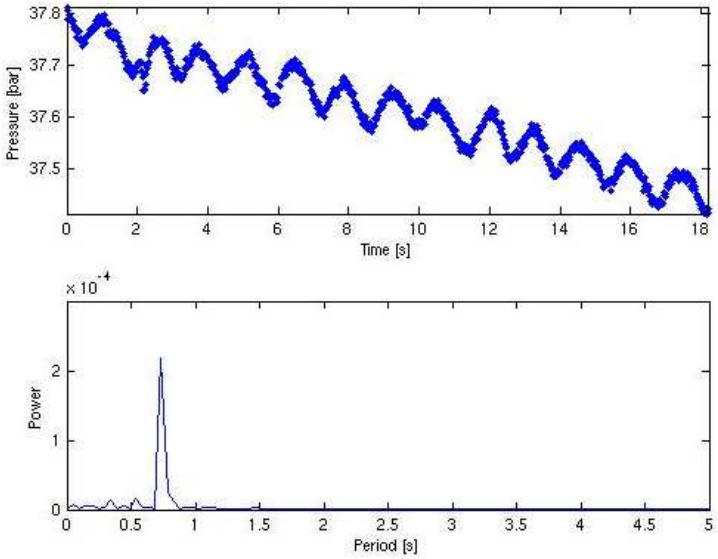

Figure 3.23: (a) The back-pressure recorded during extrusion of Camphene. We can see that the pressure delivered from the pump varies with a period of about 1-2 seconds. (b) The periodogram for the pressure variations determined from the discrete Fourier transform of the pressure signal. The peak in the power-signal at 0.73 Hz corresponds to a period of 1.36 seconds.

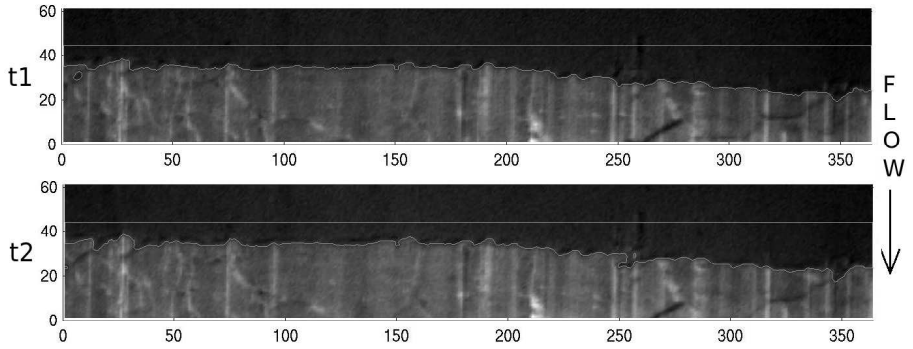

Figure 3.24: Images of the slip-line at two different times. The slip-line and a reference line are displayed on top of the images. The average fluctuation in the slip-line is analysed by calculating the area between a fixed reference line and the slip-line. If the area increases from one image to the next, then the average position of the slip-line has moved with the flow from top to bottom.

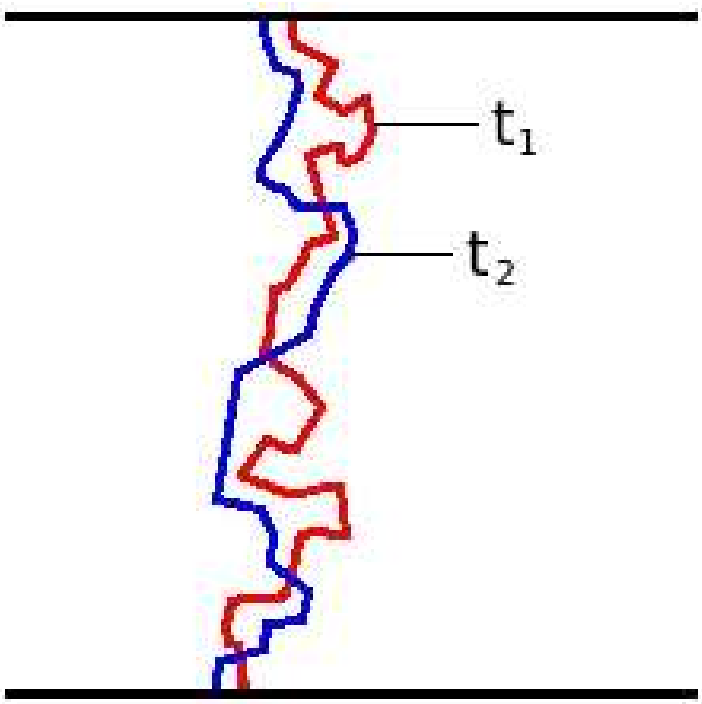

Figure 3.25: The average movement of the slip-line position between t_1 (red) and t_2 (blue) can be found by integrating Equation 3.5.3 over the boundary C made up by the two slip-lines at their respective times.

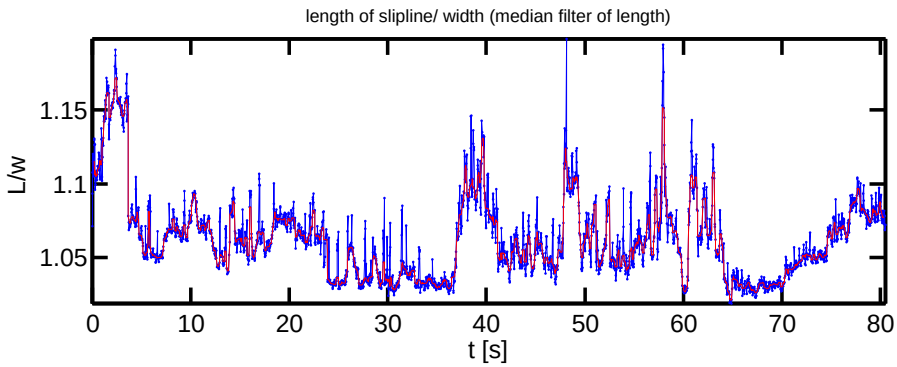

Figure 3.26: (a) The temporal evolution of the slip-line length divided by the width, w, the measurement is made over. In this example $w = 1.57\ mm$. This original data set, in blue, is difficult to compare with other measurements of the slip-line dynamic and flow velocity. Therefore, we have for clarity filtered the data set through a median filter, shown in red, with a bin size of 11 measurements. The filter we have written, picks out a window (also called bin) of 11 measures with centre in the value to be altered. The centre value is then seat equal to the median value of the window. This calculation is then repeated for all the measurements, except for the end-members surrounded with less than 11 neighbouring values.

3.5.5 Cumulative position of the slip-line within the die

This measurement describes where in the die the slip-line has spent its time during extrusion. This method loops through every slip-line extracted from the extrusion movie and counts how many times the slip-line is located at the same point in the die. The spatial resolution is equal to the pixel resolution in the acquired images. An example of a map showing the slip-line position is shown in Figure 3.27.

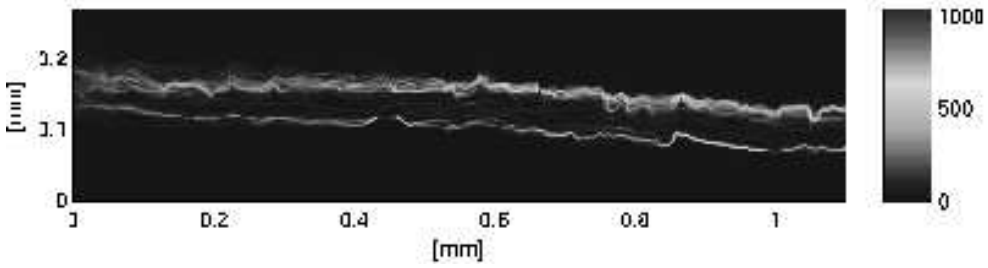

Figure 3.27: Figure showing how many times the slip-line has been observed at a certain point in the die. The resolution is equal to that of the captured image frames. The extrusion direction in this figure is from the top towards the bottom.

3.5.6 Probability distribution

From the measured area changes we calculate the area change probability density function p(x). This describes the probability for a given area change (or area jump) of size x to occur. The probability density is calculated from the formula [10]

$$p(c) = \frac{P(b) - P(a)}{b - a}, \tag{3.18}$$

where $P(b) - P(a)$ is the probability for the size of a random area change to be within the interval [a,b], (b-a) is the difference between the two end-

[10]To calculate the area change probability density function p(x) we have used the mean value theorem and the fundamental theorem of calculus. Assume that p(x) is continuous in the interval $[a, b]$. Then the mean value theorem states that

$$\frac{P(b) - P(a)}{b - a} = p'(c) \quad , \quad c \in [a, b].$$

We also use the fundamental theorem of calculus to recognise that $P(x) = \int_a^x p(x')dx'$, meaning that $\frac{d}{dx}P(x) = p(x)$. Combining the two theorems allows us to relate the probability for an area change to be in the interval $[a, b]$ with the probability density in the form shown in Equation 3.18

member area changes, and c is the average of the jump rates contained in the interval [a,b]. The approach we used to calculate the probability density p(x) is perhaps better explained with words. An array containing all the area change measurements are sorted in ascending order. Then we consider a given number (the bin-width) of measurements at the time. For a bin-width of twenty, this means first considering the twenty lowest values and then the twenty next and so on. The probability for a measurement $P(b) - P(a)$ to be in this selection is simply the bin-width divided by the total number of measurements N. The size of the interval (b-a) is the difference between the largest and smallest measurement in the selection. The c value is determined by the average of the measurements within a bin.

3.5.7 Scaling relationships

Scaling relationships are, in this thesis, used to study how fluctuations in a measure Δy scales with different coupling rates, Δt, of the data. Specifically, one wants to determine the function f in

$$\Delta y^2 = f(\Delta t).$$

We have used this approach to determine how average quantities measured in the extrusion experiment, $< \Delta y^2 >$, vary when the distance scale is varied. Figure 3.28 illustrates how varying Δt can influence $< \Delta y^2 >$.

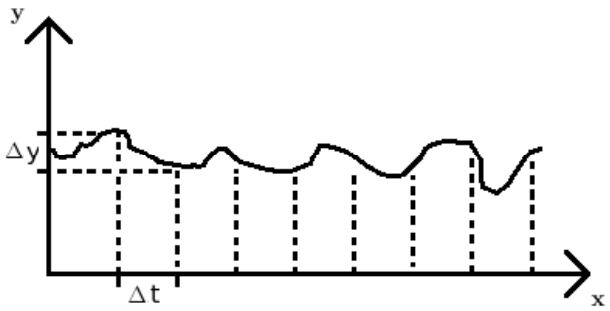

Figure 3.28: Illustration of the relation between the measured quantity Δy and the length scale, Δt, it is measured over. If the length scale Δt is varied, the average of the measured Δy will also vary.

The power law relationship between fluctuations and sampling rate,

$$< (\Delta y)^2 > \propto \Delta t^{2H},$$

have received much attention [52]. Here H is the Hurst exponent. By plotting $\log(<(\Delta y)^2>)$ as a function of $\log(\Delta t)$ we find H as the slope.

In the case where the quantity Δy arbitrarily increases or decreases for every time step, ie. equal to a random walk, the scaling exponent is $1/2$ (H=$1/2$) [52]. In this case there is no correlation between past and future area increments for any Δx. If $H \neq 1/2$, however, there are correlations between future and past increments. If $H > 1/2$ we have persistence, meaning that an increase has higher probability to be followed by another increase. Conversely, a decreasing trend in the past implies a decreasing trend in the future when $H > 1/2$. When $H < 1/2$ the system has antipersistence,, also referred to as being negatively correlated, meaning that an increasing trend implies a decrease in the future and *vice versa*.

Chapter 4

Results

The results presentation is divided into two parts: a qualitative discussion of the observations that are difficult to quantify, followed by a presentation of statistical measurements applied to the experimental data. The section concerning general observations is meant to give the reader a brief overview of all the observations that will be discussed later in this chapter. The parameters of the experiments mentioned in this chapter and following chapters can be found in Table 4.1.

4.1 General observations

Figure 4.1 shows a typical reflected light microscope image from inside the die during extrusion of Succinonitrile at $40°C$. We can clearly distinguish between two regions, one dark on the inlet side of the image and one brighter further down-stream. As explained in section 3.4, the two regions are identified as the stick-region and slip-region of the bearing channel. The intensity border separating the two regimes is the slip-line.

In the bright slip-region we can see some dark spots, which are moving in the direction of the material flow but with a much lower speed than the extrusion velocity. In this region, we also observe dark lines in a polygonal structure moving with the velocity of the extruded material. These are the grain boundaries of the polycrystalline material we extrude. We also see several dark straight lines aligned parallel to the direction of the material flow.

We clearly see continuous lines downstream from the ductile-brittle trans-

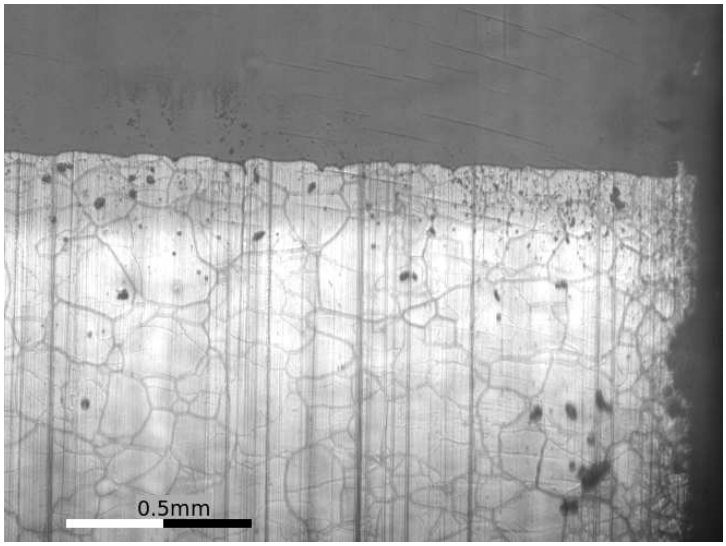

Figure 4.1: A reflected light microscope image showing Succinonitrile being extruded at $40°C$ through a die with a radius of curvature 24.8 mm. The plane of focus is on the bright profile surface in the lower part of the image. The flow is from the top towards the bottom. Notice the dark straight vertical lines running parallel with the flow. These are grooves in the extruded profile's surface. On the right side, the side-wall of the bearing channel is visible.

ition in Figure 4.1. These are grooves in the die that scratch the flowing material as it is extruded. Microscope examinations of Succinonitrile profiles directly after extrusion verifies this. The distribution of groves in the die corresponds to the lines in the finished profile. When Camphene is extruded, the same lines are observed directly downstream from the slip-line. However, microscope examinations of the Camphene profiles pressed through the same dies show no grooves. This suggests that the surface of Camphene heals as it exits the die or immediately after the extrusion process. Our visual inspections indicate that dies with a smoother surface finish also impose fewer grooves in the profile.

4.2 Overview of analysed experiments

We have conducted the extrusion experiments with the materials, Succinonitrile and Camphene, at 40° and 22° respectively. The radius of curvature of the bearing surfaces, R_c, was varied from 8.0-66.1 mm. The images of the

slip-line in the dies with the smallest R_c, 8.0 mm, have poor contrast. This is because the curved bearing surfaces focuses the light from the microscope at the same position as where the slip-line is located in the middle of the die. Therefore, we could not use the automatic slip-line detection methods to identify the transition in these experiments, but we have analysed one of them qualitatively.

4.3 Experimental conditions

We have experienced problems predicting the course of the extrusion experiments because of the many variables involved. When we start an experiment we expect one, or a combination, of the three following scenarios; **i)** the slip-line is observed as a sharp contrast border between the stick and slip region, **ii)** numerous asperities on the bearing surface in the stick regime scratch the extruded profile and upset the slip-line, **iii)** the gravity force and die-geometry effects move the slip-line close to the channel outlet. Examples of the three different scenarios are shown in Figure 4.2. The fact that we can not predict the outcome of an experiment has vastly increased the time we have used to conduct experiments in the laboratory.

Our focus has been to conduct experiments in the first category, **i**. In these experiments, the slip-line is clearly defined and suitable for automatic detection with the tools we have developed and described in the previous chapters. Therefore, the experimental results we present and discuss in this chapter are from this category if not otherwise stated. First, however, we will give a brief overview of the other experiment categories, **ii** and **iii**.

In the second category of experiments, shown in Figure 4.2(b), the slip-line is smeared out by the numerous lines created in the profile by the asperities adhering to the bearing surface in the stick regime. This problem normally arises in the later stages of the extrusion or in reused dies, where an adhesive layer has had time to form at the die walls. The adhesive layer allows particles to adhere to the bearing surface. The asperities are present in all the experiments, however, normally in vastly reduced numbers and are subject to further discussion in section 4.4.4, where they are referred to as micro-hills.

In the last category of experiments, **iii**, the slip-line is not positioned immediately down-stream from the middle of the bearing channel, but rather at the outlet of the die. This phenomenon is probably best explained by the

Exp.	Comp.	T_{ingot} [$^{\circ}C$]	R_c [mm]	Die	$\bar{P} \pm \Omega$ [bar]	Profile dim. [mm]	Δt [ms]	w [mm]
Quant.								
S1	SNC	40	66.1	19	40.9±0.2	4.1×1.3	±0.7	1.59
S2	SNC	40	24.8	16	40.1±0.1	1.2×4.0	±0.7	1.57
S3	SNC	40	29.1	15	37.8±0.1	1.3×4.1	±0.7	1.66
S4	SNC	40	24.8	N/A	45.5±0.3	N/A	±12.7	1.78
S5	SNC	40	29.1	5	56.7±0.1	1.3×4.0	±12.7	1.81
S6	SNC	40	44.6	6	55.8±0.2	1.4×4.2	±12.7	1.62
S7	SNC	40	44.6	7	61.9±0.9	1.3×4.2	±12.7	1.69
S8	SNC	40	24.8	3	38.5±0.2	1.3×4.1	±12.7	1.09
S9-B	SNC	40	8.0	10	Sec. 4.5.5	1.3×4.1	±0.7	N/A
S10-B	SNC	40	66.1	17	Sec. 4.5.5	1.3×4.0	±0.7	N/A
Qualit.								
S11	SNC	40	29.1	2	varied	1.0×4.0	12.7	N/A
S12	SNC	40	8.0	11	34.7±0.12	4.1×1.3	12.7	N/A
S13	SNC	40	44.6	18	54.2±0.41	4.0×0.9	12.7	N/A
S14	SNC	40	44.6	18	51.1±0.09	1.3×4.0	12.7	N/A
S15	SNC	40	66.1	19	38.4±0.13	1.3×3.9	12.7	N/A
S16	SNC	40	8.0	11	38.9±0.07	1.3×4.0	12.7	N/A
C1	Camph.	22	24.8	4	21.9±0.12	1.3×4.0	12.7	N/A

Table 4.1: Overview of analysed experiments. T_{ingot} is the temperature of the ingot when the extrusion is initiated, thus equalling the set-temperature of the thermal control system. The die number identifies the die used in the experiment. The specifics for each die is listed in Table 4.2. The average back pressure during the extrusion is $\bar{P}$. The profile dimension is the thickness and width of the extruded profile measured with a calliper. The estimated error in the recorded time between two successive images is stated as Δt. The width of the bearing channel for which the slip-line position is measured over is stated as "w" for the experiments that are analysed quantitatively.

Die number	R_c [mm]	Height×Width [mm]	Reduction ratio
5	29.1	1.03×4.05	13.6
6	44.6	1.26×4.20	10.7
7	44.6	1.01×4.19	13.4
15	29.1	1.31×4.01	10.8
2	29.1	0.94×4.02	15.0
11	8.0	1.34×4.07	10.4
16	24.8	1.24×4.08	11.2
19	66.1	1.01×4.20	13.4
3	24.8	1.17×4.19	11.6
4	24.8	1.21×4.02	11.7
10	8.0	1.31×3.95	11.0
17	66.1	1.34×4.14	10.2
18	44.6	0.91×4.01	15.6

Table 4.2: Specifications on dies used in analysed experiments. The die number identifies the die, the die used in the various experiments is stated in Table 4.1. The height and width is measured at the middle of the bearing channel, thus where the cross-sectional area, or die opening, of the channel is nominally the smallest. The reduction factor is the ratio of the cross-sectional area of the ingot, $56.7mm^2$, and the die opening.

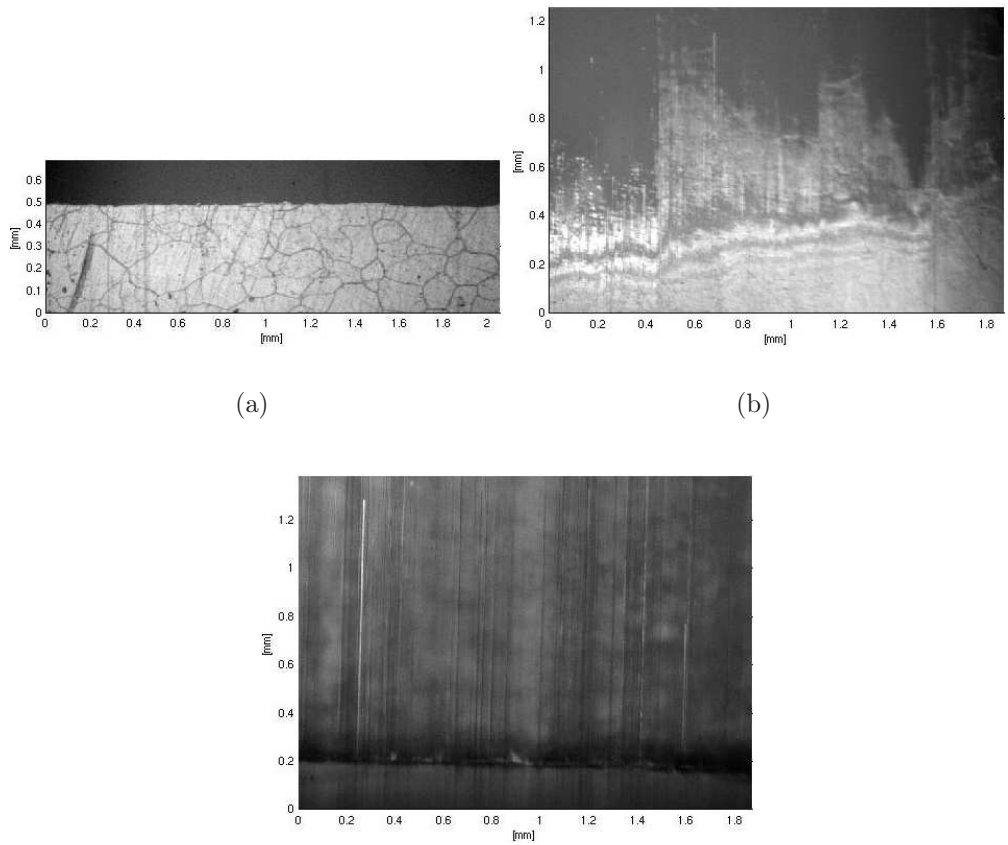

(a) (b)

(c)

Figure 4.2: The three main categories of experiments. (a) A sharp transition from stick to slip conditions (experiment S2). These experiments can be analysed with our image analysis tools. (b) The contrast changes gradually from the dark to the bright region. Note the Newton rings that are visible down-stream from the slip-line (experiment S13) (c) Stick conditions prevail throughout the bearing channel and the slip-line can not be observed.

combined effect of gravity pull on the profile and an undesired skew in the die.

An offset between the curved die walls will change the position of the narrowest point in the bearing channel. The effect this will have on the slip-line position is illustrated in Figure 4.3. The effect gravity plays in the extrusion experiments are the same for all experiments and is explained in the following section 4.3.1.

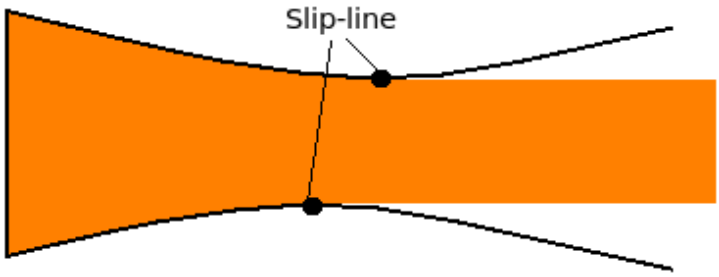

Figure 4.3: Illustration, in parallel view, of how an offset along the flow direction between the bearing walls will change the narrowest point in the channel. This will influence the average position of the slip-line and is one likely explanation for why we sometimes observe the slip-line further down-stream than expected. The offset is too small to be detected in our current die assembly process.

4.3.1 Gravity pull on the profile

The microscope objective is situated underneath the die in our experiments, therefore, gravity affects the boundary conditions at the two curved bearing surfaces differently. Material at the bearing surface closest to the microscope, where the top slip-line is observed, is pulled towards the die wall. By the same token, the material at the bearing surface furthest away is pulled away from the die wall.

The following example illustrates how we established that gravity pull in the bearing channel has a direct effect on our observations. In some experiments, the stick-regime that covers the whole bearing surface when an experiment is initiated does not recede as normal. In these experiments, we have observed the slip-line recede upstream and stay stable close to the die center by increasing the flow through the die. An example of this is experiment S11. As in all the experiments, the first material that entered the die adhered to the bearing surface. As more material came in, the material moved forward until the whole die exhibited stick boundary conditions. We waited several minutes for the slip-line to appear at the die outlet and then to recede backwards followed by the slip boundary condition. However, in this experiment the slip-region never appeared. Through small scratches in the opaque stick layer we observed that the velocity of the profile was noticeably slower compared to other experiments. At this time the pressure was 47 bar. We then doubled the flow-rate from the pump, increasing the back pressure to 78 bar, thus increasing the velocity. This made the the slip-line appear at the outlet and recede to the middle of the die. Since we can only measure the flow surface velocity in the slip-region, it is impossible to compare the exit speed of the profile before and after we increased the strain rate.

The speed of the exiting profile is, under normal extrusion conditions, high enough that the effect of gravity is negligible. This conclusion is based on observations of the top-bottom slip-line instability (discussed in section 4.4.1); the two slip-lines spend equally much time being furthest downstream. When the velocity of the exiting material is very low or the flow is halted completely, gravity can make the stick region extend further down-stream than it would without the effect of gravity pull.

4.4 Qualitative observations

Much extrusion literature is focused on phenomena that have implications for the finished product and how industry may expand the usage of extrusion. We have observed several of these interesting issues in our extrusion experiments. However, these processes are difficult to quantify with our experimental setup. What follows are, therefore, qualitative descriptions of our findings.

The material that enters the die when a new press is initiated covers the whole bearing surface with stick conditions. The stick regime prevails all the way from the die inlet to the outlet for about one minute into the extrusion process. About 1 minute into the pressing, the slip-line slowly recedes to its preferred position just downstream from the narrowest opening in the middle of the die. The slip-line will oscillate around this position for the rest of the extrusion. In the dies with sharpest curvature, $R_c = 8mm$, the initial slip-line only progressed about 1 mm past the middle before it receded after some seconds to a stable position.

4.4.1 Top-bottom slip-line instability

When we press Camphene or Succinonitrile through the die, both the top and bottom slip-line are visible by changing the focus on the microscope. Figure 4.4 illustrates the concept of an upper and a lower slip-line. The two lines can exchange positions during an experiment. For example, the top slip-line can be positioned about one millimetre upstream relative to the bottom slip-line when change places, and then the top slip-line becomes the one positioned downstream. They normally go to the exact same place as where the other line was previously located. This phenomena is occurs in almost all experiments with Camphene, but is only observed a few times when Succinonitrile is extruded.

In Camphene experiments where the radius of curvature in the die was $R_c = 44.5mm$, the top and bottom slip-lines are separated by about 1 mm in the flow direction. The line change takes place every 80-100 seconds and the change itself takes about 10 seconds. When Camphene is extruded in a die with $R_c = 25mm$, the offset between the slip-lines is about 0.3 mm and they are not observed changing places. As one might expect, our general observations support the trend that smaller curvature reduces the top-bottom slip-line instability. While the slip-line in Camphene extrusions can move

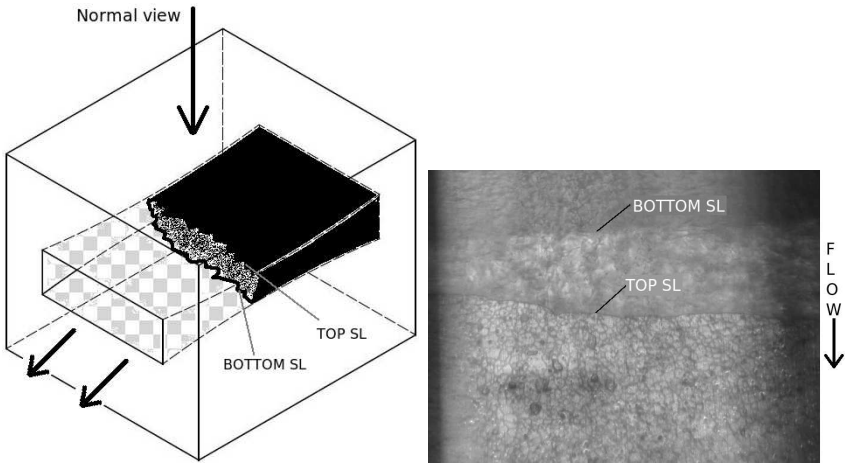

(a) (b)

Figure 4.4: **Left:** Schematic view of the extrusion die illustrating the top and bottom slip-line. The stick region is indicated by black material, and the slip region by grey dots. The extrusion direction is indicated by the two parallel arrows. The extrusion movie is filmed through a microscope mounted in normal view. By adjusting the focus of the microscope, one can observe either the upper or lower slip-line. **Right:** Image displaying the upper (horizontal line labelled TOP SL) and lower slip-line. In experiments with Camphene, the two lines swap positions.

more than a millimeter, the largest movement observed in Succinonitrile is only a fraction of this.

We have not observed that one of the slip-lines spends more time being the one furthest up or down-stream for experiments in category **i** and **ii**. This is, however, not true for the category **iii** experiments.

4.4.2 Adhesive layer inside the die

Figure 4.5 show an image taken during the extrusion of Camphene where a light-reflecting layer covers the bearing surface. The slip-region in this image is almost opaque and we cannot discern the structure of the grain boundaries. We can, however, see the extruded profile surface flow under this bright layer. Therefore, we believe the layer to adhere to the bearing surface. This layer can only be observed in the part of the die with slip, because the stick

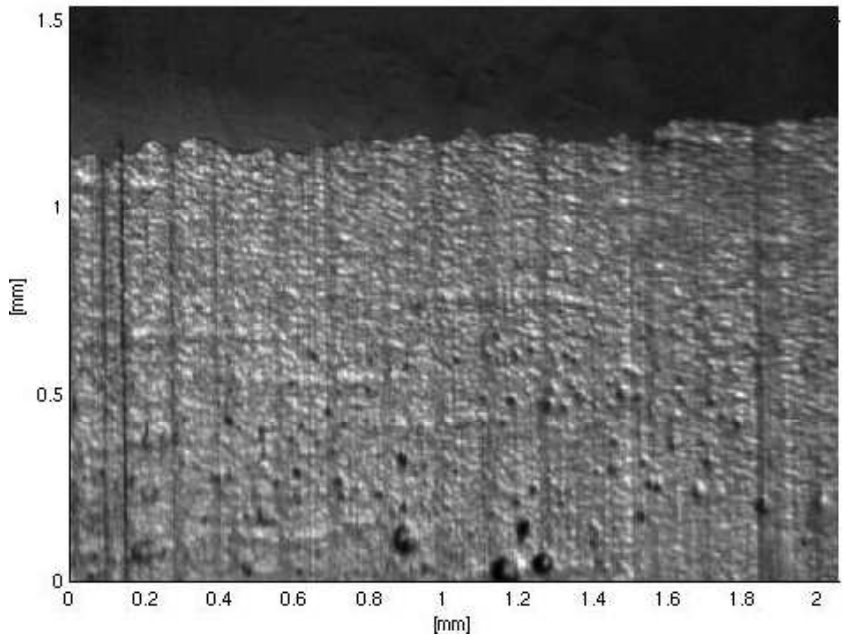

Figure 4.5: In this Camphene extrusion experiment a stationary reflective layer almost block our view of the moving profile surface. We can however see the material flow the under the layer that is believed do adhere to the bearing surface. From the extrusion movie can we barely make out the grain boundaries in the newly formed Camphene profile. Experiment name C1.

region always appears dark. The exception is in the case of micro-hill lines described in section 4.4.4. Experiments with both materials, Camphene and Succinonitrile, show formation of an adhesive layer, but not all experiments develop a noticeable layer.

When a new experiment is initiated in an unused die, the slip region downstream from the slip-line appears clean and the surface of the crystalline profile can be observed clearly. This means that the adhesive film is either transparent or not present. However, if the slip-line advances in flow direction, ie. the stick regime expands, and then to retreat upstream again, dark spots appear in the region swept by the slip-line. We have observed two mechanisms allowing the stick regime to expand for several millimeters in the flow direction. Firstly, the top-bottom slip-line instability. The second is halting the flow. The latter allows the stick region to advance through the die until the whole channel surface is covered by the crystalline material. This is probably caused by the gravity force. Since we are filming from underneath

the press, we simply see the extruded profile being bend towards the die. When the extrusion is resumed the stick region retreats back upstream.

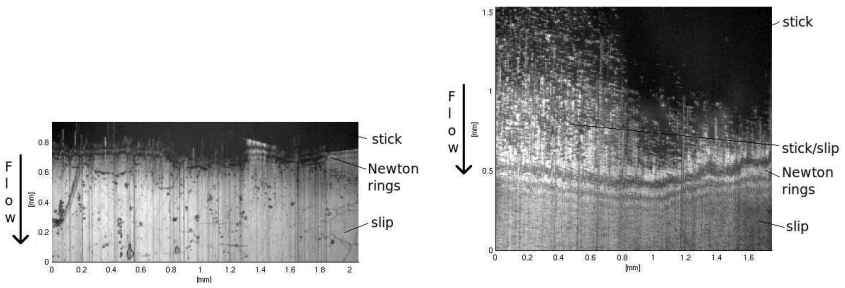

(a) Experiment S16 (b) Experiment S13

Figure 4.6: Microscope images from a Succinonitrile extrusion. Note the Newton rings that are visible in both images. (a) Experiment where there is a gradual contrast change between the stick and slip region and dark spots of material is visible on the bearing surface in the slip-region. (b) The stick and slip region is separated by a region that appear to have a mix of stick and slip conditions. The moving extrusion profile is visible through an almost opaque layer in the bottom of the image.

As the dark spots become more abundant during the course of extrusion, they can be described as a layer covering the slip-region close to the slip-line. Examples of this in Succinonitrile extrusions are shown in Figure 4.6. The first example, Figure 4.6(a), shows an area with a gradual contrast change from the dark stick region to the bright slip-region. The gradual contrast change is caused by material that stands still relative to the flow and appears to be stuck on the bearing surface. The dark lines running parallel with the slip-line in this figure are Newton rings. These fluctuate up and downstream much the same way the slip-line does in the experiments with a sharp stick-slip transition. Figure 4.6(b) shows the same features. However, the layer covering the slip-region in this example appears more opaque and there is a layer that, determined from the reflected light, appears to be a mix of stick and slip conditions. We interpret the this as a a region with a very dense deposit layer where there is very little space separating the bearing surface and the extruded profile. What we mean by "very" will be explained in the following section 4.4.3 where we calculate this separation using the Newton rings.

A similar spot-like layer covering the die is reportedly observed in post-extrusion examination of dies used for aluminium extrusion [8]. In these observations, the layer is composed of spot-like aluminium deposits in the stick-region and a layer that completely covers the bearing surface in the slip-region. The presence of the layer is believed to improve the surface quality of the extruded material [53, 54, 55]. This is because scratches and defects in the die are filled with the extrusion material, in that way inhibiting grooving of the extruded profile (or die lines) on its way out.

4.4.3 Newton rings

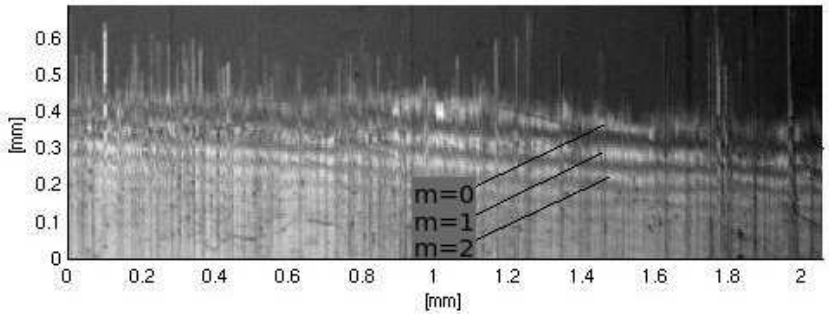

Figure 4.7: Microscope image taken from a Succinonitrile extrusion, experiment S15. We have used the Newton rings, m=0,1,2, to determine the separation, t, between the bearing surface and the extruded profile.

The newton rings observed in the extrusion experiments, shown in Figure 4.6 and Figure 4.7, are caused by interference in the light that is reflected from the profile-air interface and the bearing surface-air interface. The Newton rings can be used to make an order of magnitude estimate of the separation between the two interfaces. We can use the three lines in Figure 4.7 to obtain the slope in the spacing between the bearing surface and the profile surface. In other words, we determine, how much the profile surface separates from the bearing surface per length,ds , in the flow direction.

Where the lines are bright, the spacing, t, between the interfaces is given by,

$$t = \left(m + \frac{1}{2}\right)\frac{\lambda}{2} = \left(m + \frac{1}{2}\right)275nm \qquad m = [0, 1, 2...],$$

where λ is the wavelength of white light ($\approx$550 nm) and m is the number of the of the line[56]. For the bright line positioned most upstream m=0, see

Figure 4.7. In this image, the m=0 and m=2 lines corresponds to $t = 137.5$ nm and $t = 687.5$ nm respectively. And they are separated by $ds \approx 150\mu m$ in the flow direction. This gives a slope of $\Delta t/ds = 3.67 \times 10^{-3}$ or a 3.67 nm increase in the separation t for every μm ds in the flow direction.

Let us calculate the steepest slope where we can see newton rings in our experiments. In the experimental images, the size of one pixel is $1.56\mu m$. If we assume we need at least 10 pixels to distinguish two bright Newton rings, this corresponds to a distance of 15.6 μm in the flow direction. The difference in t between two neighbouring rings is $\lambda/2 = 275nm$, which gives a slope of 17 nm of separation per 1 μm in the flow direction. When the separation between the profile and bearing surface is steeper than this, we will not be able to detect the newton fringes.

4.4.4 Micro-hills

We have observed particles that adhere to the bearing surface in the stick-region in almost all the extrusion experiments. Figure 4.8 shows the presence of these particles. In this example, many of the particles are tailed by a bright line in the flow direction. In other examples, the tailing lines can be darker and shorter and therefore more difficult to observe. The position of the particles corresponds to dark lines in the extruded profile that become visible in the slip-region. The lines become more pronounced with increasing particle size. The particles can break loose from their site and move with the flow towards the slip-line for then to stop at a new site or simply disappear into the bulk flow. If the latter is the case, the dark line that was also previously observed downstream from the particle disappears. We, therefore, believe the particles are asperities on the bearing surface that groove the material as it flows past. Ridges on the surface in the bearing channel damaging the extrusion profile are reported in [8], where they are referred to as micro-hills. We believe this is the same phenomenon as we are observing. Therefore, we will refer to particles that adhere to the bearing surface and scratches the profile as micro-hills in the following sections.

There are also dark spots on the bearing surface in the slip-region. Their size varies from small enough to only appear as a dark regions when abundant, to large islands with an area of several $100\mu m^2$. We interpret them as small pieces of the extruded material deposited on the interior of the die. The deposits are affected by the material flow and generally move slowly downstream. They seem to be the only means of contact between the profile

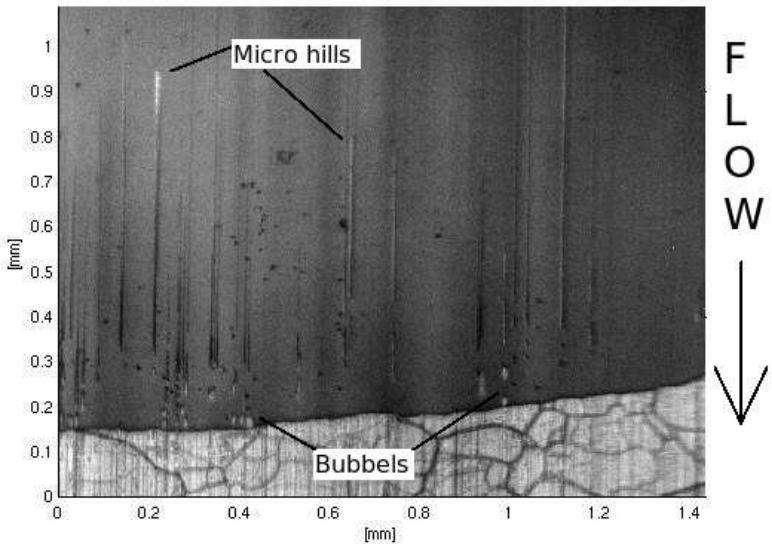

Figure 4.8: Microscope image of the slip-line from a Succinonitrile extrusionn a die with radius of curvature $R_c = 24.8$ mm. The presence of an adhesive layer on the bearing surface allows small asperities, referred to as micro hills, to form and grow. The micro hills are made up by extrusion material deposited on the die surface. The bubbles appearing close to the slip-line can be gas that has filled the groves in the extrusion profile downstream from the micro hills.

and the die after slip has occurred.

In our experiments, most of the deposits in the slip region do not seem to scratch the profile noticeably compared to the grooves made by the micro-hills in the stick region, which are already present in the profile-surface when it emerges from the stick region. There are, however, some micro-hills in the slip-region creating grooves of the same size as those originating from the stick-region. At the later stages of the extrusion press, the lines originating from the stick region often become more abundant in the profile surface. A cumulative formation of asperities on the die surface in the stick region is a plausible explanation for this grooving.

Figure 4.8 shows bubbles nucleating in the stick regime about 1 mm upstream from the slip-line in an Succinonitrile experiment. The gas is released at the end of the lines created by micro hills that are situated on the bearing surface in the stick region of the die.

Immediately after a micro hill, there is a drop in the normal pressure exerted by the bearings on the extruded material. This allows the gas trapped in the crystalline sample to emerge into the fresh groove in the profile. The gas can be seen as bright lines in behind the micro-hills in Figure 4.8. There is normally not enough gas trapped in the sample to see the formation of bubbles. The presence of gas in this particular experiment is probably due an abnormality in the preparation of the ingot prior to the extrusion.

Micro-hills can suddenly form on the bearing surface just downstream from the slip-line and then 5-20 seconds later disappear and be replaced with the continuous film. The image series in Figure 4.9 shows an example of this phenomena in a Succinonitrile extrusion experiment (experiment name S12). In this example, the slip-line makes a small advance downstream and immediately after micro-hills are formed. The micro-hills sit in the same position on the bearing surface for about 10 seconds and scratch the profile surface that flows past. We measure no abnormal fluctuations in the back pressure that could explain the sudden advancement of the slip-line.

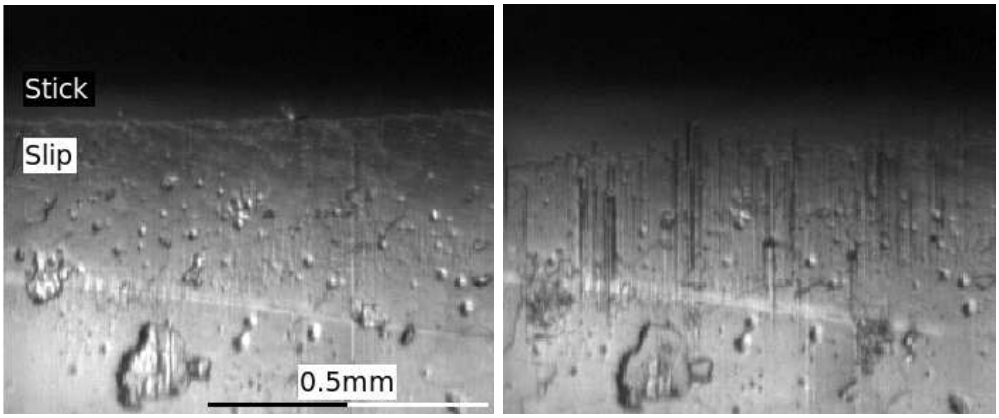

(a) t=0 sec. (b) t=1.4 sec.

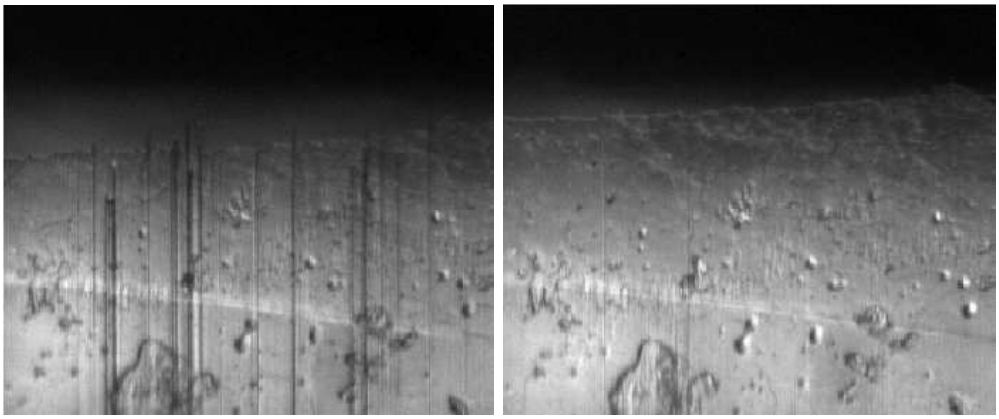

(c) t=8.0 sec. (d) t=10.9 sec.

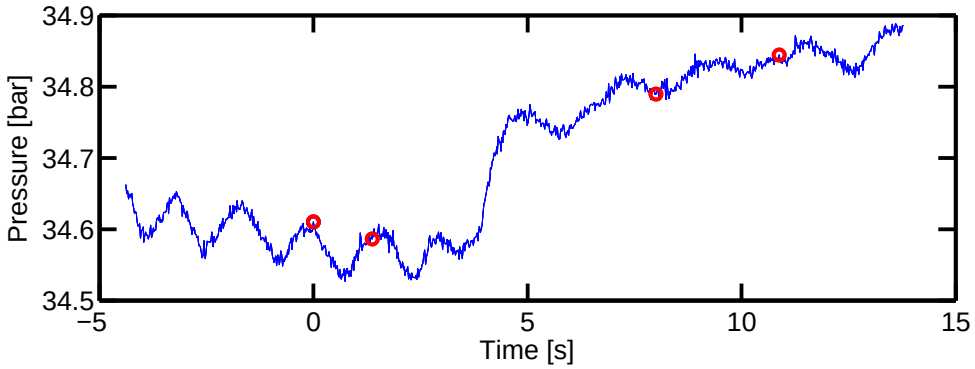

Figure 4.9: The image series show how the slip-line suddenly make an advancement and scratches the profile. (a) Note the large island on the bearing surface immediately left of the scale bar. (b) The slip-line suddenly advances about 0.2 mm, and the deposits on the bearing surface are moved down-stream. (c) The scratches begin to disappear. (d) The profile is back to normal. (e) The back-pressure recorded during this event, the acquisition times for the images (a-d) is indicated with circles. Experiment name S12.

4.5 Statistical measurements

The results from different statistical measurements characterising the behaviour of the dynamic ductile-brittle transition are presented in this section. The findings presented in the following sections are, if not otherwise stated, based on the eight experiments listed as "quantitatively analysed" in Table 4.1.

4.5.1 Slip-line area fluctuations

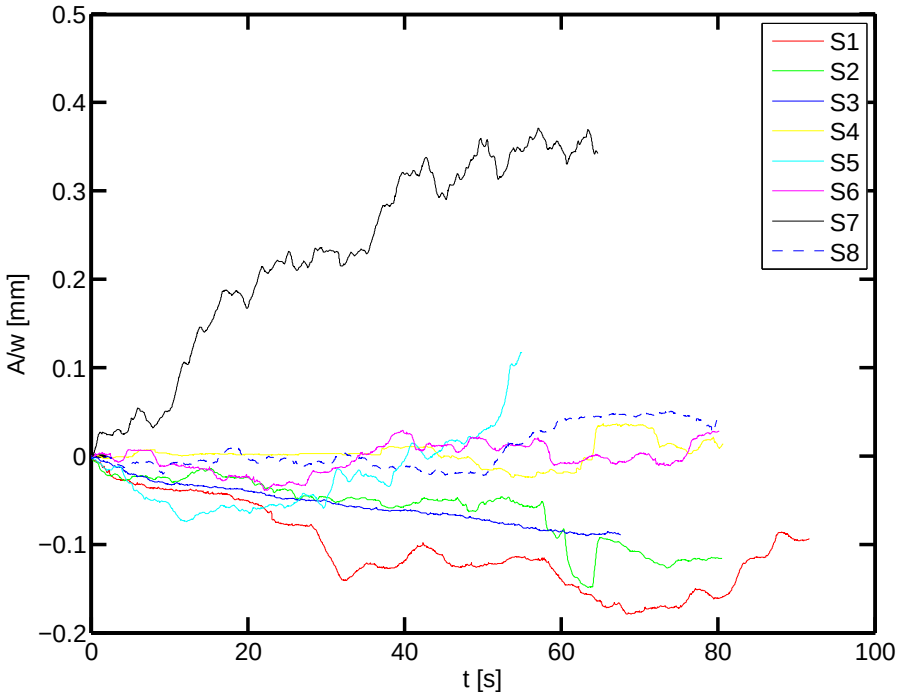

Figure 4.10: The normalised area, A/w, as a function of time for eight experiments. The first measurement is set to zero at t=0. There is a clear difference in how much the area fluctuates in the different experiments.

One measurement that characterises the dynamic behaviour of the slip-line is how the areas covered by stick and slip in the die varies during an experiment. On average, when the slip-line advances forward in the flow direction, the stick area increases while the slip region decreases. We measure the area covered by the sticking regime for every image in the extrusion

experiment movie. The details of how this measurement is made from the extrusion movies are described in section 3.5.3. We have normalised this measurement by dividing by the width, w, the measurement is made over. This normalised measurement is henceforth simply referred to as the area, A/w. This measure has the dimension of length and is a measure for the mean position of the slip-line.

The slip-line is, on average, stable in the experiments we have analysed quantitatively. This is shown in Figure 4.10. In three of them, the slip-line moves slightly upstream and in one experiment the area covered by slip increases. The standard deviation of the area fluctuations for the eight experiments, calculated from the timeseries in Figure 4.10, are listed in Table 4.3

In Figure 4.11 have we subtracted the mean area and removed the linear trend from the area measurement. This allows us to analyse the fluctuations in the measurement. If the large trends in the signal are fluctuations, their wavelength is too long to be analysed with this data. We can see how the fluctuations never deviate far from the mean area. This behaviour is further supported by area probability density plotted in Figure 4.12. The width of the distributions in this figure reflect the standard deviation of the area fluctuations seen in Figure 4.11. Experiment S3 and S4 show very small fluctuations and have corresponding very narrow probability distributions. The general trend for all the data is a noisy bellshaped curve.

The behaviour of the measured areas is in agreement with what we expected from the experimental setup. The position of the slip-line is focused in the area where the curved bearing channel starts to expand after its narrowest point.

Figure 4.13 shows how the mean squared area, $< (\Delta A/w)^2 >$, scales with time, Δt, in the experiments. We assume a power-law scaling relationship of the form

$$< (\left(\frac{\Delta A}{w}\right)^2 > \propto \Delta t^{2H},$$

where H is the power-law scaling exponent. The slopes in Figure 4.13 correspond to a H in the range 0.75-0.9. Thus we have persistence, meaning that the data has positively correlated increments. The slope of the time-series for $< (\Delta A/w)^2 >$ shows a decreasing trend for larger Δt. This suggests that the correlation between the future and the past area changes vanishes for

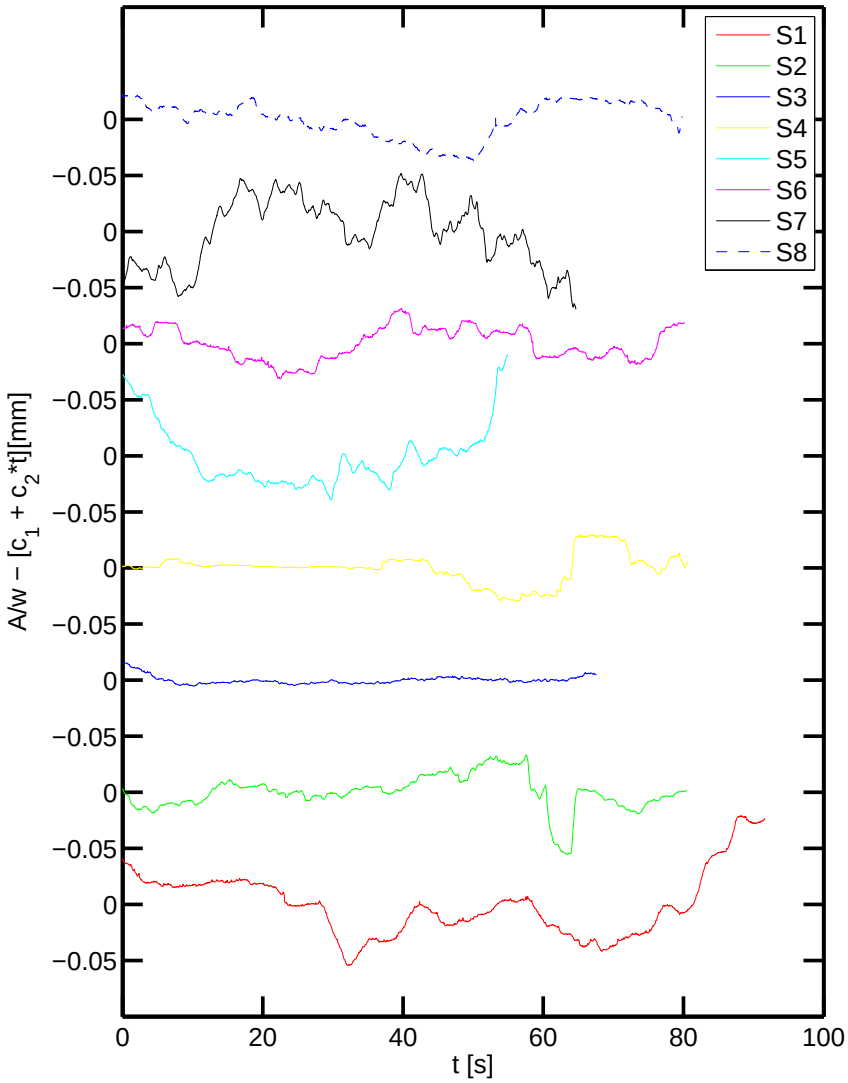

Figure 4.11: The normalised area, A/w, where the mean and the linear trend is subtracted. The standard deviation of the area fluctuations varies much between the experiments.

large Δt.

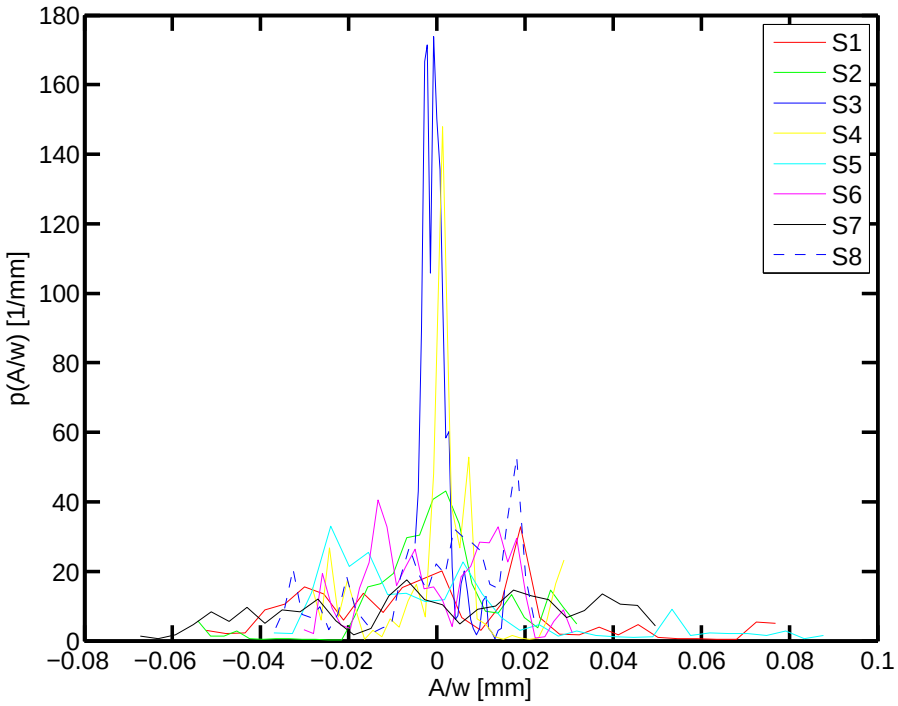

Figure 4.12: Probability density of the normalised area measurement A/w, where linear trend and the mean has been removed from A/w. In other words, it is the probability density calculated from the data plotted in Figure 4.11. The data gives no basis for an underlying general functional form.

When going from small Δt to large Δt there is a small change in the slopes in Figure 4.13. We have used the plot to measure the crossover time, $\Delta t_{crossover}$, where this occur, the result is shown in Table 4.3.

To verify that the power-law scaling exponents, H, are meaningful, we have plotted the probability densities for $\Delta A/w$,where ΔA is calculated for three $\Delta t = 0.1, 0.2, 0, 4$s, before and after rescaling with Δt^H, in Figure 4.14. The rescaling is shown for experiments S1 and S3, which shows the steepest and shallowest slopes in Figure 4.13, with power-law exponents H=0.9 and H=0.75 respectively. This test was performed for all eight experiments and similar data collapses were found. That is, the rescaling collapses data for one experiment at different Δt onto each other. Note that it is the absolute value of area changes, $|\Delta A/w|$, that is plotted in Figure 4.14(c) and Figure 4.14(d). We see no significant difference in the probability distribution of positive and negative area changes. The data collapse of the rescaled prob-

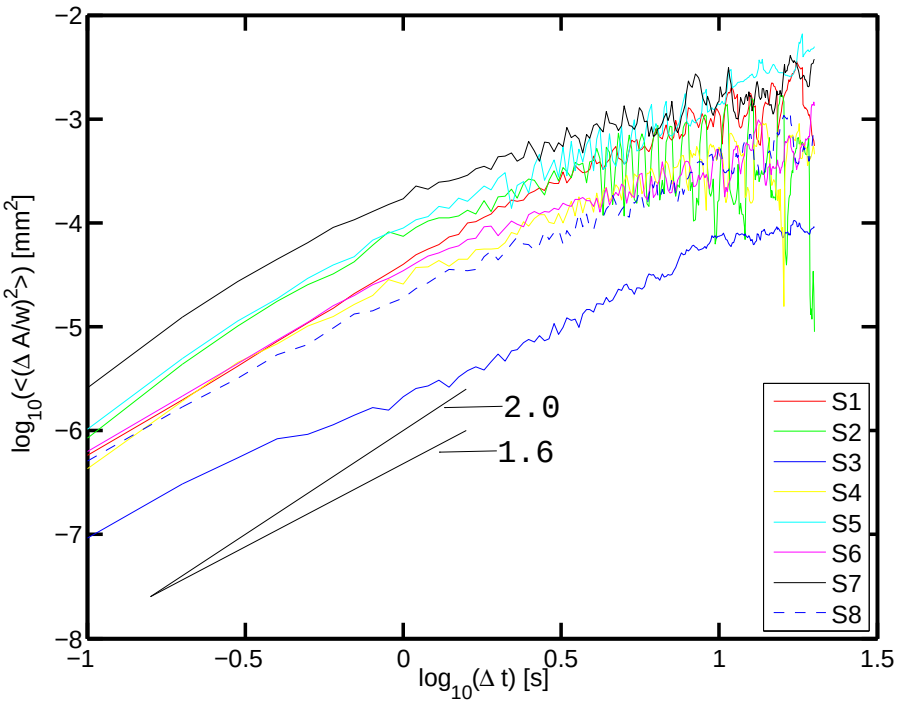

Figure 4.13: Scaling plot showing the average change in area squared ,$< (\Delta A/w)^2 >$ for an $\Delta t = [0.1...20]$ seconds. The two black lines correspond to the smallest and largest slopes in the scaling relation, 1.5 and 1.8 respectively. Note how the slopes fall off with increasing Δt.

ability density strengthens the validity of the scaling relation. The positive and negative slopes in the log-linear plot in Figure 4.14(b) are listed in Table 4.3 for all the eight analysed experiments.

4.5.2 Length of the slip-line

We have analysed how the length of the slip-line evolves during the extrusion process, the technical details regarding the length measurement can be found in section 3.5.4. The time-series of the slip-line length is plotted in Figure 4.15. The large fluctuations in length for experiment S1 and S6 compared to other experiments are explained by the automatic slip-line detection routine. In experiments where the grain boundaries appear very dark, ie. in experiment S1 and S6, the grain boundaries downstream from the slip-line will sometimes be identified as a part of the slip-line. While this can produce

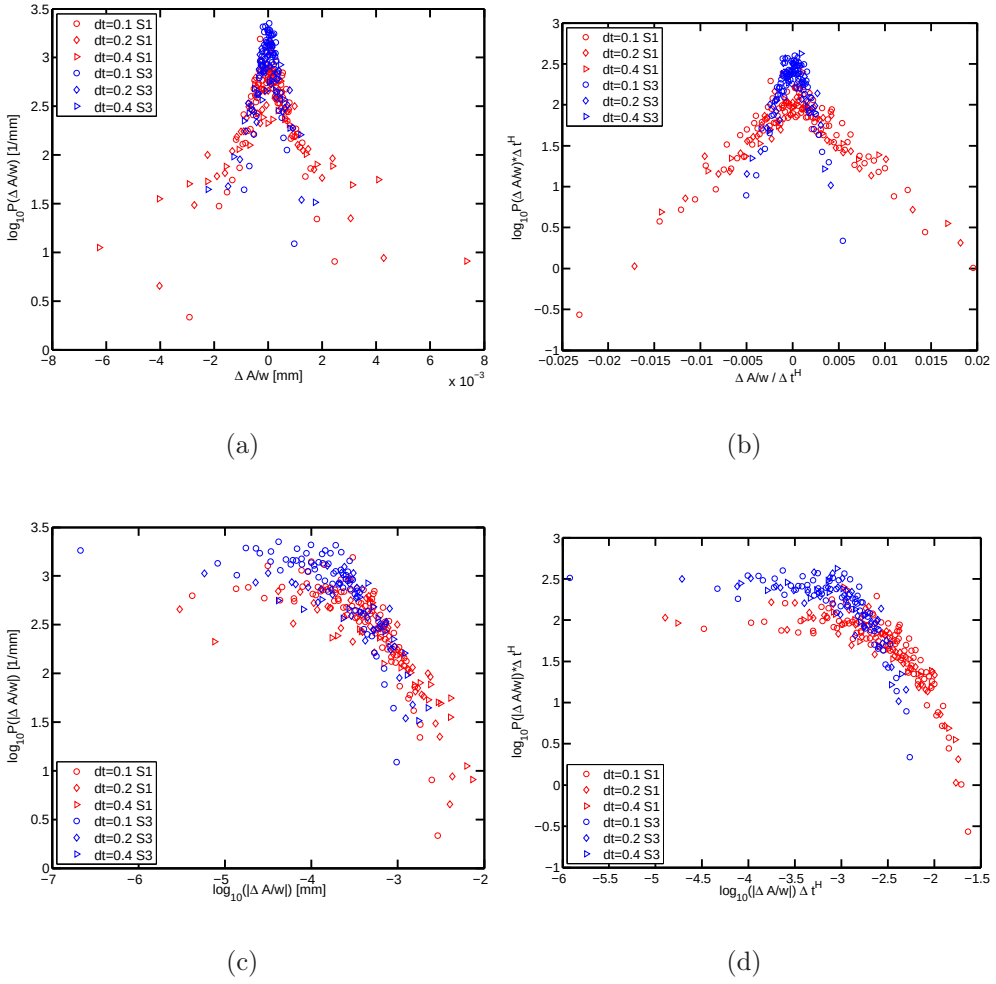

(a) (b)

(c) (d)

Figure 4.14: Log-linear and log-log representation of the probability density for $\Delta A/w$, where where ΔA is calculated for the three $\Delta t = 0.1, 0.2, 0, 4$s. The plots to the left are unscaled while the ones to the right are rescaled with the power-law exponent H. Experiment S1 is rescaled with H=0.9 and experiment S3 with H=0.75. In the log-log plots the absolute value of area, $|\Delta A/w|$, is plotted.

errors in the length measurement, it does not change the area measurement because the faulty identified grain boundaries have very little area.

To further characterise the slip-line we measured how the length of the slip-line, ΔL, scaled with intervals of different width, Δw. The procedure we followed was to divide the slip-line into intervals, systematically varying Δw

normal to the exit velocity and measuring the ΔL within the intervals. This measure provides an estimate of the fractal dimension of the slip-line, that is

$$\Delta L \propto \Delta w^D,$$

where D is the fractal dimension. Figure 4.16 shows this scaling for the eight experiments, where we also have averaged ΔL over all slip-lines in the respective experiments, that is $\sim$2000-3000 slip-lines.

We see that all the experiments follow the same trend. The black line drawn in Figure 4.16 has a slope of 1 which is the euclidean dimension of a line. For increasing Δw the scaling length approaches this slope, however, for small Δw the local D is slightly larger than one. These are characteristic for self-affine geometries.

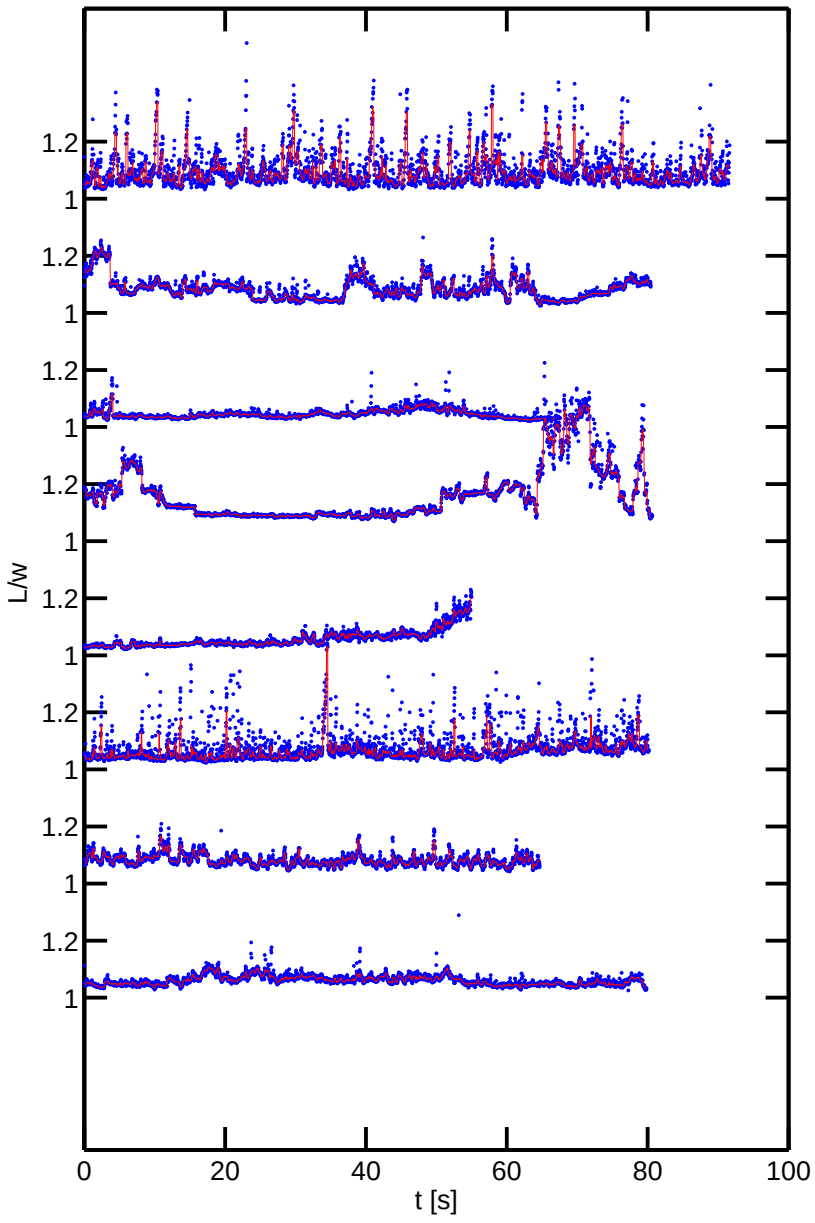

Figure 4.15: The length of the slip-line as a function of time. The top plot is experiment S1, the second from the top is S2 and so on. The length calculated for each image is indicated with blue dots. Because of the scatter in some of the plots, we have median filtered the data (red line). The bin-size used in the filter is 11 measurements.

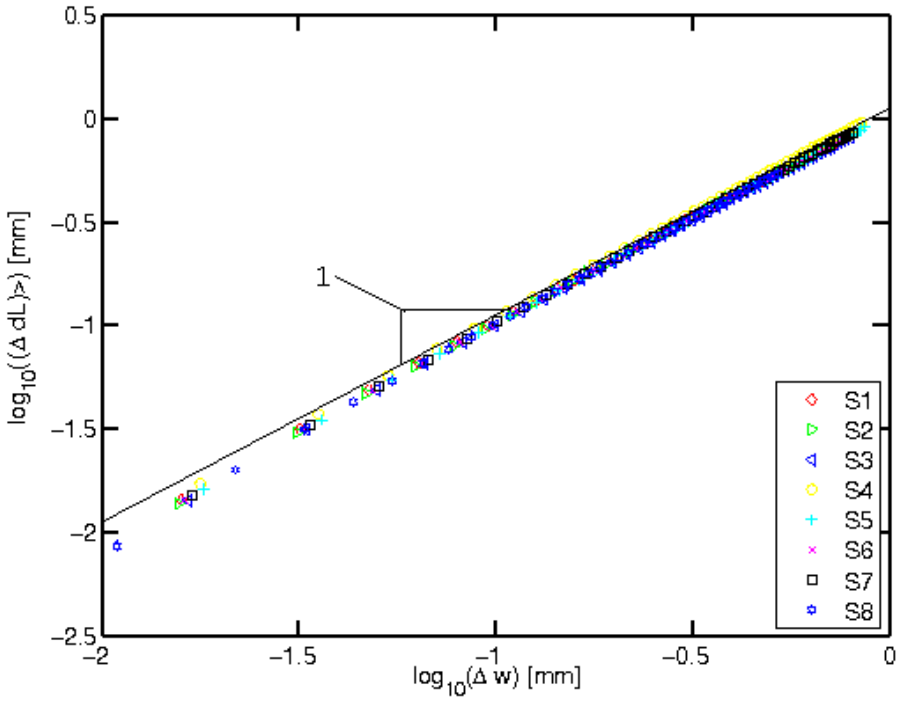

Figure 4.16: Scaling relation of the slip-line length, ΔL, as a function of the width, Δw, it is measured over. The slope of the inserted black line is 1.

4.5.3 Roughness of the slip-line

During extrusion the roughness of the slip-line varies. This can often be attributed to irregularities in the flow that pull the slip-line about 0.1 mm downstream as they pass. Examples of such irregularities are impurities and crystals with different grid orientation from the main flow. We have used the scaling of the standard deviation of the slip-line versus width, Δw, to characterise the roughness of the slip-line. The data is averaged over all slip-lines in the experiment. Section 3.5.1 describes how we determine the standard deviation of the slip-line.

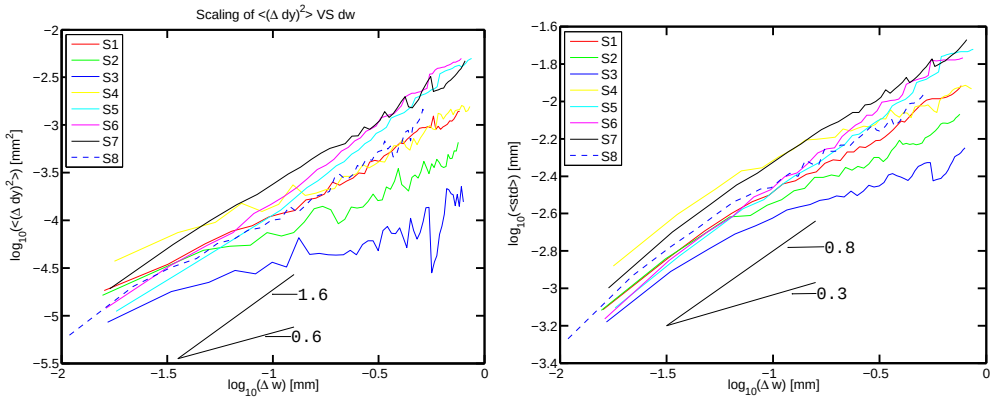

(a) (b)

Figure 4.17: Measures of the roughness of the slip-line. (a) Scaling of the difference in the average slip-line extent in the flow direction, $< dy^2 >$, with width. (b) Scaling of the standard deviation of the slip-line with width. The data is averaged over all slip-lines in the respective experiments, that is ∼2000-3000 slip-lines.

The two measures plotted in Figure 4.17 describe the extent of the slip-line in the flow direction. With the extent, we mean the distance between the point of the slip-line that is furthest downstream and the point being fattest upstream in the die. The mean square extent in the flow direction, $< (\Delta y)^2 >$, as a function of the width is plotted in Figure 4.17(a). The scaling of the mean standard deviation of the slip-line, $< std >$, with w is plotted in Figure 4.17(b). For these two roughness measures, we assume a

scaling relation on the form

$$< (\Delta y)^2 > \propto \Delta w^{2H},$$
$$< std > \propto \Delta w^{H},$$

where H is the Hurst exponent. From the slopes in Figure 4.17 we see that both the scaling relations gives the same estimate for the lower and upper boundary of the Hurst exponent, $H = 0.3$ and $H = 0.8$ respectively. In all the experiments the value of H is in the interval [0.3, 0.8], which means that the slip-line will appear flat for large Δw. This is in agreement with the findings in section that also show that the slip-line is a flat when Δw is large.

We see a change in the slope for the experiments, clearer in some than others, and easiest observed in the scaling of $< std >$, Figure 4.17(b). For small Δw, H is larger than 1/2 ($\sim$0.8). This means that we have persistence, thus an increasing trend in the standard deviation is likely to be followed by an increasing trend in the future and *vice versa*. As Δw increases we see a crossover to a slope smaller than H=1/2, $\sim$0.3, which corresponds to a negatively correlated behaviour. This is likely to be related to the constraints imposed on the slip-line position by the die geometry; for large Δw standard deviation is limited by the curvature, R_c, of the die. For very large Δw the standard deviation of the line will go towards a constant value, corresponding to $H = 0$.

4.5.4 Summary of the scaling measures

This section summarises the statistical measurements we have used to determine any possible trends in the eight analysed experiments, the results are listed in Table 4.3. We have attempted to determine the cutoff length, $\Delta L_{crossover}$, for the scaling of standard deviation based on the plots in and Figure 4.17(b). The same approach has been used to determine $\Delta t_{crossover}$ from the scaling of the area, A/w, with the time, Δt.

The cutoff lengths found from the $< std >$ vs length plots in Figure 4.17(b) is presented in Table 4.3. However, we do not see a relation between the radius of curvature, R_c, and the Δw for which the crossover occurs. This suggests that there are factors other than R_c controlling this scaling behaviour, but is probably also a consequence of the few observations available for the analysis.

Experiment	R_c [mm]	$\Delta w_{crossover}$ [mm]	$\Delta t_{crossover}$ [s]	σ_A [mm]	Decay length [mm^{-1}]
S1	66.1	0.06	4.0	0.0287	-105 110
S6	44.6	0.04	1.8	0.0146	-100 123
S7	44.6	0.13	0.8	0.0304	-33 29
S5	29.1	Straight	0.8	0.0277	-62 54
S3	29.1	0.10	7.9	0.0035	-355 247
S2	24.8	0.05	1.8	0.0157	-114 100
S4	24.8	0.13	7.9	0.0134	-140 207
S8	24.8	0.04	0.8	0.0161	-118 135

Table 4.3: The crossover width,$\Delta w_{crossover}$, and crossover time,$\Delta t_{crossover}$, determined from the scaling behaviour plotted in Figure 4.17(b) and Figure 4.13 respectively. The standard deviation of the area, σ_A, has been determined from the time-series in Figure 4.10. The decay length referes to the slopes in the log-log plot of the probability density in Figure 4.14(b). Note that $\Delta w_{crossover}$ and $\Delta t_{crossover}$ are rough estimates.

4.5.5 Bulk and surface velocities

Surface velocity
In the following will we present an analysis of the surface velocity measure performed to determine the velocity of the extruded material down-stream from the slip-line. We have measured the velocity both in the direction parallel, $v_{\parallel}$, and in the direction perpendicular, $v_{\perp}$, to the exiting flow. The first measure is often referred to as exit velocity in the extrusion literature, therefore, this name is used in the following. The velocity in the direction perpendicular to the exit velocity, $v_{\perp}$, thus parallel with the slip-line, will be referred to as the normal velocity. We determine the surface velocity of the material in a region located immediately on the outlet side of the slip-line. The exit velocity here corresponds to the velocity of the material exiting the die if we assume that the extrusion material exhibits plug flow downstream from the slip-line. The details of this correlation method are described in section 3.4.3. For the velocity measurements presented in this section it is crucial to know the precise time, Δt, between the images. The following analysis is, therefore, only carried out for experiments with an uncertainty less than ± 1 ms, ie. experiments S1, S2, and S3.

The spatial and temporal fluctuations in the surface velocity measured immediately downstream from the slip-line are shown in Figure 4.18. Position=0 in the middle, w/2, of the region in the bearing channel we have measured the velocity for. The average exit and normal velocity in the experiments are; $\bar{v}_{\parallel} = 0.29$mm/s and $\bar{v}_{\perp} = 0.0$mm/s (S1), $\bar{v}_{\parallel} = 0.39$mm/s and $\bar{v}_{\perp} = 0.0$mm/s (S2), and $\bar{v}_{\parallel} = 0.32$mm/s and $\bar{v}_{\perp} = 0.0$mm/s (S3).

We have compared fluctuations in the exit velocity with periodic fluctuations in the hydraulic back-pressure, the respective data-sets are shown in Figure 4.19. The large variations in the pressure do not seem to influence the fluctuations in the flow velocity adversely, nor are the trends in the velocity signals affected by the pressure to any large extent. The periodicity of the pressure signals on the short time scale, $\sim$1-2 seconds, were determined with a discrete Fourier transform of the complete time series, the periods are $T_P = 1.36$ s (S3), $T_P = 1.74$ s (S2), and $T_P = 2.27$ s (s1), see Figure 4.20(b). The amplitude of the fluctuations are ± 0.04 bar in all the experiments. We attempted to extract the characteristic period in the complete exit velocity signals with the discrete Fourier transform, the resulting power-spectrums are shown in Figure 4.20(a). The power-spectrums are not conclusive because of the different wavelengths and trends present in the data-set, and it cannot be used to determine one characteristic wavelength. We have, therefore,

picked out shorter time-series from the fluctuations, where the exit velocity have little trends and are close to monoperiodic, and calculated their discrete Fourier transform. The power-spectrum for the selected parts of the velocity signals and the corresponding pressure is shown in Figure 4.21 together with the exit velocity and pressure signal they are calculated from. The periods corresponding to the largest peaks in the power-spectrum, for period T<5s, for the exit velocity are $T_{\|} = 2.43$ s (S1), $T_{\|} = 1.54$ s (S2), and $T_{\|} = 1.46$ s (S3). The periods for the pressure in this time-interval are $T_P = 2.27$ s (S1), $T_P = 1.70$ s (S2), and $T_P = 1.36$ s (S3). In experiments S1 and S3 the period of the velocity fluctuations, $T_{\|}$, are 7% larger then the pressure period, T_P. In experiment S2 is the T_P 10% larger than $T_{\|}$. Experiment S1 and S3 suggest that one part of the velocity fluctuations are caused by the periodicly varying back-pressure delivered by the pump. However, the descrepancy found between the periods in experiment S2 and the many peaks in Figure 4.20(a) shows that there is other factors, in addition to the back-pressure, that controlles the fluctuations in the extrusion velocity.

The time-series for the normal velocity averaged along the slip-line, $v_{\perp}$, is shown in Figure 4.22. The standard deviation in these measurement are $\sigma_{v_{\perp}} = 0.005$mm/s (S1), $\sigma_{v_{\perp}} = 0.006$mm/s (S2), $\sigma_{v_{\perp}} = 0.006$mm/s (S3). A standard deviation of 0.005 mm/s corresponds to a displacement of 0.1 pixels in the correlation method. This displacement is then averaged the $\sim$400 measurements along the slip-line. We trust the fluctuations in $v_{\perp}$ to be real, and not artifacts generated by the image analysis routine. For the three experiments the average ratio of the standard deviation in normal velocity $\sigma_{v_{\perp}}$ to the mean flow velocity is

$$\frac{\sigma_{v_{\perp}}}{\bar{v}_{\|}} = \frac{(0.05 + 0.06 + 0.06)/3}{(0.39 + 0.29 + 0.32)/3} = 0.017 = 1.7\%. \tag{4.1}$$

This result means that the extruded profile wiggles slightly on its way out of the die. The power-spectrum calculated with the discrete Fourier transform of $v_{\perp}$, do not yield any single characteristic wavelength in this behaviour.

Figure 4.23 shows the time-average of the exit velocity along the slip-line. The large trends in this graph can be trusted to be correct, ie. the difference in velocity from the left to the right side of the studied region of the bearing channel. The small fluctuations in this velocity, however, correspond to displacements much smaller than 0.1 pixel, and are therefore likely to be much influenced by measurement errors. The deviation shown in the trends in Figure 4.23 between the time-averaged exit velocity from the pure exit velocity, $\bar{v}_{\|}$, is in the order of 1-3% across the $\sim$ 1.2 mm of the

bearing channel. In the experiments we have observed several times observed that the profile can exit the die with a small angle, therefore, a difference in the average exit velocity across the bearing channel was expected.

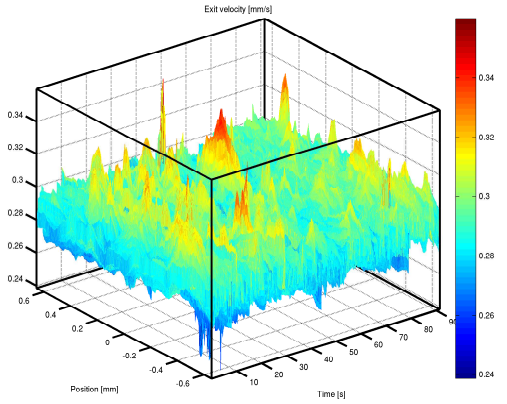

(a) Experiment S1

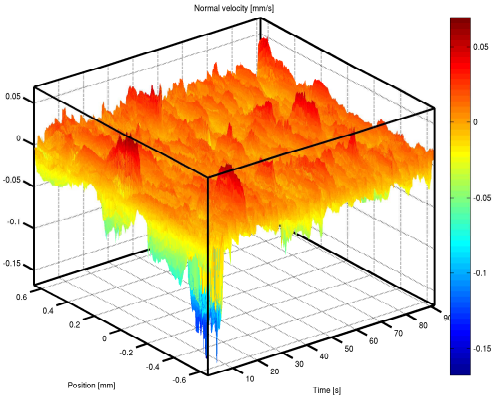

(b) Experiment S1

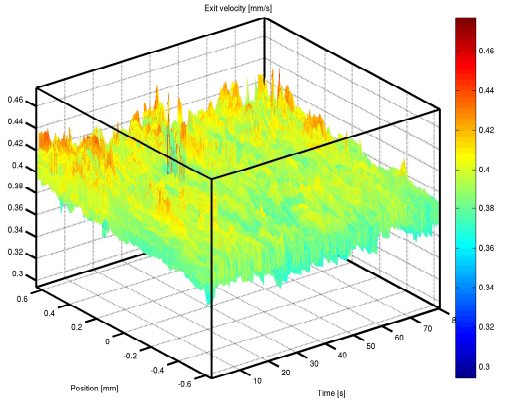

(c) Experiment S2

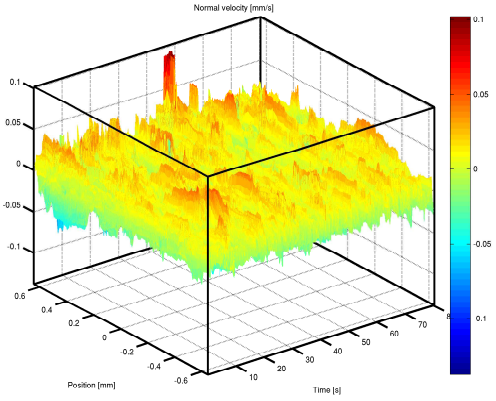

(d) Experiment S2

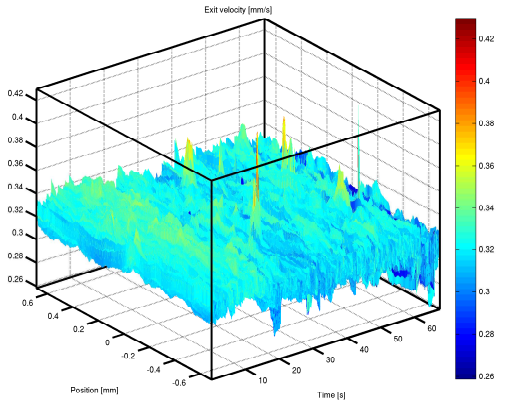

(e) Experiment S3

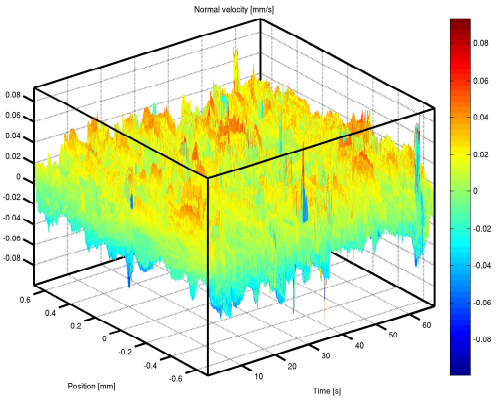

(f) Experiment S3

Figure 4.18: The exit velocity,$v_{\parallel}$, and normal velocity, $v_{\perp}$, along the slip-line as a function of time and position.

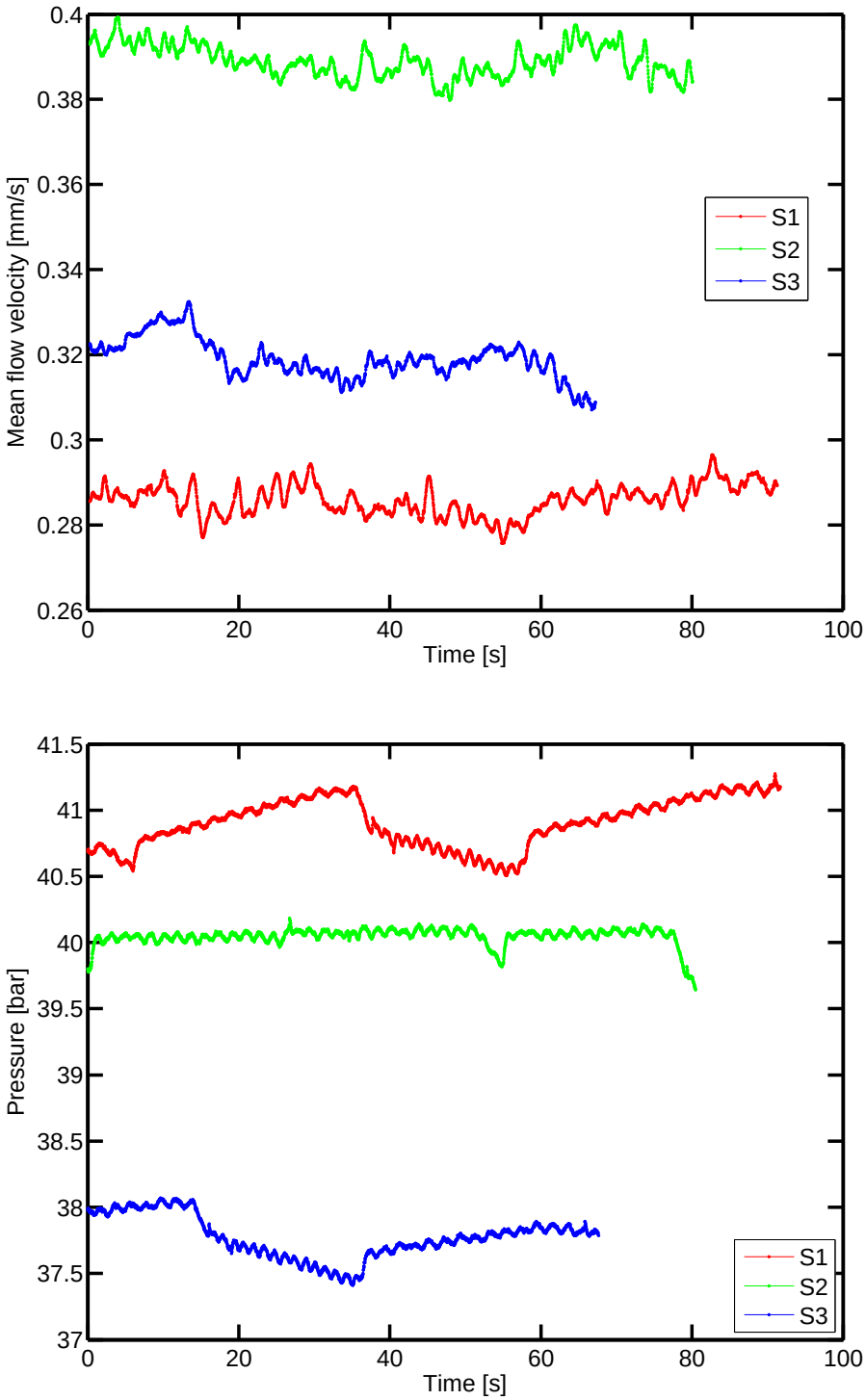

Figure 4.19: (a)The temporal evolution of the average exit velocity. The average is calculated in the direction along the slip-line. For clarity the data have been filtered with a mean-filter with a width of 11 measurements. The velocity is averaged along the slip-line for every velocity measurement. (b) The back-pressure measured during the extrusion. Note the periodicity in the pressure signals.

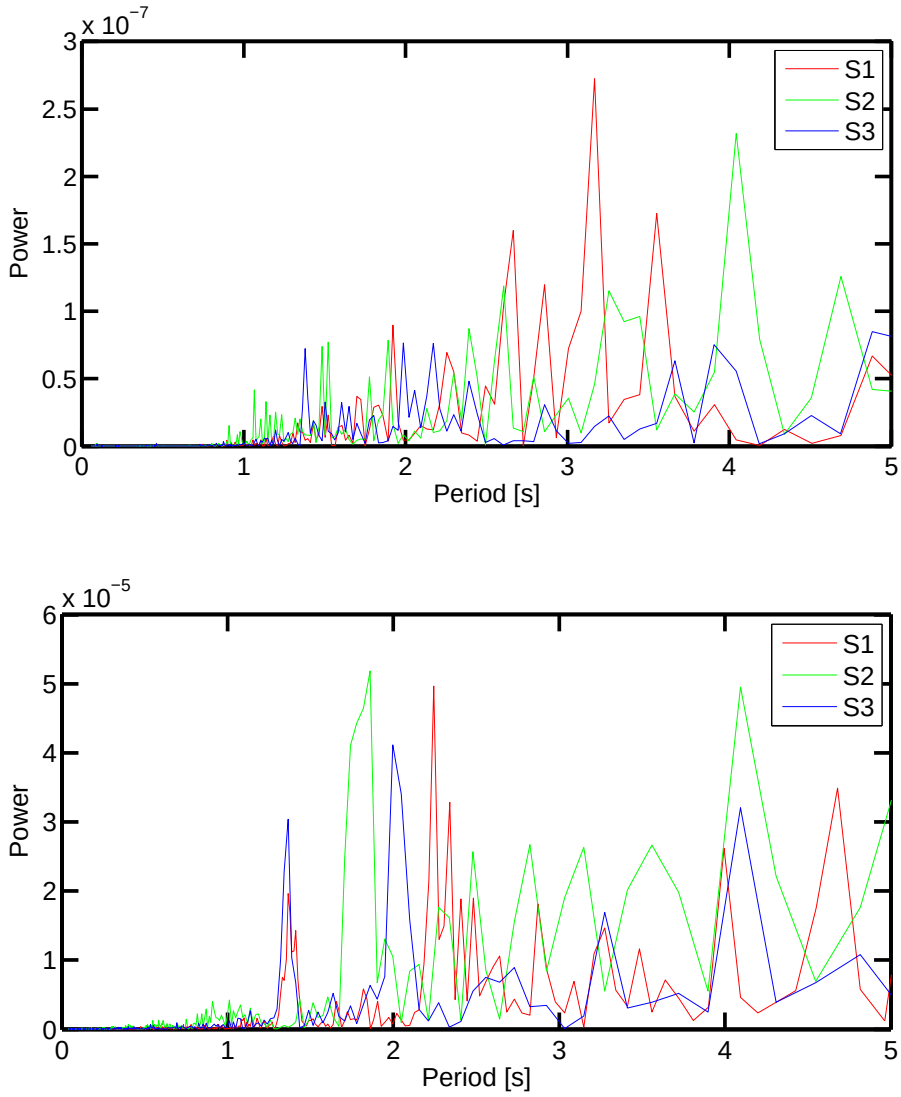

Figure 4.20: **Top** Power-spectrum for the average exit velocity plotted in Figure 4.19(a). We were unable to extract any characteristic period in the exit velocity fluctuations based on this discrete Fourier transform. **Bottom** Power spectrum for the back-pressure during the extrusion. The peaks corresponds to the periods; T=1.36 and T=2.3 seconds for S1, T=1.86 seconds for S2, and T=1.36 and T=2 seconds for S3.

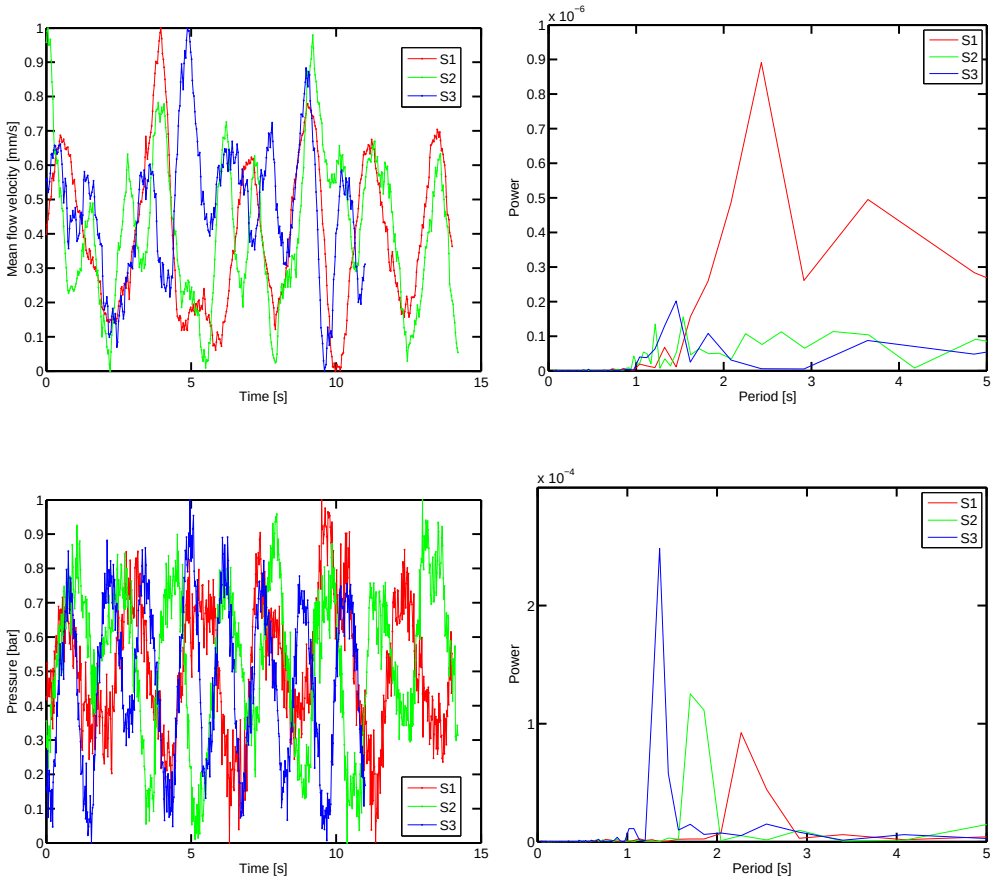

Figure 4.21: **Left:** The mean exit velocity and the pressure for a selected time-interval more suited for a Fourier transform than the complete time series. The data have been rescaled to lie in the interval [0,1]. **Right:** The Fourier transform of the velocity and pressure signal, top and bottom figure respectively.

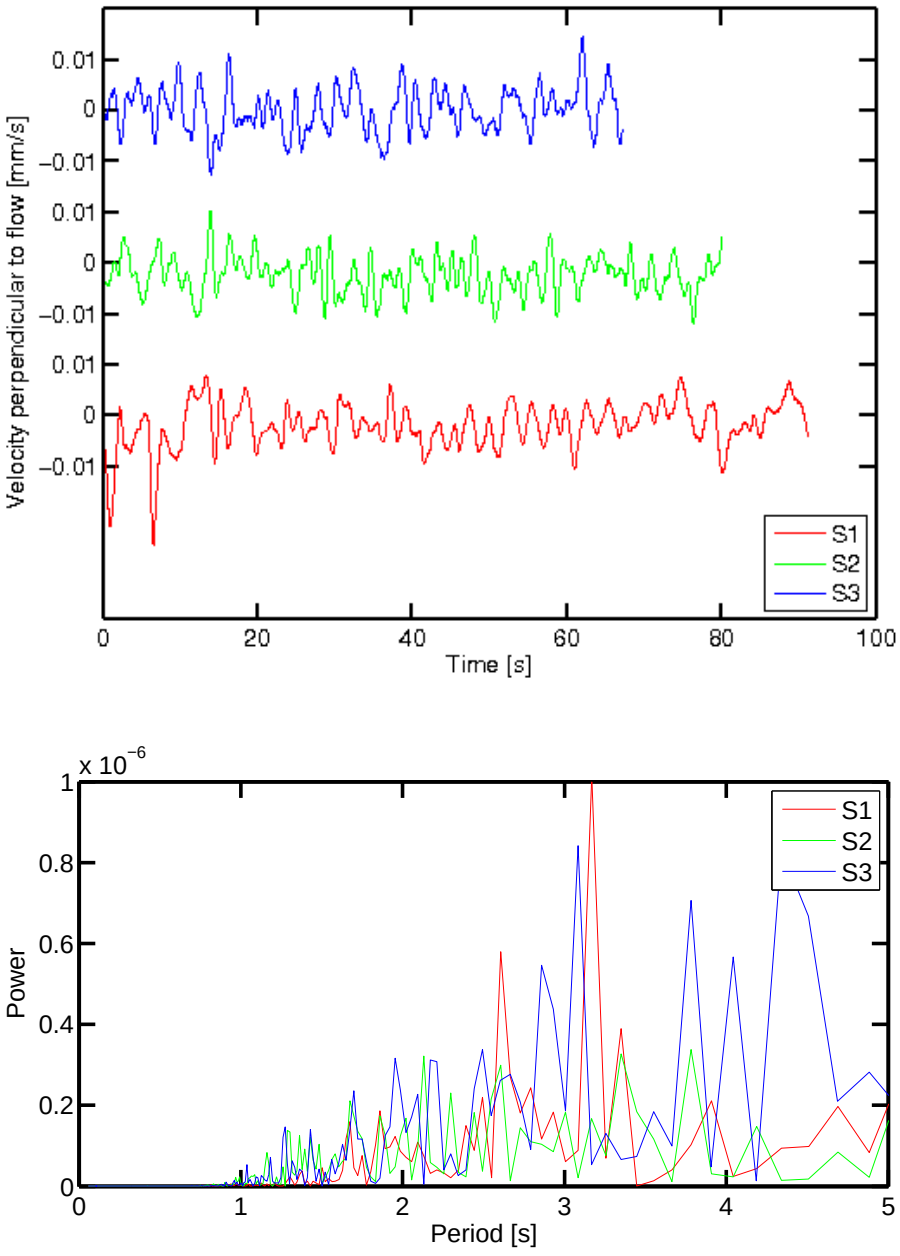

Figure 4.22: (a) The temporal evolution of the average normal velocity, $v_\perp$. The velocity is averaged in the direction along the slip-line. We have used a mean filter, bin-width 11 measurements, on the data-set for clarity. (b) The discrete Fourier transform of $v_\perp$. No peaks stand out in this spectrum.

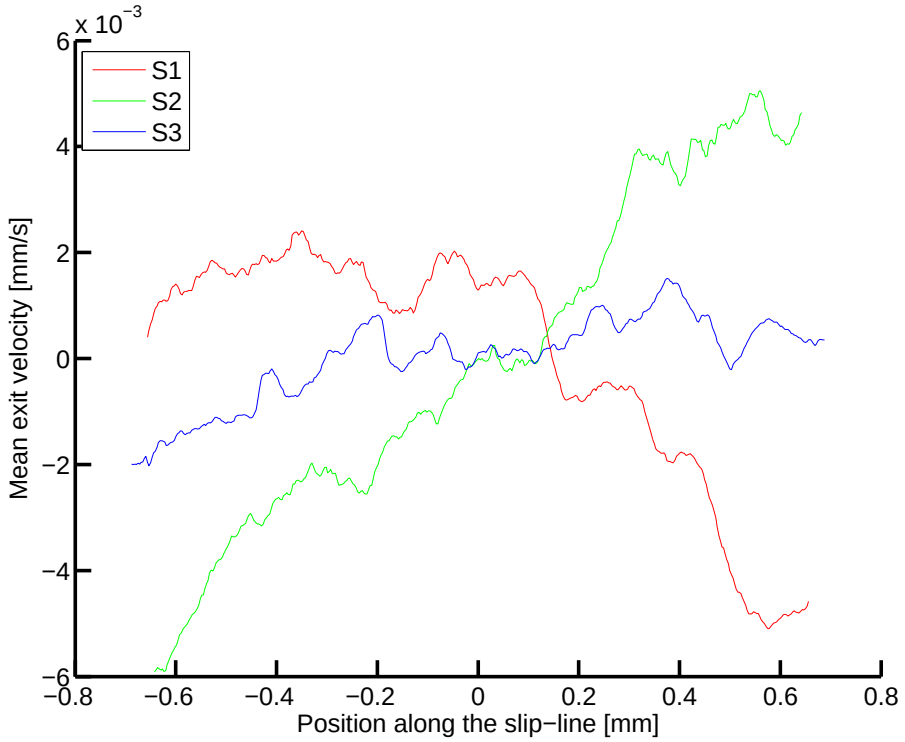

Figure 4.23: The time average of the exit velocity, $v_{\|}$, plotted along the slip-line. The centre of the region were we have mapped the slip-line corresponds to position=0, the end of the measurements are in $0 \pm w/2$. The mean velocities $\bar{v}_{\|} = 0.2859$ mm/s(S1), $\bar{v}_{\|} = 0.3891$ mm/s (S2), and $\bar{v}_{\|} = 0.3189$ mm/s (S3) are subtracted from the respective plots.

Bulk flow velocity

The bulk velocity profile has been determined for the experiments S9-B and S10-B. The curvature in these dies are $R_c = 8.0$ mm and $R_c = 66.1$ respectively. This measurement is done from the die inlet down to the middle of the die and is based on the movement of tracer particles in a plane inside the bulk flow. The details of this measurement are described in 3.4.3.

Figure 4.24 and Figure 4.24 present the velocity profile for Camphene flowing in dies with radius of curvature 66.1 mm and 8.0 mm respectively. The images to the left show the velocity in the main extrusion direction, this is referred to as the bulk flow velocity in the following. The images to the right show the velocity perpendicular to the flow velocity, henceforth called the bulk normal velocity. The two top images in the figures is for the die inlet, the two images beneath are from one image frame further downstream and so on. The velocity profile starts 0.5 mm from the inlet and extent about 3.3 mm (Figure 4.25) and 5.5 mm (Figure 4.24) downstream, The total length of the die is 8 mm. There are an overlap of 0.1 mm between the images.

The die walls are drawn in black in the scalar plots. The position of the walls is determined by comparing the plots with the correlated optical images. The white area in the top right image is because there in this region have been too few tracer particles in focus to obtain a good correlation. Note that the sidewalls in the images are the curved bearing surfaces, therefore, we expect an acceleration as we approach the narrower middle of the die. However, the pressure can vary while we move the camera between the regions. Therefore should the attention be directed not so much on the absolute velocity as the velocity profile.

In Figure 4.24 can we see that the bulk flow velocity at the inlet, Figure 4.24(a), has a more parabolic velocity profile, that over the next few millimeters changes to a more plug-like profile.

In the middle of the die, Figure 4.24(e), the velocity profile appear completely flat. The noise at the left bearing surface is caused by a film of glue on the wall we are filming through and that the profile is leaving the wall in this region. The flat profile suggest that we are in the plug-flow regime, which mean there no longer are stick-boundary conditions. The optical images of the channel at this point show that the material start slipping from the right wall where the 0.4 mm tick is. The images are, unfortunately, blurred to much at this point in the channel that we can resolve the flow at the walls good enough to see the slip-point. Figure 4.24(g) show the velocity profile even further down stream.

The velocity profile perpendicular to the main flow direction, in Figure 4.24(b), has a funnel shape at the inlet, because the material is pushed towards the middle of the narrowing channel. As we approaches the middle, the profile of the normal bulk velocity this tendency is weakened, and finally vanishes in Figure 4.24(h). The flat normal bulk velocity profile indicates that the walls no longer pushes on the profile, as is the case when we have plug-flow. The non-vanishing velocity in this direction because the CCD chip in the camera not is perfectly aligned with the main flow direction.

In Figure 4.24 the radius of curvature, R_c, is of the die is only 12% of that in the experiment described above. The flow velocity profile starts out parabolic in Figure 4.25(a) and appears allmost flat in the bottom of Figure 4.25(c). Right downstream of the middle of the die, by the 0.4 mm tick in Figure 4.25(e) it looks as if the material no longer stick at the wall, and we have pure plug-flow. This is supported by the flat profile for the flow in the normal direction aswell.

Through these experiments have we been able to see the transition from a parabolic flow profile to Couette-like flow, which is characteristic for non-Newtonian fluid flow. And in the area where the slip-line is located, we have observed how this almost flat velocity profile turns into the entirely flat one characterising pure plug-flow.

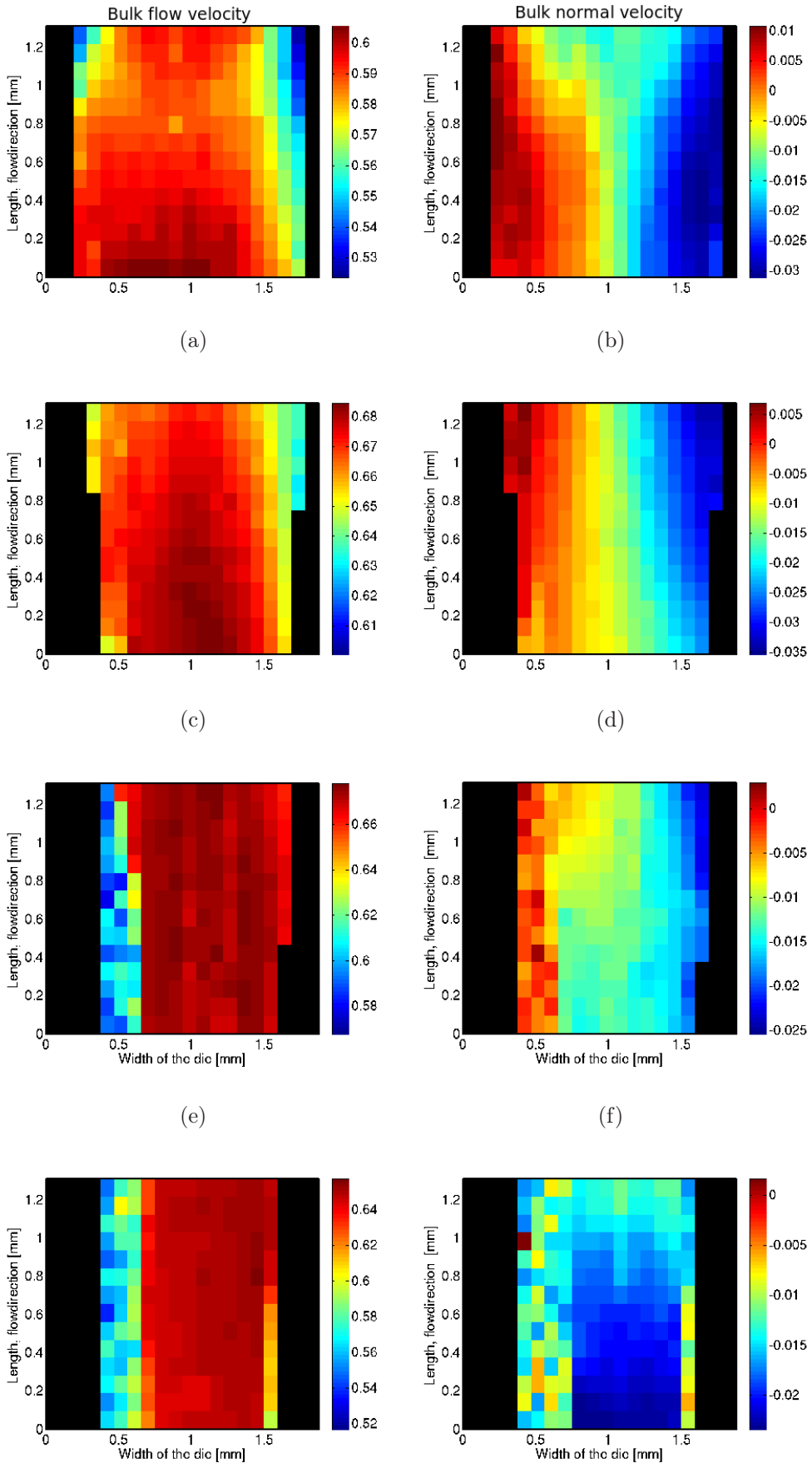

Figure 4.24: The bulk velocity profile in [mm/s] for experiment S10-B where $R_c =$

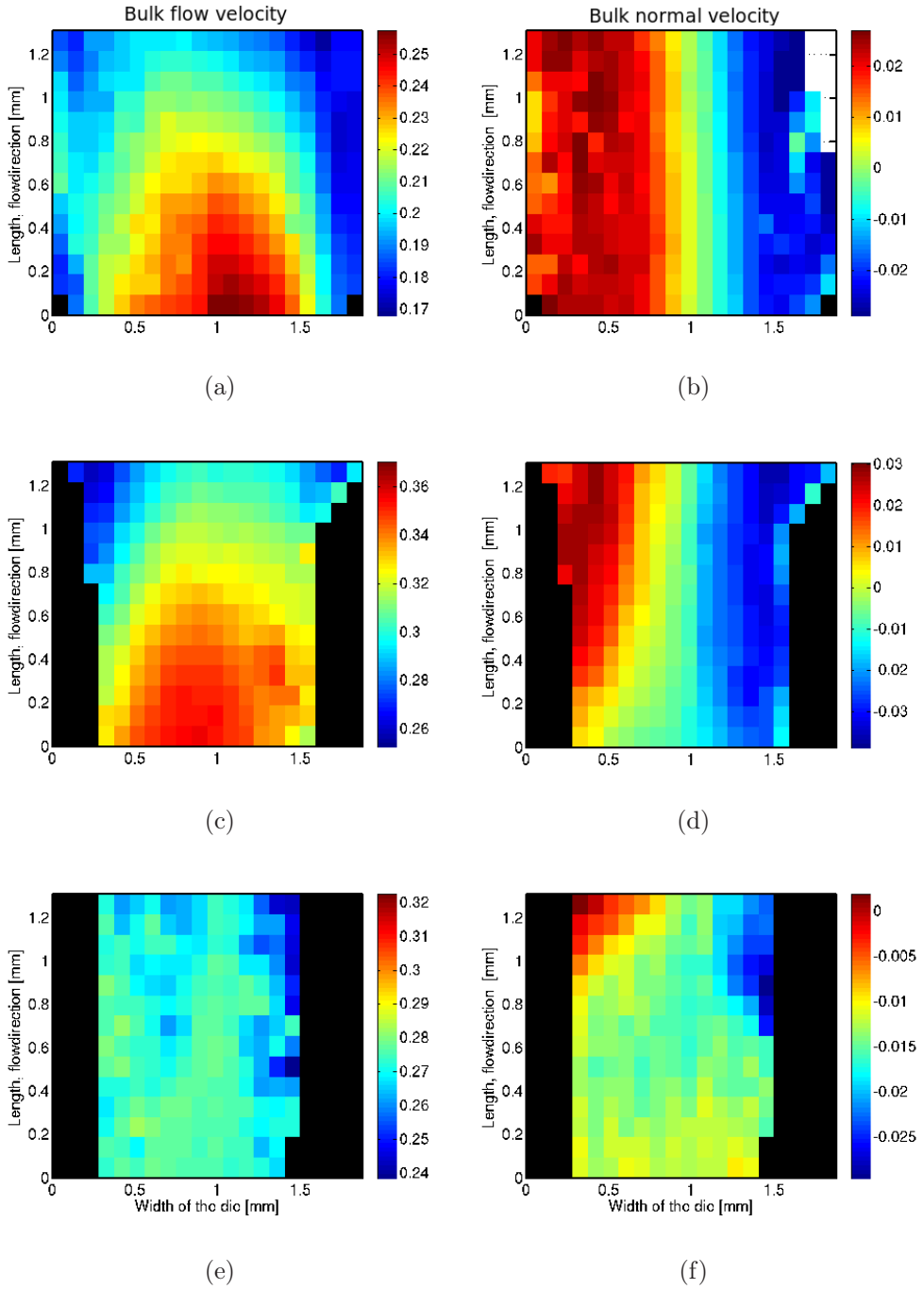

Figure 4.25: The bulk velocity profile in [mm/s] for experiment S9-B where R_c = 8.0mm.

Chapter 5

Discussion and Conclusion

We have studied the extrusion process by characterising the behaviour of the transition from stick to slip regime inside the die and analysing the velocity field. We chose to study the effect by systematically varying the radius of curvature, R_c,of the bearing walls in the dies. When using curved dies we know the geometrical constraints in the die better than if we tried to use parallel walls. This is because parallelity is very difficult to control in an experimental setting, especially with the die casting techniques available to us at this time. Furthermore, elastic deflection of the bearing walls during extrusion will always induce a curvature in the die.

There is an endless number of phenomena and measures, qualitative and quantitative that one may delve into when opening a new research avenue like this. The phenomenology has often seemed too rich! We have therefore been forced to make choices on what to spend time on analysing and only *a posteriori* known if we chose a good avenue. Many of the results point to future research possibilities.

5.1 Three different regimes

The extrusion experiments can be divided into three main categories where the slip-line appear very different;**i)** as a clear border between the stick and slip region, **ii)** as a very rough border between the regions, **iii)** or not present at all. We did our best to design the experiment in a way that favoured the clear boundary, **i**, since our analysis tools was developed with this scenario in mind. However, often the slip-line did not appear at all,**iii**. We believe this can be explained by how gravity affected our experimental setup. The material is pulled towards the bearing surface we observe, and the result is

that the slip-line only appears at the die outlet. However, gravity can only be partially responsible for this problem because we also have the two other categories of experiments where this does not happen. We have suggested variation in the geometry of the die as a second contributor to the problem. The category **ii)** where the slip-line appears too rough to be analysed with our automatic methods is very interesting. In these experiments we observed regions dominated by friction between the newly formed extrusion profile and the bearing surface. There was a clear adhesive layer present on the die surfaces and the presence Newton rings downstream indicated that the profile and the bearing surface are separated but only by a ∼10-100 nm. We know from the extrusion industry that there is much interaction between the extruded material and the die. Out of the three categories we observed, this is the one that can accommodate the amount of friction that is being reported in aluminium extrusion. This was also the most frequent category we encountered. Experiments that started out as category **i** would often evolve into having an extremely rough line and almost undefined slip-stick transition. Rough or reused dies are optimal conditions for observing category **ii)** behaviour.

5.2 Qualitative findings

Top bottom slip-line instability is peculiar, interesting and possibly important in extrusion with long bearing surfaces. This seems like an interesting problem for future work. We have observed the presence of an adhesive layer of varying thickness on the bearing surface in many in the experiments. It may very well be present in all the experiments because it is very difficult to observe when thin. During the experiments this layer often become thicker, which mechanisms controlling the growth of the layer is not understood. It is also well known that in solid friction there is always material transfer between the contacting materials. We have seen this leading to material being picked up from the flow and deposited on the bearing surface. The transparency of the die and extruding material lends this system to further direct observation of this feature that other authors have found to be important in Aluminium extrusion. We have observed micro-hills that sticks to the bearing surface and make groves in the material that flows past. Local fluctuations of slip line position is driven by disorder in the extruded polycrystalline material. Stabilization is assumed to be caused by the die land curvature, elastic interactions and surface tension.

5.3 Quantitative findings

In the optically simple category **i** experiments we have found a number of interesting results.

The mean slip line position fluctuates and drifts slightly during experiments. At short times, typically <1s, the motion is persistent, characterized by a Hurst exponent of 0.75-0.9. At longer times, typically 5-10s, motion is uncorrelated.

Using the fluctuation scaling we may obtain data collapse of area change distributions of the slip line for different area time intervals. This exponential distribution yields a form of time dependent decay/correlation length of area changes.

Using the length of the slip line, the slip line is measured to be close to 1-dimensional. Only at the short length scales, $< 100\mu m$, is the slip line dimension slightly larger than 1.

The width measure of the roughness of the slip line on the other hand shows a crossover from persistent to antipersistent behaviour at length scales of 40-130 micrometers. No trend in crossover length with varying radius of curvature, R_c, is found. This means that the crossover length is dominated by variation in disorder between experiments, not by the die land surface curvature.

Correlation of back-pressure and exit velocity shows that some of the periodic pressure variations are detected in the exit velocity. Large pressure fluctuations, however cannot be seen to directly influence the exit velocity. This is an important result that demonstrates that the extrusion dynamics are mostly influenced by disorder in the material and there is only a weak coupling to the back-pressure. In fact, the coupling is so weak that it is barely detectable using the equivalent of a Lock-in amplifier technique used to measure small signals in noisy environments. This confirms that the system is, as we hoped and expected, dominated by disorder in the material that the fracture tip (slip line) is moving into, in the same manner as in the Plexiglas fracturing experiments of the Måløy group.

In addition to the slow top-bottom instability, with a time scale of 100 s, the careful measurements of extrusion velocity normal to the main flow direction revealed a wiggling behaviour of the exiting extrudate on the timescale of 2-5 seconds. These instabilities are possibly important in aluminium extrusion and might well be studied further.

Development of Couette-like flow profile to plug flow has been demonstrated as the material is approaching the slip line. More careful analysis at the die wall must be performed to obtain the details of the evolution. There, unfortunately, was no time for this.

The large scale behaviour of the slip-line is largely dependent of the geometry of the die. However, at the present time, we have been unsuccessful in correlating any of the statistical measures we have done on the slip-line to the radius of curvature, R_c. This suggest that there are other factors that controls this behavior. Another scenario is that the very varying experimental conditions we have encountered during the work conceal the trends we are looking for. This is quite possible, considering we only have analysed eight experiments.

5.4 Future work

Three of the eight experiments quantitatively analysed in this report have been made with our current experimental setup that gives an uncertainty in the image acquisition time $\sigma = \pm 0.7ms$, the other experiments have an uncertainty of the order $\sigma \pm 10 - 15ms$. With higher time resolution we could investigate the scaling behaviour of the statistical measures for shorter Δt. The current lower limit we use is 0.1 s. This will tell us more about the persistence and antipersistence we have found in our data A camera with higher resolution whould allow the study of the slip-lines self-affinity more thoroughly.

Furthermore we could improve the statistic quality of the measurements by running the experiments for a longer time. Today our image-reading routine limits us to read no more than 3200 frames ($\sim$90 s). A larger Δt would enable us to verify that the Hurst exponent in the scaling of the standard deviation of ΔA approaches zero. The methods used to detect crossover lengths should be improved, ie. by the usage of fitting functions instead of simply reading them directly from the plots.

To avoid the frequent occurrence of category **i** experiments, a more sophisticated die casting process should be implemented in the future. We have experienced that the geometrical tolerances are smaller than those we can meet with our glued Plexiglas dies. By making the dies from a tougher material than Plexiglas, for instance glass, we could use stronger detergents and mechanical means to clean the dies without damaging the bearing surfaces. The dies used in the experiments in this work often had to be replaced after 1-2 presses because of cracks, dirt, and surface damages. This introduces more die changes, ie variations, in the experimental programme.

In this study we used curved bearing surfaces in the extrusion dies. This geometry guaranteed that the extruded materials internal shear stress ex-

ceeded the critical friction shear stress τ_c towards the outlet, because the bearing channel is opening up. Thus, the design of the bearing channel to a large extent prescribes the location of the transition from stick to slip boundary conditions. We, therefore, propose to use dies that have parallel or slightly choked bearing channels to study the slip-line. This way the balance between the internal strain-rate of the material, $\bar{\epsilon}$, and the frictional stress, τ_c, can be studied without the complications imposed by curved bearing surfaces. Furthermore, the length of the bearing channel can be varied, to study the effect of sliding friction on the behaviour on the slip-line dynamic.

The effect of gravity in our experiments will be considerably reduced, and certainly more symmetric, by changing the orientation of the extrusion press from horizontal to vertical, ie. extruding the profile downwards. Another possibility is to install a conveyor-belt that the exiting profile can roll out on, similar to what is used in aluminium extrusion.

Appendix A

Derivations omitted in the main text

A.1 Euler-Lagrange transformation

Calculating the Euler-Lagrange Functions

The following work has been preformed to determine the associated Euler-Lagrange equation for $F(c_1, c_2, \phi)$. This expression is used in the image analysis tool that extract the slip-line coordinates from the experiment images automatically. For simplicity we regard c_1 and c_2 as constants as we minimise F_h

$$\begin{aligned} F_h(c_1, c_2, \phi) = \quad & \nu \int_{u_0} H_h(\phi(x,y))\ dxdy \\ & +\mu \int_{u_0} \delta_h(x,y) \nabla\phi(x,y)\ dxdy \\ & +\lambda_1 \int_{u_0} (u_0(x,y) - c_1)^2 H_h(\phi(x,y))\ dxdy \\ & +\lambda_2 \int_{u_0} (u_0(x,y) - c_2)^2 (1 - H_h(\phi(x,y)))\ dxdy. \end{aligned} \tag{A.1}$$

Let us do the transformation term by term for the RHS (denoting them I_ν,I_μ,$I_{\lambda 1}$ and $I_{\lambda 2}$), starting with the expression for the area inside C.

$$I_\nu = \nu \int_{u_0} H_h(\phi(x,y))\ dxdy \tag{A.2}$$

We define $\tilde{\phi}$ by

$$\tilde{\phi}(x,y) = \phi(x,y) + \epsilon\eta(x,y),$$

where ϕ is the stationary curve (the extremal minimising the energy contribution from this term), ϵ the parameter to be varied and η an arbitrary function with continuous derivatives that perturbate ϕ on u_0. Now we substitute ϕ in Equation A.2 by $\tilde{\phi}$ and Taylor expand

$$\begin{aligned} I_\nu(\epsilon) &= \nu \int_{u_0} H_h(\phi + \epsilon\eta)\ dxdy \\ I_\nu(\epsilon) &= \nu \int_{u_0} \left(H_h(\phi) + \frac{\partial H_h}{\partial \phi}\epsilon\eta + 0(\epsilon^2) \right)\ dxdy \\ I_\nu(\epsilon) &= \nu \int_{u_0} H_h(\phi) dxdy + \nu \int_{u_0} \frac{\partial H_h}{\partial \phi}\epsilon\eta\ dxdy \end{aligned}$$

We can omit the higher order terms in the Taylor series because we are evaluating the integral I_ν when $\epsilon = 0$, ie. $\tilde{\phi} = \phi$. Differentiating the integral with respect to ϵ at $\epsilon = 0$, and making $\partial I_\nu / \partial \epsilon = 0$ gives the extremal value.

$$\frac{\partial I_\nu(\epsilon)}{\partial \epsilon}|_{\epsilon=0} = \nu \int_{u_0} \frac{\partial H_h(\phi)}{\partial \phi}\eta\ dxdy = 0$$

For the above to be true for all functions, it must be that

$$\nu \frac{\partial H_h(\phi)}{\partial \phi} = 0, \tag{A.3}$$

because η is an arbitrary function. If this were not so, one could choose η so that the integral would have a positive value. Equation A.3 can finally be written as

$$\nu \delta_h(\phi) = 0, \tag{A.4}$$

This is the expression minimising the area terms' contribution to the energy functional F_h.

With the same technique, we find the Euler-Lagrange equation for the second term on the RHS in Equation A.1, the length of C. Finding the extremal for this expression is slightly more complicated, but that should not intimidate us.

$$I_\mu = \mu \int u_0 \delta_h(\phi) |\nabla \phi|\ dxdy \tag{A.5}$$

Again we define

$$\tilde{\phi}(x, y) = \phi(x, y) + \epsilon\eta(x, y),$$

substituting this into Equation A.5 gives

$$\begin{aligned} I_\mu &= \mu \int u_0 \delta_h(\tilde{\phi}) |\nabla \tilde{\phi}|\ dxdy \qquad (A.6) \\ &= \mu \int u_0 \delta_h(\phi + \epsilon\eta) |\nabla(\phi + \epsilon\eta)|\ dxdy \end{aligned}$$

Taylor expanding the factors in Equation A.6 yields

$$\delta_h(\phi + \epsilon\eta) = \delta_h(\phi) + \frac{\partial \delta_h}{\partial \phi}\epsilon\eta$$

for the Delta function. And for $|\nabla\phi|$

$$\begin{aligned} |\nabla(\phi + \epsilon\eta)| &= |\nabla\phi + \epsilon\nabla\eta| = \sqrt{(\nabla\phi + \epsilon\nabla\eta)^2} \\ &= \sqrt{(\nabla\phi)^2 + 2\epsilon(\nabla\phi)\cdot(\nabla\eta) + \epsilon^2(\nabla\phi)^2} \\ &= \sqrt{(\nabla\phi)^2} + \frac{1}{2}\frac{2\epsilon(\nabla\phi)\cdot(\nabla\eta)}{sqrt(\nabla\phi)^2} \\ &= |\nabla\phi| + \epsilon\frac{\nabla\phi}{|\nabla\phi|}\nabla\eta, \end{aligned}$$

where the 2^{nd} order terms of ϵ have been discarded. Rewriting Equation A.6 gives (discarding all 2^{nd} order terms of ϵ)

$$\begin{aligned} I_\mu(\epsilon) = \quad & \mu\int_{u_o}\left(\delta_h + \frac{\partial\delta_h}{\partial\phi}\epsilon\eta\right)\left(|\nabla\phi| + \epsilon\frac{\nabla\phi}{|\nabla\phi|}\nabla\eta\right)dxdy \qquad (A.7) \\ = \quad & \int_{u_o}\delta_h|\nabla\phi|\ dxdy + \epsilon\int_{u_o}\delta_h\frac{\nabla\phi}{|\nabla\phi|}\nabla\eta\ dxdy + \epsilon\int_{u_o}\frac{\partial\delta_h}{\partial\phi}|\nabla\phi|\eta\ dxdy \\ = \quad & \int_{u_o}\delta_h(\phi)|\nabla\phi|\ dxdy + \epsilon\int_{u_o}\delta_h\frac{\nabla\phi}{|\nabla\phi|}\nabla\eta\ dxdy + \epsilon\int_{u_o}\nabla\delta_h\frac{\nabla\phi}{|\nabla\phi|}\eta\ dxdy \end{aligned}$$

Let us now set

$$f = \delta_h \ \ and \ \ \bar{g} = \frac{\nabla\phi}{|\nabla\phi|}\eta.$$

We can then rewrite the last term in Equation A.7 using

$$\begin{aligned} \nabla(f\bar{g}) = \quad & (\nabla f)\bar{g} + f(\nabla\bar{g}) \qquad (A.8) \\ \int_{u_0}\nabla(f\bar{g})\ dxdy = \quad & \int_{u_0}(\nabla f)\bar{g}\ dxdy + \int_{u_0} f(\nabla\bar{g})\ dxdy \\ \int_s(f\bar{g})\cdot\bar{n}dS = \quad & \int_{u_0}(\nabla f)\bar{g}\ dxdy + \int_{u_0} f(\nabla\bar{g})\ dxdy \end{aligned}$$

where Gauss' divergence theorem takes us from integrating over the whole image u_0 to just integrating over the boundary S of the image.

$$\epsilon\int_{u_o}\nabla\delta_h\frac{\nabla\phi}{|\nabla\phi|}\eta\ dxdy = \epsilon\int_s\delta_h\frac{\nabla\phi}{|\nabla\phi|}\eta\bar{n}\ dS - \epsilon\int_{u_o}\delta_h\nabla\cdot\left(\frac{\nabla\phi}{|\nabla\phi|}\eta\right)\ dxdy.$$

Integration by parts of the last term changes the expression to

$$\begin{aligned}\epsilon \int_{u_o} \nabla\delta_h \frac{\nabla\phi}{|\nabla\phi|}\eta \; dxdy = \quad & \epsilon \int_s \delta_h \frac{\nabla\phi}{|\nabla\phi|}\eta\bar{n} \; dS \\ & -\epsilon \int_{u_o} \delta_h \left(\nabla \cdot \left(\frac{\nabla\phi}{|\nabla\phi|}\right)\right)\eta \; dxdy \\ & -\epsilon \int_{u_o} \delta_h \left(\frac{\nabla\phi}{|\nabla\phi|}\right)\nabla\eta \; dxdy.\end{aligned} \tag{A.9}$$

If we insert this result into Equation A.7, the two terms will cancel each other out and we are left with

$$I_\mu(\epsilon) = \int_{u_o} \delta_h |\nabla\phi| \; dxdy + \epsilon \int_s \delta_h \frac{\nabla\phi}{|\nabla\phi|}\eta\bar{n} \; dS - \epsilon \int_{u_o} \delta_h \left(\nabla \cdot \left(\frac{\nabla\phi}{|\nabla\phi|}\right)\right)\eta \; dxdy$$

Finally $I_\mu(\epsilon)$ can be differentiated with respect to ϵ

$$\frac{\partial I_\mu(\epsilon)}{\partial\epsilon}|_{\epsilon=0} = \int_s \delta_h \frac{\nabla\phi}{|\nabla\phi|}\eta\bar{n} \; dS - \int_{u_o} \delta_h \left(\nabla \cdot \left(\frac{\nabla\phi}{|\nabla\phi|}\right)\right)\eta \; dxdy = 0$$

Since the expression above is equal to zero for all functions, recall that η is an arbitrary function, so

$$\frac{\delta_h}{|\nabla\phi|}(\nabla\phi)\cdot\bar{n} = 0 \;\; and \;\; -\delta_h div\left(\frac{\nabla\phi}{|\nabla\phi|}\right) = 0. \tag{A.10}$$

Here $\bar{n}$ denotes the exterior normal to the boundary of u_0. The left expression in Equation A.10 states that ϕ is constant at the boundary of the image;

$$\frac{\delta_h}{|\nabla\phi|}\frac{\partial\phi}{\partial\bar{n}} = 0.$$

There are still two fitting terms to transform in Equation A.1 before we have the complete associated Euler-Lagrange equation. Again we replace ϕ with $\tilde{\phi}$ and Taylor expand

$$\begin{aligned} I_{\lambda_1}(\epsilon) &= \lambda_1 \int_{u_o} (u_0 - c_1)^2 (H_h(\tilde{\phi})) \; dxdy \\ &= \lambda_1 \int_{u_o} (u_0 - c_1)^2 (H_h(\phi + \epsilon\eta)) \; dxdy \\ &= \lambda_1 \int_{u_o} (u_0 - c_1)^2 H_h(\phi) \; dxdy + \lambda_1 \int_{u_o} (u_0 - c_1)^2 \frac{\partial H_h}{\partial\phi}\epsilon\eta)) \; dxdy \end{aligned}$$

Then we differentiate with respect to the parameter ϵ to find the extremal minimising the energy

$$\frac{\partial I_{\lambda_1}(\epsilon)}{\partial \epsilon}|_{\epsilon=0} = \lambda_1 \int_{u_o} (u_0 - c_1)^2 \frac{\partial H_h}{\partial \phi}\eta))\ dxdy = 0$$

This means that

$$\begin{aligned} \lambda_1(u_0 - c_1)^2 \frac{\partial H_h}{\partial \phi} &= 0 \\ \lambda_1(u_0 - c_1)^2 \delta_h(\phi) &= 0. \end{aligned} \tag{A.11}$$

The last fitting term in Equation A.1 can be treated the exact same way

$$\begin{aligned} I_{\lambda_2}(\epsilon) &= \lambda_2 \int_{u_o} (u_0 - c_2)^2 (1 - H_h(\tilde{\phi}))\ dxdy \\ &= \lambda_2 \int_{u_o} (u_0 - c_2)^2 (1 - H_h(\phi))\ dxdy - \lambda_2 \int_{u_o} (u_0 - c_2)^2 \frac{\partial H_h}{\partial \phi}\epsilon\eta))\ dxdy \end{aligned}$$

Determining the stationary expression

$$\frac{\partial I_{\lambda_2}(\epsilon)}{\partial \epsilon}|_{\epsilon=0} = -\lambda_2 \int_{u_o} (u_0 - c_2)^2 \frac{\partial H_h}{\partial \phi}\eta))\ dxdy = 0.$$

Finally we obtain the last term in the associated Euler-Lagrange equation minimising the energy F_h,

$$-\lambda_2(u_0 - c_2)^2 \delta_h(\phi) = 0. \tag{A.12}$$

We can now collect all four terms, Equation A.4, A.10, A.11, A.12, and write the equation minimising F_h

$$\begin{aligned} \frac{dF_h}{d\epsilon} = \quad & \delta_h(\phi) \Big(\nu - \mu\ div \frac{\nabla \phi}{|\nabla \phi|} \\ & + \lambda_1(u_0 - c_1)^2 - \lambda_2(u_0 - c_2)^2 \Big) = 0. \end{aligned} \tag{A.13}$$

A.2 Shape functions used to determine extrusion velocity

Each of the nine nodes in the correlation matrix (the maximum and its eight neighbours) have a corresponding shape function that is defined everywhere in the fitting region. We denote the nine values (or nodes) of the correlation

matrix $r_{\{1,2...9\}}$, and let $N_{\{1,2...9\}}$ be their corresponding shape functions. Figure A.1 ilulustrate were the shapefunctions behave and are defined on the correlation matrix R. The shape functions are required to be 1 in the node they belong to, and 0 at all other nodes,

$$N_1(r_1) = 1,\ N_1(r_{\neq 1}) = 0.$$

Further, the sum of all the shape-functions must always be 1 everywhere. The 2.-order shape-functions fulfilling these requirements are

$$\begin{aligned}
N_1(x,y) &= \frac{x(x-1)}{2}\frac{y(y-1)}{2}\ ,\ N_2(x,y) = \frac{x(x-1)}{2}(y-1)(y+1) \\
N_3(x,y) &= \frac{x(x-1)}{2}\frac{y(y+1)}{2}\ ,\ N_4(x,y) = (x-1)(x+1)\frac{y(y-1)}{2} \\
N_5(x,y) &= (x-1)(x+1)(y-1)(y+1)\ ,\ N_6(x,y) = (x-1)(x+1)\frac{y(y+1)}{2} \\
N_7(x,y) &= \frac{x(x+1)}{2}\frac{y(y-1)}{2}\ ,\ N_8(x,y) = \frac{x(x+1)}{2}(y-1)(y+1) \\
N_9(x,y) &= \frac{x(x+1)}{2}\frac{y(y+1)}{2}
\end{aligned} \tag{A.14}$$

The x and y values in the nodes are $x, y = [-111]$ (see Figure A.1), where $(1,1)$ is the maximum in R (r_5). The resolution of the shape-functions is $1/100$ of a pixel. The fitting function F is defined as

$$F(x,y) = \sum_{i=1}^{9} r_i N_i(x,y) \tag{A.15}$$

Another approach, is to solve the set of equations arising when requering that $\frac{\partial F}{\partial x} = 0$ and $\frac{\partial F}{\partial y} = 0$ in the maximum point of the fitting function.

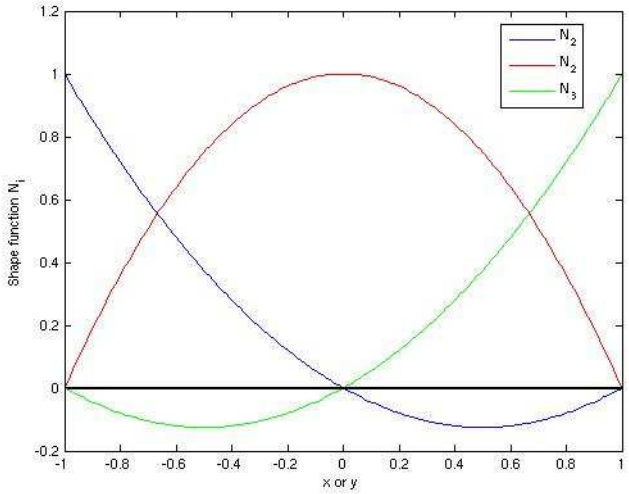

(a)

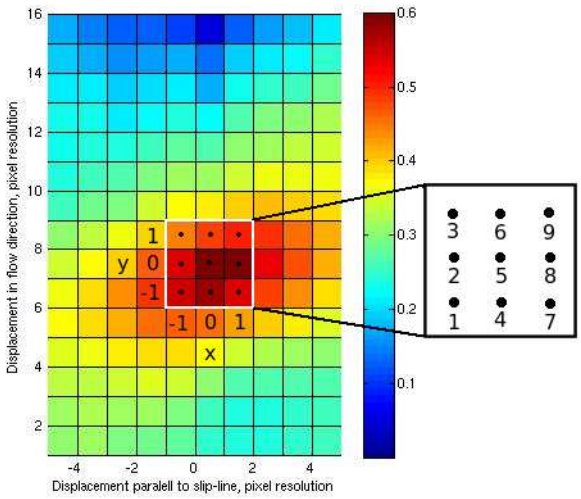

(b)

Figure A.1: (a) One-dimensional illustration of how the shape-functions behaves. The shape function N_i is 1 in r_i and 0 in all other nodes $r_{\neq i}$. The sum of all the nodes are always 1 ($\sum_{i=1}^{9} N_i = 1$). For the two-dimensional shape-functions used see Equation A.14. (b) The nodes are placed in the middle of each pixel in the correlation matrix. The maximum is defined as the centre, which here are $x = y = 0$. All nine shape functions are defined for x,y = (-1 0 1).

Appendix B

Instrumentation

B.1 Data aquisition - Labview code

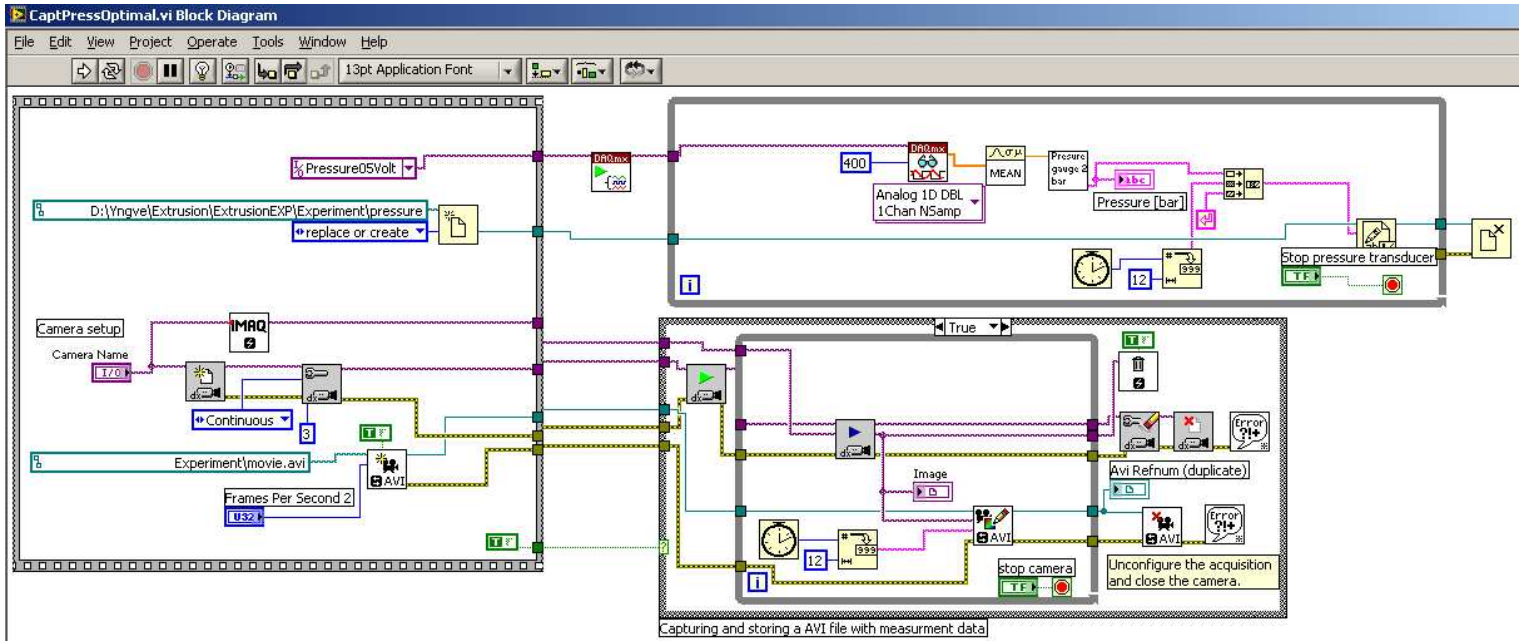

Figure B.1: Graphical Labview code for the image acquisition and pressure logging during the extrusion experiment.

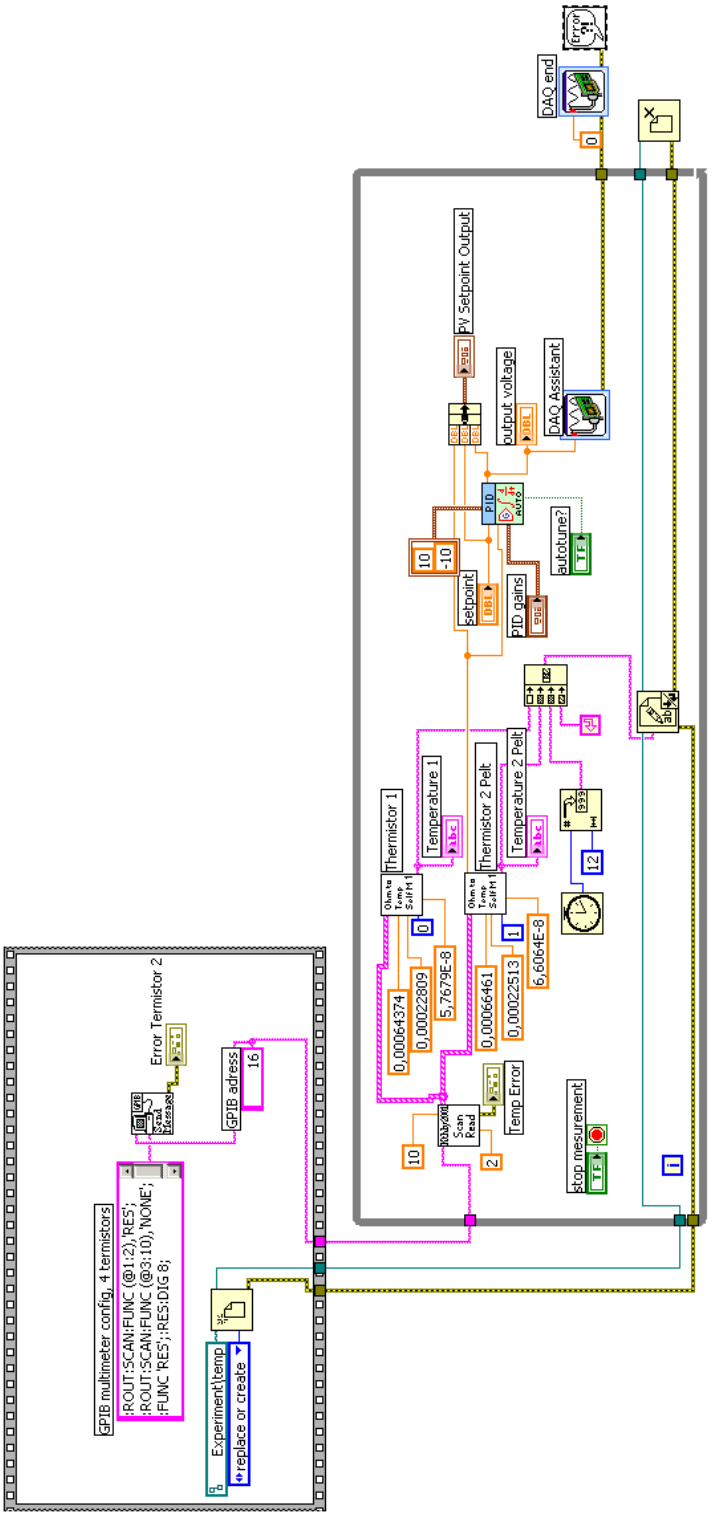

Figure B.2: Graphical Labview code for the PID temperature control loop.

B.2 Thermistor calibration (least square) - Matlab code

The Matlab code used to determine the Steinhart-Hart coefficients for the thermistors used for temperature control. The routine call on the function *paramfit* to performe a least square fit to determine the coefficients from the temperatur and resistance data. The latter menthod is written by Dag Dyste based on Numerical recipes by Press et. al.

```
%Reading thermistor(NTC) data(ohm) from file and using linear regression
%(the routine paramfit).
%Using T=1/(b1+b2 ln(R)+b3 ln(R)^3) => y = V * b + E

%Load data from file( Temp  therm1 therm2  therm3  therm4)
%data = load('calibdata.txt','\t');
data  = load('-ascii', 'calibdata.txt');
tnr = 4;                  %The coloum you read thermistor data from

% initialising
b      = [];                    % fitting coefficients
%V      = zeros(length(data),1); % the data ( 1 ln(R) ln(R)? )
E      = [];                    % Error
Stdb   = [];                    %std deviation in % of fitting coefficients
Stdfit = [];                    %std deviation in % of fit (total)

%Constructing CTdata (quartz thermometer) and THdata(Thermistor)
QTdata = data(7:end,1);
THdata = data(7:end, tnr);
QTdata = QTdata + 273.15;  %The formula used is for Kelvin
W      = ones(length(THdata),1);  % Weighting

V(:,1) = ones(length(THdata),1);
V(:,2) = log(THdata);
V(:,3) = log(THdata).^3;

figure(1),clf
plot(QTdata-273.5, THdata/1000,'.')
hold on

%Callin mlinreg for fitting
y=1./QTdata;
```

```
[b,E,Stdb,Stdfit] = paramFit(y,V,W);

T=1./(V*b);
%plotting the temperature calculated with the fitting coeff.
%T = 1/(b(1)+b(2)*log(THdata)+b(3)*log(THdata).^3);
plot(T-273.15,THdata/1000,'r.')
xlabel('Temperature [Celsius]')
ylabel(texlabel('Resistance [k Omega]'))

%standard deviation
QT = QTdata(61:1163);
T2  = T(61:1163);
s = sqrt((sum((QT-T2).^2))/length(QT));
sigma_mean = ((1/(length(QT)-1))^0.5)*s;
%%%%%%%%%%%%%%%%%%%%%%%%%%%%%%%%%%%%%%%%%%%%%%%%%%%%%%%%%%%%%%%%%%%%%%%%%%%%%%%
%%%%%%%%%%%%%%%%%%%%%%%%%%%%%%%%%%%%%%%%%%%%%%%%%%%%%%%%%%%%%%%%%%%%%%%%%%%%%%%
function [b,E,Stdb,Stdfit] = mlinregr(y,Vin,W)

% Weighted multilinear regression
% y    =  Vin  * b     + E
% (Jx1)  (JxP)   (Px1)   (Jx1)
%
% where W (Jx1) is the weight of each data point,
% W(i)=1/(standard deviation in i)
% i.e. to minimize the standard deviation of the whole fit one uses W=1./y,
% ordinary least squares: use W = ones(size(y));
% See Press et. al. pp 558 ->
%
% b      (Px1) = fitting coefficients
% E      (Jx1) = absolute error in each fitting point
% Stdb   (Px1) = standard deviation in percent of fitting coefficients
% Stdfit (1x1) = standard deviation in percent of fit
%                BEWARE that this uses the RELATIVE DEVIATION

  J = length(y);
  P = length(Vin(1,:));

  V = ( W*ones(1,P) ).*Vin;
  VTV = inv(V'*V);
  b = VTV*V'*( W .* y );
  E = y - Vin*b; %= y- (V./W)*VTV*V'*(W.*y);
```

```
  RelE = E./y;
  Var = (E'*E)/(J-P);
%  Stdb = 100.*sqrt(Var.*diag(VTV))./abs(b);
  Stdb = 100.*sqrt(Var.*diag(inv(Vin'*Vin)))./abs(b);
  Stdfit = 100.*sqrt((RelE'*RelE)./(J-P));
```

Appendix C

Image analysis - Matlab code

C.1 Snake

```
%%%%%%%%%%%%%%%%%%%%%%%%%%%%%%%%%%%%%%%%%%%%%%%%%%%%%%%%%%%%%%%%%%%%%%%%%%%%
%Generating a snake to indentify countours.
%Snake equation:
% -w1 (d?v/ds?)+ w2 (d4v/ds4) = -dP/dxy
%%%%%%%%%%%%%%%%%%%%%%%%%%%%%%%%%%%%%%%%%%%%%%%%%%%%%%%%%%%%%%%%%%%%%%%%%%%%
clear all
close all
%number of pics to analyse
n=1;
%name of avi move to analyse
movname = 'movie.avi';

%weights
%Tension, curve as short as possible
w1 = 1;
%Rigidity, changes in direction smooth
w2 = 1;
%Lambda,
la = 3;
%Number of nodes on snake
N=50;
%Number of iterations
iter = 50;

%Acuiring the smoothed potential from image
```

```
[dPdx,dPdy,ilx,ily,P,X,Y] = PicAqSmooth(n, movname);

%Init. snake
%x = 10*ones(size(ilx));
x = 100*linspace(2,max(X(:,1)),N)';
y =    linspace(2,max(Y(:,1)),N)';

%Init. matrix
[Ainvx,Ainvy] = InitMatrix(w1,w2,la,N);


%Finding the snakes x- & y-cordinates, iterations
[x,y] = SnakeSolv(dPdx,dPdy,iter,la,x,y,P,X,Y,ilx,ily,Ainvx,Ainvy);


%Plot of SL
%plot(x,y), xlabel({'x';'grr'}), ylabel('y')
%%%%%%%%%%%%%%%%%%%%%%%%%%%%%%%%%%%%%%%%%%%%%%%%%%%%%%%%%%%%%%%%%%%%%%%%%%%%%%%
%%%%%%%%%%%%%%%%%%%%%%%%%%%%%%%%%%%%%%%%%%%%%%%%%%%%%%%%%%%%%%%%%%%%%%%%%%%%%%%
function [dPdx,dPdy,ilx,ily,P,X,Y] = PicAqSmooth(n, movname)

framevec = n;
mov = aviread(movname,framevec);
X1 = flipud(double(frame2im(mov(1))));
P = X1;
[ni,nj] = size(P);
ilx = 2:(ni-1);
ily = 2:(nj-1);
%finding potential
dPdx = (P(ilx,ily+1)-P(ilx,ily-1))/2;
dPdy = (P(ilx+1,ily)-P(ilx-1,ily))/2;
%norm. the potential
wht  = (max(abs(dPdx(:))));
wht  = wht + (wht==0);
dPdx = dPdx/wht;
wht  = (max(abs(dPdy(:))));
wht  = wht + (wht==0);
dPdy = dPdy/wht;
[X,Y] = meshgrid(ily,ilx);
%%%%%%%%%%%%%%%%%%%%%%%%%%%%%%%%%%%%%%%%%%%%%%%%%%%%%%%%%%%%%%%%%%%%%%%%%%%%%%%
```

```
%%%%%%%%%%%%%%%%%%%%%%%%%%%%%%%%%%%%%%%%%%%%%%%%%%%%%%%%%%%%%%%%%%%%%%%%%%%%
function [Ainvx,Ainvy] = InitMatrix(w1,w2,la,N)
%The equations for the A matrix, drived parameters(Taylor)
a = w2;
b = -w1-4*w2;
c = 2*w1+ 6*w2+la;
% Make matrix
I = zeros(1,5*N);
J = zeros(1,5*N);
V = zeros(1,5*N);
tmp = 1:N;
elm = [a,b,c,b,a];
for n = 1:5
    ind = tmp+N*(n-1);
    I(ind) = tmp;
    J(ind) = mod(tmp-1-3+n,N)+1;
    V(ind) = elm(n)*ones(1,N);
end
A   = sparse(I,J,V,N,N);
Ax  = A;
Ay  = A;
%Modify exp. for boundary nodes in x direction
Ax(1:2,:)   = 0;
Ax(1,1:5) = [-w1+w2+la 2*w1-4*w2    -w1+w2*6 -4*w2 w2];
Ax(2,1:5) = [-w1+w2    2*w1-4*w2+la -w1+w2*6 -4*w2 w2];

Ax(end-1:end,:)         = 0;
Ax(end-1,end-4:end)     = [w2 -4*w2 -w1+w2*6 2*w1-4*w2+la -w1+w2];
Ax(end,end-4:end)       = [w2 -4*w2 -w1+w2*6 2*w1-4*w2    -w1+w2+la];
%Modify exp. for boundary nodes in y direction
Ay(1:2,:)               = 0;
Ay(1  ,1)               = 1;
Ay(2,1:5)               = [-w1+w2 2*w1-4*w2+la -w1+w2*6 -4*w2 w2];

Ay(end-1:end,:)         = 0;
Ay(end-1,end-4:end)     = [w2 -4*w2 -w1+w2*6 2*w1-4*w2+la -w1+w2];
Ay(end  , end     )     = 1;
%Find inverse matrices
Ainvx = inv(Ax);
Ainvy = inv(Ay);
%%%%%%%%%%%%%%%%%%%%%%%%%%%%%%%%%%%%%%%%%%%%%%%%%%%%%%%%%%%%%%%%%%%%%%%%%%%%
```

```
%%%%%%%%%%%%%%%%%%%%%%%%%%%%%%%%%%%%%%%%%%%%%%%%%%%%%%%%%%%%%%%%%%%%%%%%
%Finding the curve that locally balance the internal(snake) forces and
%external(picture) forces. Then solving it iterative to find the global
%best fit. x-y is the snakes cordinates.
% [A][x]=[-dp/dxy]
%%%%%%%%%%%%%%%%%%%%%%%%%%%%%%%%%%%%%%%%%%%%%%%%%%%%%%%%%%%%%%%%%%%%%%%%
function [x,y] = SnakeSolv(dPdx,dPdy,iter,la,x,y,P,X,Y,ilx,ily,Ainvx,Ainvy)

% "Time" iteration to find global minima.

for t=1:iter
     dPdx_interp = interp2(X,Y,dPdx,x,y);
     dPdy_interp = interp2(X,Y,dPdy,x,y);

     %boundary in y-direct.
     dPdy_interp(1  ) = la*y(1  ) - 2;
     dPdy_interp(end) = la*y(end) - max(Y(:,1)) + 1;

     x = Ainvx*(la*x - dPdx_interp);
     y = Ainvy*(la*y - dPdy_interp);

     figure(2), clf
     surf(X,Y,P(ilx,ily)), axis off,shading flat, view(0,90), hold on
     plot3(x,y,(max(P(:))-150)*ones(size(x)),'g.-');
     drawnow
end
%%%%%%%%%%%%%%%%%%%%%%%%%%%%%%%%%%%%%%%%%%%%%%%%%%%%%%%%%%%%%%%%%%%%%%%%
```

C.2 Image segmentation

```
%%%%%%%%%%%%%%%%%%%%%%%%%%%%%%%%%%%%%%%%%%%%%%%%%%%%%%%%%%%%%%%%%%%%%%%%
%algoritem for finding contours in pictures, based on levelset method.
%%%%%%%%%%%%%%%%%%%%%%%%%%%%%%%%%%%%%%%%%%%%%%%%%%%%%%%%%%%%%%%%%%%%%%%%
%parameters
h   = 0.5;
u   = 0.01*255^2;
v   = 0;
la1 = 1;
la2 = 1;
```

```
dt  = 0.4;
%aq. images and time data
fileinfo  = aviinfo('movie.avi');
frame_n   = 100;               % # frames to be read
be = 600; en = be+frame_n-1;   %First and last frame to read from the AVI.
mov       = aviread('movie.avi', be:en);
frame_t   = load('framedata'); %millisecond time data
frame_t   = frame_t-frame_t(be);
time      = frame_t(be:en);
xrange    = 295:350;        %pixel span,horisontal (flow) direction in image
yrange    = 140:360;        %pixel span,vertical direction in image
%movie(mov)

for npic=1:frame_n
    im_org  = double(frame2im(mov(npic)));
    im      = im_org(yrange,xrange);
    im      = 255*(im - min(im(:)))/(max(im(:))-min(im(:)));
    %numerics %%%%%%%%%%%%%%%%%%%%%%%%%%%%%%%%%%%%%%%%%%%%%%%%%%%%%%%%%%%%%%%%
    iter    = 30;
    [Nx Ny] = size(im);
    nx      = 1:Nx;
    ny      = 1:Ny;
    [X,Y]   = meshgrid(ny,nx);
    phi     = zeros(Nx,Ny);
    npix    = Nx*Ny;
    ie      = (Nx-2)*(Ny-2); %Number of points with no boundery, inside elm.
    phi(:,:)= X-10; %(i,j) Initial level-set function
    %phi(:,:)= 3.8*X-ceil(mean(ny))-(X).^(1.25);

    for nn=1:iter%solving phi(n+1)

        c1   = sum(sum(im.*(0.5*(1+2/pi*atan(phi/h))))) / ...
            sum(sum(0.5*(1+2/pi*atan(phi/h))));

        c2   = sum(sum(im.*(1-0.5*(1+2/pi*atan(phi/h))) )) / ...
            sum(sum(1-0.5*(1+2/pi*atan(phi/h))));

        d_h = 1./(pi*(1+(phi/h).^2 ));

        %A i= 1:end-1, j = 2:end-1
        A    = sqrt(((phi(2:end,2:end-1) - ....
```

```
            phi(1:end-1,2:end-1)).^2/h^2 + ...
            (phi(1:end-1,3:end) - ...
            phi(1:end-1,1:end-2)).^2/(2*h)^2));

Amax             = max(A(:));
A(A < 1e-8*Amax) =  1e-8*Amax;
A                = 1./A;

%B i= 2:end-1, j = 1:end-1
B    = sqrt(((phi(3:end,1:end-1) - phi(1:end-2,1:end-1)).^2/(2*h)^2 +
    (phi(2:end-1,2:end) - phi(2:end-1,1:end-1)).^2/h^2));

Bmax             = max(B(:));
B(B < 1e-8*Bmax) =  1e-8*Bmax;
B                = 1./B;

% Constants in eq.
ii  = repmat(2:Nx-1,1,Ny-2);                %Nx
jj  = reshape(repmat(2:Ny-1,Nx-2,1),1,ie); %Ny
cnt = sub2ind(size(phi),ii,jj);

U   = reshape((dt*d_h(cnt)*u)/h^2,Nx-2,Ny-2); %prefactor

C   = [-B(:,1:end-1) -A(1:end-1,:) (B(:,1:end-1) + B(:,2:end) + ...
    A(1:end-1,:) + A(2:end,:) + 1./U) -A(2:end,:) -B(:,2:end)];

I   = zeros(1,npix*5);
J   = zeros(1,npix*5);
K   = zeros(1,npix*5);
% Right hand side
RHS = zeros(npix,1);

tmp = 1:ie;
dbi = [0 -1 0 1 0]; %non-elegant cheating
dbj = [-1 0 0 0 1]; %non-elegant cheating

for n=1:5
    ind = tmp + ie*(n-1);
    K(ind) = U(:)'.*C(ie*(n-1)+1:ie*(n-1)+ie);
    I(ind) = sub2ind(size(phi),ii,jj);
    J(ind) = sub2ind(size(phi),ii+dbi(n),jj+dbj(n));
```

```
end

RHS(cnt) = phi(cnt) + dt*d_h(cnt).*(-v - la1*(im(cnt)-c1).^2 ...
    + la2*(im(cnt)-c2).^2);

%boundaries (where phi(1,1) is in bottom left corner)
% Left
ind = ind(end) + (1:Nx-2);
ii = 2:Nx-1;
jj = ones(size(ii));

K(ind) = 1;
I(ind) = sub2ind(size(phi),ii,jj);
J(ind) = sub2ind(size(phi),ii,jj);

ind = ind(end) + (1:Nx-2);
K(ind) = -1;
I(ind) = sub2ind(size(phi),ii,jj);
J(ind) = sub2ind(size(phi),ii,jj+1);

% right
ind = ind(end) + (1:Nx-2);
ii = 2:Nx-1;
jj = Ny*ones(size(ii));

K(ind) = 1;
I(ind) = sub2ind(size(phi),ii,jj);
J(ind) = sub2ind(size(phi),ii,jj);

ind = ind(end) + (1:Nx-2);
K(ind) = -1;
I(ind) = sub2ind(size(phi),ii,jj);
J(ind) = sub2ind(size(phi),ii,jj-1);

%bottom
ind = ind(end) + (1:Ny-2);
jj  = 2:Ny-1;
ii  = ones(size(jj));

K(ind) = 1;
I(ind) = sub2ind(size(phi),ii,jj);
```

```
J(ind) = sub2ind(size(phi),ii,jj);

ind = ind(end) + (1:Ny-2);
K(ind) = -1;
I(ind) = sub2ind(size(phi),ii,jj);
J(ind) = sub2ind(size(phi),ii+1,jj);

%top
ind = ind(end) + (1:Ny-2);
jj  = 2:Ny-1;
ii  = Nx*ones(size(jj));

K(ind) = 1;
I(ind) = sub2ind(size(phi),ii,jj);
J(ind) = sub2ind(size(phi),ii,jj);

ind = ind(end) + (1:Ny-2);
K(ind) = -1;
I(ind) = sub2ind(size(phi),ii,jj);
J(ind) = sub2ind(size(phi),ii-1,jj);

% Bounderies in the corners
ii = [1 Nx 1 Nx];
jj = [1 1 Ny Ny] ;
ind = ind(end) + (1:4);

K(ind) = 1;
I(ind) = sub2ind(size(phi),ii,jj);
J(ind) = sub2ind(size(phi),ii,jj);

ind = ind(end) + (1:4);
i   = [1 -1  1 -1];
j   = [1  1 -1 -1];
K(ind) = -1;
I(ind) = sub2ind(size(phi),ii,jj);
J(ind) = sub2ind(size(phi),ii+i,jj+j);

%solving for phi_n
indi      = find(I==0);
I(indi)   = [];
J(indi)   = [];
```

```
        K(indi)   = [];
        AA = sparse(I,J,K,npix,npix);

        phi = AA\RHS;

        phi = reshape(phi,Nx,Ny);
    end

    % Save slip line evolution
   [xyc] = contourc(phi, [0 0]);
   while ~isempty(xyc)
       num      = round(xyc(2,1));
       xyc(:,1) = [];
       %xc = xyc(1,1:num);
       %yc = xyc(2,1:num);
       if (xyc(2,num) < 10) && (xyc(2,1) > length(yrange)-9) || ...
                (xyc(2,1) < 10) && (xyc(2,num) > length(yrange)-9)
           xc{npic} = xyc(1,1:num);
           yc{npic} = xyc(2,1:num);
       end
       xyc(:,1:num) = [];
   end
end
save('SliplineCord&Time600-699', 'xc', 'yc','time')
```

C.3 Velocity measurement by correlating average intensities

```
clear all
close all
% Looking at two squares, sqA and sqB, seperated by dx
% Measuring velocity in die by convolution of the intensities
% iA and iB in x direction.
%%%%%%%%%%%%%%%%%%%%%%%%%%%%%%%%%%%%%%%%%%%%%%%%%%%%%%%%%%%%%%%%%%%%%%%%%%%%
% Loading movie and time data
fileinfo  = aviinfo('movie.avi');
frame_n   = 900;
be = 699; en = be+frame_n-1; %First and last frame to read from the AVI.
mov       = aviread('movie.avi', be:en);
```

```
frame_t   = load('framedata');
frame_t   = frame_t-frame_t(be);
time      = frame_t(be:en);
%%%%%%%%%%%%%%%%%%%%%%%%%%%%%%%%%%%%%%%%%%%%%%%%%%%%%%%%%%%%%%%%%%%%%%%%%%%%
% physics
dx = 0.0769;  % the length of 100 pixels [mm].
avrg_t = ((frame_t(end)-frame_t(1))/ ... %time betw.two im.frames [s]
         (length(frame_t)))/1000;
ds = 20; % distance between the two sq. in pixels

%numreics
tau = 40;                   %number of frames to average intensities over.
f1   = zeros(1,tau);
g1   = zeros(1,tau);
f2   = zeros(1,tau);
g2   = zeros(1,tau);
f3   = zeros(1,tau);
g3   = zeros(1,tau);
%%%%%%%%%%%%%%%%%%%%%%%%%%%%%%%%%%%%%%%%%%%%%%%%%%%%%%%%%%%%%%%%%%%%%%%%%%%%
frame_n = 900;
for ii=1:frame_n-tau

    disp(num2str(ii));

for j=1:tau    % recording intensity for the two squares sqA and sqB
    im = double(frame2im(mov(ii+j-1)));
    f1(j) = mean(mean(im((170:180)+110,360:370)));
    g1(j) = mean(mean(im((170:180)+110,(360:370)+ds)));

    f2(j) = mean(mean(im((170:180),360:370)));
    g2(j) = mean(mean(im((170:180),(360:370)+ds)));


    f3(j) = mean(mean(im((170:180)-80,360:370)));
    g3(j) = mean(mean(im((170:180)-80,(360:370)+ds)));
end

[v1,x_sp1,offset1] = my_corr_im(f1,g1,tau,ds,dx,avrg_t);
[v2,x_sp2,offset2] = my_corr_im(f2,g2,tau,ds,dx,avrg_t);
[v3,x_sp3,offset3] = my_corr_im(f3,g3,tau,ds,dx,avrg_t);
```

```
v1_list(ii) = v1;
xsp1_list(ii) = x_sp1;
offset1_list(ii) = offset1;

v2_list(ii) = v2;
xsp2_list(ii) = x_sp2;
offset2_list(ii) = offset2;


v3_list(ii) = v3;
xsp3_list(ii) = x_sp3;
offset3_list(ii) = offset3;

% %plots
% figure(1), clf
% dt = x_sp3+1;
% t = 1:tau;
% plot(t+dt,f3-mean(f3),'b'), hold on
% plot(t,g3-mean(g3),'r')
end

figure(3), clf
tm = time(1:length(v1_list))/1000;
plot(tm,v1_list,'g'), hold on
plot(tm,v2_list,'r'), hold on
plot(tm,v3_list,'b'), axis tight

d12 = abs(v1_list - v2_list);
d13 = abs(v1_list - v3_list);
d23 = abs(v2_list - v3_list);

[val,ind] = min([d12;d13;d23],[],1);

v_mean = zeros(size(v1_list));

v_mean(ind==1) = 0.5*( v1_list(ind==1) + v2_list(ind==1) );
v_mean(ind==2) = 0.5*( v1_list(ind==2) + v3_list(ind==2) );
v_mean(ind==3) = 0.5*( v2_list(ind==3) + v3_list(ind==3) );

std_v = zeros(size(v1_list));
std_v(ind==1) = d12(ind==1);
```

```
std_v(ind==2) = d13(ind==2);
std_v(ind==3) = d23(ind==3);

figure(4), clf
plot(tm, v_mean,'k-','linewidth',2), hold on
plot(tm, v_mean+std_v,'r-','linewidth',1), hold on
plot(tm, v_mean-std_v,'r-','linewidth',1), hold on
axis tight, xlabel('time [s]'), ylabel('velocity [m/s]')
%%%%%%%%%%%%%%%%%%%%%%%%%%%%%%%%%%%%%%%%%%%%%%%%%%%%%%%%%%%%%%%%%%%%%%%%%%%%
%%%%%%%%%%%%%%%%%%%%%%%%%%%%%%%%%%%%%%%%%%%%%%%%%%%%%%%%%%%%%%%%%%%%%%%%%%%%
function [v,x_sp,offset] = my_corr_im(f,g,tau,ds,dx,avrg_t)

fg_cor = zeros(1,tau/2);

for i=1:tau/2
    fg_cor(i) = mean((f(1:end-i)-mean(f(1:end-i))) ...
        .*(g(1+i:end)-mean(g(1+i:end))));
%   fg_cor(i) = mean(f(1:end-i).*g(1+i:end));
end

[C,offset] = max(fg_cor);

% Subpixel resolution
x = offset + (-2:2);

if (x(1) > 0) && (x(end)<(tau/2))
    [a,Std] = paramFit(x-1,fg_cor(x));

    x_sp = -a(2)/2/a(3);

    dx_sp = x_sp*sqrt( (Std(2)/a(2))^2 + (Std(3)/a(3))^2 );

    % velocity
    v =(ds*dx/100) / (x_sp*avrg_t); % velocity [mm/s]
else
    offset = -1;
    x_sp = -1;
    v     = -1;
end
%%%%%%%%%%%%%%%%%%%%%%%%%%%%%%%%%%%%%%%%%%%%%%%%%%%%%%%%%%%%%%%%%%%%%%%%%%%%
%%%%%%%%%%%%%%%%%%%%%%%%%%%%%%%%%%%%%%%%%%%%%%%%%%%%%%%%%%%%%%%%%%%%%%%%%%%%
```

```
function [a,Std] = paramFit(x,y)

y = y';

%General Linear Least Squares method. Find parameters a that best fit
%the datapoints (x,y) with the given basis function X.
%   y   =   a   *  X(x)
% [Nx1]   [1xM]   [NxM]
% Press et al page 665.

%Weighting of each data-point, w is the measurement error.
w = ones(length(x),1);

N = length(x);
M = 3; %number of fitting parameters,# of basis functions
% Define basis function X
X(:,1) = ones(N,1);
X(:,2) = x;
X(:,3) = x.^2;

%Linear regression
A     = ((1./w)*ones(1,M)).*X;
beta  = A'*(y./w);
alpha = A'*A;
a     = inv(alpha)*beta;

%Determining the uncertanty in the parameters
Std   = diag(inv(alpha));
```

C.4 Velocity measurement by correlating pixels

```
% PAREMETERS
xbox = [-40,40];
ybox = [-80,0];
dxr  = [-5, 5];
dyr  = [-15,0];
dt   = 1;  % n corr. with n+dt
NF   = 2; % # frames

frame_n   = NF+dt;
```

```
be = 1; en = be+frame_n-1;  %First and last frame to read from the AVI.

mov       = aviread('movie.avi', be:en);

load('SliplineCord&Time-1-3201.mat') %SL cord. and im. frame


frame_t   = load('framedata');
frame_t   = frame_t-frame_t(be);
timeVel   = frame_t(be:en);

vxlist = zeros(frame_n-dt,length(xrange_org));
vylist = zeros(frame_n-dt,length(xrange_org));

for n = 1:NF
    %display(['iteration: ',num2str(n,'%5d')])

    % Take out slipline region
    IM1  = double(frame2im(mov(n)));
    IM2  = double(frame2im(mov(n+dt)));
    %
    yb   = yrange_org(1);
    ye = yrange_org(end);
    xb   = xrange_org(1);
    xe = xrange_org(end);

    IM1    = IM1(:,xb:xe);
    IM2    = IM2(:,xb:xe);

    ysl1    = yc{n} + yb-1;
    xsl1    = xc{n};

    ysl2    = yc{n+dt} + yb-1;
    xsl2    = xc{n+dt};

    [vx,vy,xwidth] = CorrelationVel(IM1,IM2,xsl1,ysl1,xsl2,ysl2,...
                                    xbox,ybox,dxr,dyr,n);
    vxlist(n,1:xwidth) = vx(2,:);
    vylist(n,1:xwidth) = vy(2,:);
end
```

```
vxlist(:,xwidth+1:end) = [];
vylist(:,xwidth+1:end) = [];
%%%%%%%%%%%%%%%%%%%%%%%%%%%%%%%%%%%%%%%%%%%%%%%%%%%%%%%%%%%%%%%%%%%%%%%%%%%%
%%%%%%%%%%%%%%%%%%%%%%%%%%%%%%%%%%%%%%%%%%%%%%%%%%%%%%%%%%%%%%%%%%%%%%%%%%%%
function [vx,vy,xwidth] = CorrelationVel(IM1,IM2,xsl1,ysl1,xsl2,ysl2,...
                                         xbox,ybox,dxr,dyr,imnr)

% IM1/2          : image 1/2
% xsl1/2, ysl1/2 : slipline coordinates
% xbox, ybox     : size of the comparison region ([begin, end])
% dxr, dyr       : Size of the correlation region ([begin, end])
%                  of r
%
% r              : correlation matrix
%

% Numer of pixels in the x directions
Nx   = size(IM1,2);

% SORT xbox ybox dxr dyr
xbox = sort(xbox);
ybox = sort(ybox);

dxr  = sort(dxr);
dyr  = sort(dyr);

% REMOVE THE STATIC BACKGROUND
imbgr = max(IM1,IM2);

IM1 = imbgr-IM1;
IM2 = imbgr-IM2;

% DEFINE CORRELATION REGION

indbx = xbox(1):xbox(2);
indby = ybox(1):ybox(2);

% LIST OF PROBLEMATIC PIXEL
err_pix_x = [];

%%%%%%%%%%%%%%%%%%%%%%%%%%%%%%%%%%%%%%%%%%%%%%%%%%%%%%%%%%%%%%%%%%%%%%%%%%%%
```

```
xnbegin = 1 - min(xbox(1),0) - min(dxr(1),0);
xnend   = Nx - max(xbox(2),0) - max(dxr(2),0);

xwidth  = xnend-xnbegin+1;
vx      = zeros(2, xwidth);
vy      = zeros(2, xwidth);


count = 0;

for xn = xnbegin:xnend
    count = count + 1;
    % find x index
    indx1 = xn + indbx;

    % find y index
    % --- find y min
    ymin1 = round( min(ysl1( (xsl1>=indx1(1)) & (xsl1 <= indx1(end)))) );

    ymin2 = round( min(ysl2( (xsl2>=(indx1(1)+dxr(1)))...
                  & (xsl2 <= (indx1(end)+dxr(2)))) ) );

    ymin = min(ymin1,ymin2)-ybox(2)-dyr(2) - 5;

    indy1 = ymin + indby;

    lbox1 = IM1(indy1,indx1);


    r = zeros(dyr(2)-dyr(1)+1,dxr(2)-dxr(1)+1);

    for dx = dxr(1):dxr(2)
        indx2 = indx1 + dx;
        for dy = dyr(1):dyr(2)
            indy2 = indy1 + dy;

            lbox2 = IM2(indy2,indx2);

            if sqrt(sum(lbox2(:).^2)) == 0
                r(dy-dyr(1)+1,dx-dxr(1)+1) = 0;
            else
```

```
                r(dy-dyr(1)+1,dx-dxr(1)+1) = sum(lbox1(:).*lbox2(:))/ ...
                          sqrt(sum(lbox1(:).^2))/sqrt(sum(lbox2(:).^2));
            end
        end
    end

    [ry,rx] = find( r == max(r(:)));
    [my,mx] = size(r);

    BOL = false;

    while (ry < 2) || (ry >= my) || (rx<2) || (rx >= mx)
        r(ry,rx) = 0;
        [ry,rx] = find( r == max(r(:)));
        BOL = true;
    end

    if BOL
        err_pix_x = [err_pix_x, xn];
    end

    [rx,ry] = SubPixelRes_shapefunc(rx,ry,r);

    vy(:,count) = [xn; ry+dyr(1)-1];
    vx(:,count) = [xn; rx+dxr(1)-1];
end

if ~isempty(err_pix_x)
    save(['./dodgy_correlations_',num2str(imnr,'%d')],'err_pix_x')
end
%%%%%%%%%%%%%%%%%%%%%%%%%%%%%%%%%%%%%%%%%%%%%%%%%%%%%%%%%%%%%%%%%%%%%%%%%%%%
%%%%%%%%%%%%%%%%%%%%%%%%%%%%%%%%%%%%%%%%%%%%%%%%%%%%%%%%%%%%%%%%%%%%%%%%%%%%
function  [rx,ry] = SubPixelRes_shapefunc(rx_org,ry_org,r)

indx = rx_org + (-1:1);
indy = ry_org + (-1:1);

z    = reshape(r(indy,indx),numel(indx)^2,1);

[X,Y] = meshgrid(linspace(-1,1,201));
```

```
N     = zeros(201,201,9);

N(:,:,1) = X.*(X-1).*Y.*(Y-1)/4;
N(:,:,2) = X.*(X-1).*(1+Y).*(1-Y)/2;
N(:,:,3) = X.*(X-1).*Y.*(Y+1)/4;

N(:,:,4) = (1-X).*(1+X).*Y.*(Y-1)/2;
N(:,:,5) = (1-X).*(1+X).*(1+Y).*(1-Y);
N(:,:,6) = (1-X).*(1+X).*Y.*(Y+1)/2;

N(:,:,7) = X.*(X+1).*Y.*(Y-1)/4;
N(:,:,8) = X.*(X+1).*(1+Y).*(1-Y)/2;
N(:,:,9) = X.*(X+1).*Y.*(Y+1)/4;

Z = zeros(201);

for n = 1:9
    Z = Z + z(n)*N(:,:,n);
end

ind = find(Z == max(Z(:)));

rx  = X(ind(1)) + rx_org;
ry  = Y(ind(1)) + ry_org;
```

Bibliography

[1] R.M Iverson et al. Dynamics of seismogenic volcanic extrusion at mount st helens in 2004-05. NATURE, 444(7118):439–443, 2006.

[2] S. Planke, H. Svensen, M. Hovland, D. A. Banks, and B. Jamtveit. Mud and fluid migration in active mud volcanoes in azerbaijan. Geo-Marine Letters, 23(1):258–268, 2003.

[3] Roland Bürgmann Frédérique Rolandone and Robert Nadeau. The evolution of the seismic-aseismic transition during the earthquake cycle: Constraints from the time-dependent depth distribution of aftershocks. GEOPHYSICAL RESEARCH LETTERS, 31:L23610, 2004.

[4] European Aluminium Assosiation; Sustainability Report 2006. http://www.eaa.net.

[5] Website by Roy Beardmore. Roy@roymech.co.uk, http://www.cmse.ed.ac.uk/AdvMat45/CrystalBasics.pdf.

[6] S. Støren and P.T Moe. Handbook of Aluminium, Chapter 8; Extrusion. Marcal Dekker, 1 edition, 2003.

[7] Frode Halvorsen. Mathematical Modeling of Shape Variations on Extruded Aluminium Sections. PhD thesis, University of Oslo, Norway, 2005.

[8] Shahriar Abtahi. Friction and interface reactions on the die land in thin-walled extrusion. PhD thesis, NTNU, Norway, 1995.

[9] S. Abtahi. A numerical study of the material flow in the bearing channel of extrusion: Effect of boundary conditions. Technical Report STF 20F 93160, SINTEF Materials Technology, 1993.

[10] T. Welo. Thermo-mechanical conditions in the bearing channel of aluminium extrusion dies. Technical report, SINTEF Materials Technology, 1993.

[11] T. Welo, S. Abtahi, I. Skauvik, S. Støren, M. Melander, and S. Tjøtta. Friction in the bearing channel of aluminium extrusion dies. Technical report, 15th Risø International Symposium on Material Science, 1994.

[12] K. Holthe. Modelling of coulomb friction in alma. Technical Report STF22-A98691, SINTEF Structural Engineering, 1998.

[13] T. Aukrust and S. LaZghab. Thin shear boundary layers in flow of hot aluminium. International Journal of Plasticity, 16:59–71, 2000.

[14] T. Aukrust et. al. Texture and surface grain structure in aluminium sections. In number I, volume 1, pages 171–177, 1996.

[15] Sami LaZghab. New modelling techniques for the shear boundary layer in the bearing channel during aluminium extrusion. PhD thesis, The Univerity of Oslo, Oslo, Norway, 2000.

[16] M. Lefstad. Metallurgical Speed Limitations in Extrusion of AlMgSi-alloys. PhD thesis, NTNU, Trondheim, Norway, 1993.

[17] P. T. Moe. Pressure and strain measurement during hot extrusion of aluminium. PhD thesis, Norwegian University of Science and Technology, Trondheim, Norway, 2005.

[18] H. Valberg. Metal flow in direct axisymetric extrusion of aluminium. Journal of Materials Processing Technology, 31:39–55, 1992.

[19] H. Valberg and T. Malvik. An experimental investigation of the material flow inside the bearing channel in aluminium extrusion. International Journal of Materials and Production technique, 29(1):69–79, 1994.

[20] Interactions Jean Schmittbuhl, Stéphane Roux, Jean-Pierre Vilotte, and Knut Jorgen Måløy. Interfacial crack pinning: Effect of nonlocal. Physical Review E, 75, 1995.

[21] Jean Schmittbuhl and Knut Jørgen Måløy. Direct observation of a self-affine crack propagation. 78(3888), 1997.

[22] Knut Jørgen Måløy and Jean Schmittbuhl. Dynamical event during slow crack propagation. Phys. Rev. Lett., 87(105502), 2001.

[23] Knut Jørgen Måløy, Stéphane Santucci, Jean Schmittbuhl, and Renaud Toussaint. Local waiting time fluctuations along a randomly pinned crack front. Phys. Rev. Lett., 96(045501), 2006.

[24] J. N. Sherwood (Editor). The Plastically Crystalline State. WILEY, 1979.

[25] Harold J Frost and Michael F Ashby. Deformation-Mechanism Maps, The Plasticity and Creep of Metals and Ceramics. Pergamon Pr, 1982.

[26] Centre for Materials Science and The University of Edinburgh Engineering. http://www.cmse.ed.ac.uk/AdvMat45/CrystalBasics.pdf.

[27] Jason L. Rhoads Department of Nuclear Engineering University of California Basic Explanation of Creep Processes. http://www.nuc.berkeley.edu/thyd/ne161/jlrhoads/creep.html.

[28] Don Turcotte and Jerry Schubert. Geodynamics. Cambridge, 2. chapter 7 edition, 2002.

[29] O. Prakash and D. R. H. Jones. Creep of metal-type organic compounds - i. pure polycrystals and particle-hardened systems. Acta metall. mater, 40:3443–3449, 1992.

[30] S Abtahi and S. Støren. An investigation of surface defects mechanisms in hot extrusion of aluminium. Technical report, Dep. of Machine Design and Materials Technology at the Norwegian Institute of Technology, Trondheim, Norway, 1997.

[31] S. Tverlid. Modelling of Friction in the Bearing Channel of Dies for Extrusion of Aluminium Sections. PhD thesis, The Norwegian Institute of Technology, Trondheim, Norway, 1997.

[32] Mary L. Boas. Mathematical Methods in the Physical Science. John Wiley and Sons, 2. edition, 1966.

[33] G. L. Squires. Practical Physics. Cambridge, fourth edition edition, 2001.

[34] A. Michils. Bull. Soc. Chim. Belg., 57:575, 1948.

[35] P. D. Bons and J. L. Urai. Syndeformational grain growth: microstructures and kinetics. Journal of Structural Geology, 14:1101, 1992.

[36] M. Herwegh and M. Handy. The evolution of high-temperature mylonitic microfabrics: Evidence from simple shearing of a quartz analogue (norcamphor). Journal of Structural Geology, 18:689, 1996.

[37] Micro shear zones in experimetally deformed octachloropropane. Paul d bons and mark w. jessel. Journal of Structural Geology, 21:323, 1999.

[38] O. Prakash and D. R. H. Jones. Creep of metal-type organic compounds - ii. indentation creep. Acta mater., 44:891–897, 1996.

[39] G.C.Davies and D.R.H. Jones. Creep of metal-type organic compounds - iii. friction stress models for creep in particle-hardened systems. Scripta Materialia, 35:523–528, 1996.

[40] G.C.Davies and D.R.H. Jones. Creep of metal-type organic compounds - iv. application to hot isostatic pressing. Acta mater., 45:775–789, 1997.

[41] G.C.Davies and D.R.H. Jones. Creep of metal-type organic compounds - v. Scripta Materialia, 37:1745, 1997.

[42] the free encyclopedia; Aluminium Wikipedia. http://en.wikipedia.org/wiki/Aluminium.

[43] S. L. Robinson and O. D. Sherby. Activation energy for lattice self-diffusion in aluminium. Physica Status Solidi, 1(1):K119–K122, 1970.

[44] L. L. Levenson. Grain boundary diffusion activation energy derived from surface roughness measurements of aluminum thin films. Applied Physics Letters, 55:2617–2619, December 1989.

[45] National Instruments LabVIEW graphical programming. http://www.ni.com/labview/.

[46] User manual for Prosilica GC650 series camera. http://www.prosilica.com/products/gc650.html.

[47] Tony F. Chan and Luminita A. Vese. Active contours without edges. IEEE, 10, 2001.

[48] G. Aubert and Luminita A. Vese. A variational method in image recovery. SIAM J. Numer. Anal., 34:1948–1979, 1997.

[49] W T. Vetterling W. H. Press, S. A. Teukolsky and B. P. Flannery. Numerical recipes in Fortran. Pergamon Pr, second edition edition, 1992.

[50] Po-Chih Hung and A. S. Voloshin. In-plane strain measurement by digital image correlation. J. of the Braz. Soc. of Mech. Sci. and Eng., Vol. XXV, No. 3:215, 2003.

[51] high-level programming language Matlab. http://www.mathworks.com/.

[52] Jens Feder. Fractals. Plenum, 1 edition, 1988.

[53] M. P. Clode and T. Sheppard. Formation of die lines during extrusion of aa 6063. MATERIALS SCIENCE and TECHNOLOGY, 6:755, 1990.

[54] M. Tokizawa and K. Murotani K. Dohda. Mechanism of friction at the interface between tool surface and metals in hot extrusion of aluminium alloys (1st report) - effects of dies and extrusion temperature. Bull. Japan Soc. of Prec. Engg, 10(4), 1976.

[55] M. Tokizawa and N. Takatsuij. Effects of the die condition and billet composition on the surface characteristics of the extruded 6063 aluminium alloy. Transactions of the Japan Institute of Metals, 29(1):69–79, 1988.

[56] H. D. Young and R. A. Freedman. University Physics. Pearson, 11 edition, 2004.